Higgs boson searches in cascade decays of supersymmetric particles with the ATLAS detector at the LHC

Michele Consonni

Laboratoire d'Annecy-le-Vieux de Physique de Particules

Thèse présentée par

Michele Consonni

pour obtenir le titre de
Docteur de l'Université de Savoie
Specialité: Physique des particules

Recherche du boson de Higgs dans les cascades de désintégration de particules supersymétriques avec le détecteur ATLAS au LHC

Soutenue le 15 juillet 2008 devant la commission d'examen :

Lucia Di Ciaccio	Co-directrice de thèse
Rémi Lafaye	Directeur de thèse
Michel Lefebvre	Rapporteur
Margarete Muehlleitner	
Giacomo Polesello	
Mossadek Talby	Président

CONTENTS

ABSTRACT

The LHC is expected to deliver the first proton-proton collisions in September 2008 and the ATLAS experiment is designed to explore a large spectrum of phenomena that could arise from these interactions. In the context of supersymmetric extensions of the Standard Model, the lightest Higgs boson can be produced via cascade decays of supersymmetric particles. We investigate the possibility of observing such events with the ATLAS detector at the LHC. Firstly, we focus on the ATLAS capability in measuring the missing energy due to the passage of supersymmetric particles escaping the detection. Then, we show that, for some regions of the Minimal Supergravity parameter space compatible with the last LEP searches, the lightest Higgs boson can be discovered with less than 10 fb^{-1}, giving results competitive with standard Higgs production channels. We also study the possibility of measuring quantities related to the masses and couplings of the supersymmetric particles involved in the process. Finally, starting from these measurements, we use the `SFitter` tool to set up a global fit to the parameters of the underlying supersymmetric model, showing the validity of such procedure for constraining the theoretical interpretations of future LHC data.

1

THE STANDARD MODEL OF PARTICLE PHYSICS

1.1 The minimal gauge Lagrangian

The Standard Model (SM) is at present our best description of particle interactions; its validity has been tested and confirmed to a surprisingly high level of accuracy.

The Standard Model includes all the known fundamental spin-1/2 constituents of matter: three charged (e, μ, τ) and three neutral leptons $(\nu_e, \nu_\mu, \nu_\tau)$ and three family of quarks (u, d), (c, s) and (t, b). The interactions between them are provided by the exchange of vector boson mediators. The photon is responsible for the electromagnetic interactions between charged particles. The $W^\pm$ and Z^0 bosons are associated to the weak interactions, the most known manifestation of which is the neutron β decay. And finally eight gluons are responsible for the strong interactions, binding together quarks to form protons and neutrons.

These completely describe all the know fundamental forces in nature, with exception of gravity. In fact, in the context of particle physics, gravitation is extremely weak and thus negligible, at least at all energies in which we shall be interested. To give an idea of its magnitude, the gravitational attraction between two protons inside a nucleus is $\sim 10^{-36}$ times weaker than their electromagnetic repulsion. The gravitational strength becomes comparable to the other fundamental forces for energies at the Planck scale, $\Lambda_{\text{Planck}} \sim 10^{19}$ GeV, i.e. more than ten order of magnitude greater than the current experimental reach.

The Standard Model is formulated in the framework of relativistic quantum field theory. Such kind of theories grew up during the 1920s when the needs of a proper quantum treatment of the electromagnetic field pushed physicists to combine quantum mechanics of Heisenberg and Schrödinger with the theory of special relativity of Einstein. Their development culminated in late 1940s when Dyson, Feynman, Schwinger and Tomonaga introduced the renormalization procedure [1, 2, 3, 4, 5, 6, 7], solving the problem of the unphysical infinities that arise for example when calculating the electron energy shift due to the presence of the electromagnetic field. This led to the formulation of quantum electrodynamics (QED). In modern physics it is classified as a gauge theory[1].

In classical electromagnetism, the gauge symmetry is the local invariance that the Maxwell equations have under the transformation of the four-vector potential

$$A_\mu(x) \to A_\mu(x) - \partial_\mu \alpha(x), \tag{1.1}$$

where $\alpha(x)$ is an arbitrary function of space-time. This transformation, leaves the physical observables, the electric and magnetic fields, unchanged. In a modern point of view, the gauge symmetry becomes a fundamental principle of the theory.

Indeed, starting from the Lagrangian of a Lorentz invariant spin-1/2 free-field theory, i.e.

$$\mathcal{L}_0 = \bar{\psi}(x)(i\gamma^\mu \partial_\mu - m)\psi(x), \tag{1.2}$$

we can generalize the global phase invariance

$$\begin{cases} \psi(x) \to e^{+i\alpha}\psi(x) \\ \bar{\psi}(x) \to e^{-i\alpha}\bar{\psi}(x) \end{cases} \quad \alpha \in \mathbb{R} \tag{1.3}$$

to a local symmetry, allowing an independent symmetry transformation at every point of space-time:

$$\begin{cases} \psi(x) \to e^{+iq\alpha(x)}\psi(x) \\ \bar{\psi}(x) \to e^{-iq\alpha(x)}\bar{\psi}(x). \end{cases} \tag{1.4}$$

The arbitrarily extracted constant q is the coupling strength associated to the gauge symmetry, in the QED case it is the electron charge e. Under these transformations the derivative $\partial_\mu \psi(x)$ is not invariant and introduces in the Lagrangian a new term of the

[1]For a complete treatment see for example [8, 9].

form $q\bar{\psi}(x)\gamma^\mu\psi(x)\partial_\mu\alpha(x)$. The gauge symmetry is restored by replacing the ordinary derivative by the covariant derivative

$$D_\mu = \partial_\mu + iqA_\mu(x), \tag{1.5}$$

with a new vector field $A_\mu(x)$ that transforms according to Equation 1.1. Then, an interaction term between the fermionic and electromagnetic fields naturally arises:

$$\mathcal{L} = \bar{\psi}(x)(i\gamma^\mu D_\mu - m)\psi(x) = \mathcal{L}_0 - q\bar{\psi}(x)\gamma^\mu A_\mu\psi(x). \tag{1.6}$$

To complete the construction of the Lagrangian, we must add a kinetic term for the field $A_\mu(x)$. Again the request of local invariance constrains the possibilities to $F_{\mu\nu}F^{\mu\nu} = (\partial_\mu A_\nu - \partial_\nu A_\mu)(\partial^\mu A^\nu - \partial^\nu A^\mu)$. This is the Lagrangian of QED and its form has been worked out only on the basis of Lorentz and gauge symmetries. The corresponding quantum field theory is constructed by imposing the rules of quantization to the classical fields.

The transformation in Equation 1.4 corresponds to the invariance under the symmetry group $U(1)$. Other interesting Lagrangian may be built generalizing it to a symmetry group $\mathcal{G}$, as first stated by Mills and Yang [10]. In this case, new vector particles originate in the same way as the A_μ in QED and their interaction are restricted by the symmetry principle. In particular, interactions with fermions are given by the covariant derivative that generalizes 1.5

$$D_\mu = \partial_\mu - igA^i_\mu(x)\tau^i, \tag{1.7}$$

where g is the coupling constant, A^i_μ are the required new boson fields and τ^i the generators of $\mathcal{G}$. It is worth noticing that if $\mathcal{G}$ is a non-abelian group, such as $SU(N)$ with $N \geq 2$, since gauge bosons transform non-trivially under the gauge group itself, cubic and quartic self-interactions between gauge bosons appear. This is not the case of $U(1)$.

The Standard Model is based on the symmetry group $SU(3)_C \times SU(2)_L \times U(1)_Y$. The group $SU(3)_C$ is the gauge group of the strong interaction and is associated to its eight massless gluons. The related gauge charge is called colour (C) and quarks are the only coloured fermions. The $SU(2)_L$ symmetry involves the left-handed (L) part of all fermions, while the Y of the $U(1)_Y$ group stands for hypercharge and should not

be confused with the though related electric charge. In total, the remaining $SU(2)_L \times U(1)_Y$ part has four massless gauge bosons. However, measurements of the weak decay of neutron rather indicate a short range interaction and thus must be intermediated by massive bosons. But, explicit boson mass terms like $m^2 A_\mu(x) A^\mu(x)$ make the theory no longer gauge-invariant and also introduce renormalization problems. Moreover, the $SU(2)_L$ symmetry, under which left and right fermions transform differently, forbids all fermion mass terms. Thus, the obtained theory is completely massless.

The spontaneous symmetry breaking mechanism (Brout, Engler, Higgs [11, 12, 13, 14]) offers a solution to this problem. Its application to the $SU(2)_L \times U(1)_Y$, proposed by Glashow, Salam and Weinberg [15, 16], brings masses to both fermions and bosons without affecting the gauge-invariance of the theory.

1.2 The Higgs mechanism

The simplest solution consists of adding one $SU(2)_L$ doublet of spin-0 fields Φ (called Higgs doublet) with the associated Lagrangian

$$\mathcal{L}_h = |D_\mu \Phi|^2 - V(\Phi) = |D_\mu \Phi|^2 - \mu^2 |\Phi|^2 - \lambda |\Phi|^4. \tag{1.8}$$

The covariant derivative is

$$D_\mu = \partial_\mu - ig A^i_\mu(x) \tau^i - ig' Y B_\mu, \tag{1.9}$$

where A^i_μ and B_μ are, respectively, the $SU(2)_L$ and $U(1)_Y$ gauge bosons. Y is the hypercharge of the field to which the derivative is applied.

If $\mu^2 < 0$, the potential $V(\Phi)$ has a minimum for

$$\Phi_0 = \begin{pmatrix} 0 \\ \sqrt{-\mu^2/(2\lambda)} \end{pmatrix} \equiv \frac{1}{\sqrt{2}} \begin{pmatrix} 0 \\ v \end{pmatrix}, \tag{1.10}$$

modulo a global phase transformation that can be dropped without loss of generality.

Since this value is not invariant under $SU(2)_L \times U(1)_Y$, the expansion of the Φ field around its ground state breaks the original gauge symmetry. However, to have a good description of electromagnetism, a residual $U(1)_{EM}$ symmetry must remain unbroken. An opportune choice of the Higgs doublet hypercharge ($Y = 1/2$) ensures Φ_0 to be

electrically neutral, thus preserving this symmetry. Similarly, fermion hypercharges are adjusted to reproduce their observed electric charges.

Expanding Φ around its minimum, i.e.

$$\Phi(x) = \frac{1}{\sqrt{2}} \begin{pmatrix} \eta_1(x) + i\eta_2(x) \\ v + h(x) + i\eta_3(x) \end{pmatrix}, \tag{1.11}$$

leads to a scalar Higgs boson h with tree level mass $m_{h,0}^2 = 2\lambda v^2$ and to three heavy vector bosons, whose masses emerge from the covariant derivative:

$$|D_\mu \Phi|^2 = \frac{v^2}{8} \left[g^2 (A_\mu^1)^2 + g^2 (A_\mu^2)^2 + (-g A_\mu^3 + g' B_\mu)^2 \right] + \dots . \tag{1.12}$$

We have now the three massive bosons $W_\mu^\pm \sim A_\mu^1 \mp i A_\mu^2$ and $Z_\mu^0 \sim g A_\mu^3 - g' B_\mu$, mediators of the weak interactions. The fourth gauge field, given by the combination $g' A_\mu^3 + g B_\mu$ orthogonal to Z_μ^0, remains massless and is identified with the photon. The real scalar fields $\eta_{1,2,3}$ are massless Goldstone bosons, which can be removed from the theory by making a particular choice of gauge.

The ellipses in Equation 1.12 contain couplings between two gauge bosons and one or two Higgs fields, with strengths proportional to the vector boson masses. From a phenomenological point of view, this means that the Higgs boson decays mainly into heavy particles, at least when kinematically allowed. Additional cubic and quartic Higgs self-interactions derive from the last term of Equation 1.8.

Finally, quark and lepton masses arise from Yukawa couplings between fermions and the scalar fields. For example, for quarks:

$$-\lambda_u^{i,j} \left(\bar{u}_L^i \ \bar{d}_L^i \right) \Phi^\dagger u_R^j - \lambda_d^{i,j} \left(\bar{u}_L^i \ \bar{d}_L^i \right) \Phi d_R^j + \text{H.c.}, \tag{1.13}$$

where we have split each quark family into one $SU(2)_L$ doublet and two right-handed singlets and where u^i stands for an up quark field (u, c or t) and d^i for a down quark field (d, s or b). After symmetry breaking, the diagonalized $m_{u,d} = (v/\sqrt{2})\lambda_{u,d}$ matrices determine the quark mass values. The masses for the three lepton families (ν_ℓ, ℓ), $\ell = e, \mu, \tau$, are obtained in the same way, with the only exception that neutrino masses are experimentally negligible and thus the λ_{ν_ℓ} are set to zero and the completely non-interacting right-handed neutrinos are removed. It should be notice that the Yukawa couplings between the Higgs and the fermion pairs are again proportional to the fermion masses.

Names		Spin	$SU(3)_C$	$U(1)_{EM}$
quarks (q)	$Q = (u_L, d_L)$	1/2	**3**	$(2/3, -1/3)$
($\times$ 3 families)	u_R	1/2	**3**	$2/3$
	d_R	1/2	**3**	$-1/3$
leptons	$L = (\nu_L, \ell_L)$	1/2	**1**	$(0, -1)$
($\times$ 3 families)	ℓ_R	1/2	**1**	-1
gluons	g	1	**8**	0
W and Z bosons	W, Z	1	**1**	$\pm 1, 0$
photon	γ	1	**1**	0
Higgs boson	h	0	**1**	0

Table 1.1: Particle content of the Standard Model, comprising the yet undiscovered Higgs boson.

Table 1.1 summarizes the complete particle content of the Standard Model, with the associated quantum numbers and $SU(3)_C$ representations.

Since the three massive weak bosons have been observed, the spontaneous breaking of the electroweak symmetry is now an experimentally well established fact. However, the predicted Higgs boson is still undetected and thus the details of the mechanism that induces spontaneous breaking of the gauge symmetry are still unknown. The presented one Higgs doublet is the minimal solution but other models involving two doublets or a triplet of scalar fields have been proposed. These are reviewed in [17], with particular attention in their phenomenological implications.

1.3 Precision tests

The most impressive quantitative confirmations of the validity of the Standard Model come from precision measurements in the electroweak sector. Such observables can give valuable information about the last missing parameter, m_h, and also restrict the existence of new particles not contained in the Standard Model.

Here, we will focus our attention on the anomalous magnetic moment of electron and muon, on tests of flavour physics and on the W boson mass.

1.3.1 Lepton magnetic moments

The magnetic moment produced by an electric charge moving along a circular path is proportional to its angular moment:

$$\vec{\mu} = \frac{e}{2m}\vec{L}. \tag{1.14}$$

Similarly, since elementary particles carry an intrinsic angular moment $\vec{S}$, called spin, their associated magnetic moment is

$$\vec{\mu} = g\frac{e}{2m}\vec{S}, \tag{1.15}$$

where g is called gyromagnetic constant.

In the Dirac theory of a charged particle, g is equal to 2. In quantum field theories, loop effects, such as emission and absorption of virtual particles, produce a correction to this value.

The most recent measurement of the electron magnetic moment has the fabulous accuracy of 0.76 part per trillion [18]

$$(g/2)_e = 1.001\ 159\ 652\ 180\ 85\ (76), \tag{1.16}$$

reducing by 6 times the standard deviation with respect to the previous 1987 measurement [19]. The QED calculation plus a small contribution coming from the weak and hadronic sector of the Standard Model, combined with the independent measurements of $\alpha = e^2/4\pi$ [20, 21], show an accord at less than 15×10^{-12}, giving a beautiful confirmation of the validity of the theory. Moreover, the achieved experimental uncertainty on g will allow a 10 times more demanding test if the uncertainty on the independent determination of α can be reduced.

The muon magnetic moment, even though its uncertainty is about a thousand times larger, can better constraint the presence of new physics beyond the Standard Model, since contributions from heavy particles are much larger.

The discrepancy of the actual value from the theoretical prediction is about 3 standard deviations:

$$\begin{aligned} (g/2)_\mu^{\mathrm{exp}} &= 1.001\ 165\ 920\ 80\ (63)\ [22] \\ (g/2)_\mu^{\mathrm{th}} &= 1.001\ 165\ 918\ 05\ (56)\ [23]. \end{aligned} \tag{1.17}$$

Physicists start looking to this effect as a possible signal of the presence of new particles and interactions not yet directly observed [24, 25, 26].

A new experiment has been proposed [27] and, together with further improvement on the theory side, the error on the $(g/2)_\mu^{\rm exp} - (g/2)_\mu^{\rm th}$ could be reduced by a factor 2.

1.3.2 Flavour physics

The different families of quarks and leptons are usually referred to as flavours. Constraining flavour changing processes is a powerful test of Standard Model. Indeed, before including Higgs Yukawa couplings, the Standard Model Lagrangian has an incidental symmetry under $U(3)^5$, where $U(3)$ groups are associated to the flavour exchange respectively of the left-quark doublet, right-u-quark singlet, right-d-quark singlet, left-lepton doublet and right-charged-lepton singlet. Again, right-handed neutrinos are neglected.

The introduction of flavour dependent Yukawa couplings explicitly breaks this large symmetry, leaving a smaller residual symmetry, associated to the conservation of the total quark (baryonic) number and of three separate lepton flavour numbers.

In the lepton sector, a striking confirmation is represented by the experimental 90% confidence level upper limits on the muon decay rate to electron [28]:

$$\begin{aligned} BR(\mu^- \to e^-\gamma) &< 1.2 \times 10^{-11} \\ BR(\mu^- \to e^-e^+e^-) &< 1.0 \times 10^{-12}. \end{aligned} \tag{1.18}$$

In the quark sector, flavour changing currents are not forbidden but yet strongly constrained. Indeed, after the diagonalization of the Yukawa matrices in Equation 1.13, the Lagrangian must be expressed in terms of the physical mass eigenstates

$$\begin{pmatrix} u \\ c \\ t \end{pmatrix} \to V^u \begin{pmatrix} u \\ c \\ t \end{pmatrix} \text{ and } \begin{pmatrix} d \\ s \\ b \end{pmatrix} \to V^d \begin{pmatrix} d \\ s \\ b \end{pmatrix}. \tag{1.19}$$

In the new basis the couplings to charged W boson, that before the introduction of Yukawa's would allow only for $u \leftrightarrow d$, $c \leftrightarrow s$, $t \leftrightarrow b$ transitions, now become non-diagonal and flavour changing processes are specified by the so-called Cabibbo-Kobayashi-Maskawa (CKM) mixing matrix $V_{\rm CKM} = V^u V^{d\dagger}$.

On the other hand, neutral currents like u-u-Z and d-d-Z are unaffected, since basis transformations only add a harmless $V^u V^{u\dagger} = V^d V^{d\dagger} = \mathbf{1}$. Thus, in the Standard Model contributions to flavour changing neutral currents can be found only in diagrams with at least one loop of virtual particles. Consequently, measurements of such processes, as for example $BR(b \to s\gamma)$, provide stringent tests.

1.3.3 W boson mass

The relation between the heavy gauge boson masses is determined in terms of the electromagnetic fine structure constant α and the Fermi constant G_{F}, measured from the cross-sections of weak processes:

$$m_W \left(1 - \frac{m_W^2}{m_Z^2}\right) = \frac{\pi\alpha}{\sqrt{2}G_{\mathrm{F}}}(1 + \Delta r). \tag{1.20}$$

Loop corrections enter via Δr. In the Standard Model these are dominated by top quark and Higgs loops.

Exploiting this relationship, the experimental results at the Z-pole [29] allow to predict the masses of heavy fundamental particles, such as the top quark and the W boson, which are then compared to the direct measurements. This checks the correctness of the prediction and thus of the theory in this area. Figure 1.1 displays this comparison for m_W [30].

The current value from direct measurements is based on a combination of the latest LEP [31] and Tevatron results [32, 33]. Particularly interesting is the measurement from the NuTeV experiment, which published its final result on the ratio of neutral current to charged current reactions in neutrino-nucleon scattering [34]. Interpreting this result as a measurement of the mass of the W boson gives a 2.5 standard deviation discrepancy.

1.4 Higgs mass limits

Besides the successful precision tests, the Standard Model still has a missing item: the Higgs boson. While the value of $v = (2\sqrt{2}G_{\mathrm{F}})^{-1/2} \simeq 246$ GeV is fixed by the measurements of the weak interaction rates, the Higgs boson mass is not theoretically

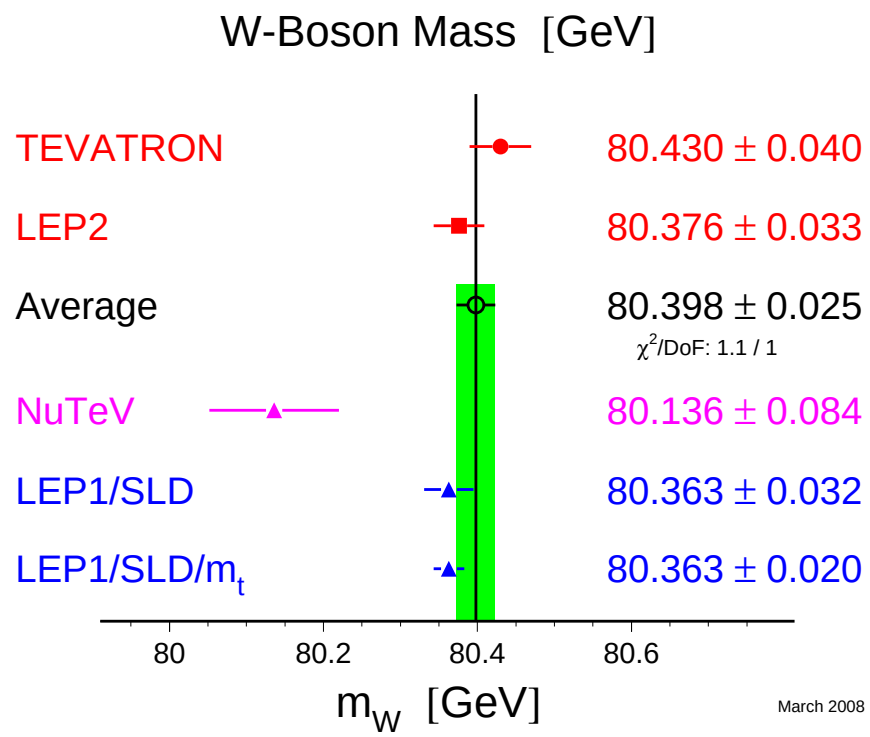

Figure 1.1: Different W boson mass measurements. The top part shows the direct measurements, the bottom part shows the indirect constraints valid within the Standard Model [30].

predicted. However, it is constrained by direct searches at LEP and a fit to electroweak precision observables can also suggest a preferred value, as we review in the following.

1.4.1 Experimental limit on the Higgs boson mass

The present experimental lower limit on the Standard Model Higgs boson has been established from direct searches at LEP. At the end of the data taking the four LEP experiments (ALEPH, DELPHI, L3 and OPAL) have collected 2461 pb^{-1} of e^+e^- collision data with centre-of-mass energy from 189 to 209 GeV.

At LEP the Higgs boson is expected to be produced mainly in association with a Z boson and, for the benchmark Higgs mass of $m_h = 115$ GeV, it is predicted to decay in $b\bar{b}$ pairs with a branching ratio of 74%. The most relevant final states are the four following:

1. $e^+e^- \to (h \to b\bar{b})(Z \to q\bar{q})$, which is the most abundant channel with a branching ratio of about 60% for $m_h = 115$ GeV;

2. the missing energy topology, produced mainly in the $e^+e^- \to (h \to b\bar{b})(Z \to \nu_\ell\bar{\nu}_\ell)$ process and occurring with a branching ratio of about 17%;

3. the process $e^+e^- \to (h \to b\bar{b})(Z \to e^+e^-/\mu^+\mu^-)$, that, although its branching ratio is only about 6%, has a low background and thus provides good sensitivity;

4. the τ-lepton pair final state, with a branching ratio of about 10% and produced in the processes $e^+e^- \to (h \to b\bar{b})(Z \to \tau^+\tau^-)$ and $e^+e^- \to (h \to \tau^+\tau^-)(Z \to q\bar{q})$.

For collision energies of 189 GeV, the Z boson in the final state is virtual and only channel 2 and 3 can be used, because of prohibitive background in the other final states. After the machine upgrade ($\sqrt{s} \geq 206$ GeV), the Z boson produced is on mass shell, yielding additional separation power. Thus all four search topologies can be exploited.

After the LEP machine shutdown an extensive and refined analysis work has been carried out combining statistically the data of the four LEP experiments in different decay channels and at different centre-of-mass energies [35]. This work sets a 95% confidence level lower bound at 114.4 GeV.

A more stringent experimental lower bound (or even an evidence or observation) could come in the next years from the CDF and D0 experiments at the Tevatron collider.

In Figure 1.2, we report the most recent, but still preliminary, exclusion plot, obtained for integrated luminosities varying from 0.3 to 1 fb^{-1}, depending on the Higgs decay channel [36]. The expected and observed lower limits on the Higgs production cross-section (expressed in units of the SM prediction) are shown over the accessible mass range, from 115 to 200 GeV. The two most sensitive regions are for $m_h < 120$ GeV, where evidence for Higgs signals are mainly searched for in the $b\bar{b}$ channel, and for 150 GeV $< m_h <$ 170 GeV, with the $h \to WW$ decay mode as the most promising analysis.

The Higgs searches at the Tevatron collider mainly rely on the machine luminosity. The reach of 6 fb^{-1} of integrated luminosity per experiment by the year 2009 seems now very possible; that will probably allow to set a new 95% confidence level limit on m_h.

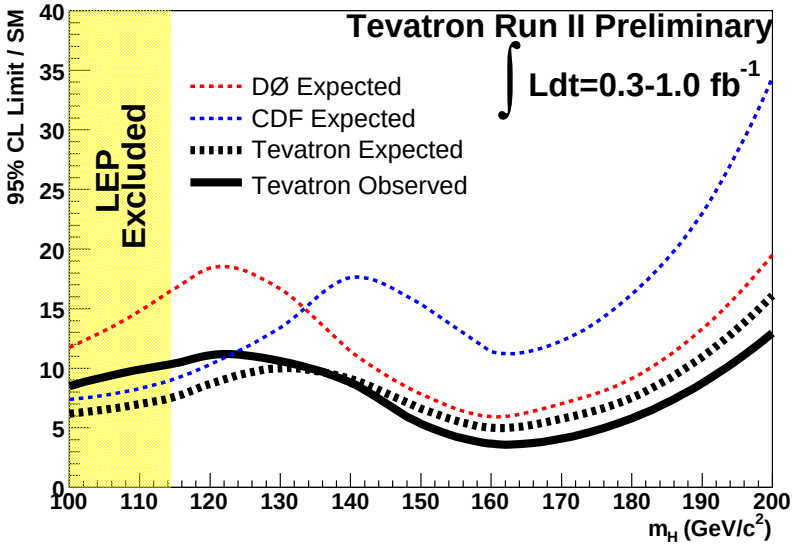

Figure 1.2: Preliminary Higgs exclusion plot from Tevatron experiments CDF and D0 [36]. The expected and observed lower limits on the Higgs production cross-section (expressed in units of the SM prediction) are shown over the accessible mass range, from 115 to 200 GeV. The integrated luminosity varies from 0.3 to 1 fb^{-1}, depending on the Higgs decay channel.

1.4.2 Electroweak precision observables fit of the Higgs mass

As pointed out in Section 1.3, the measured values of electroweak observables are sensitive to the presence of unobserved particles, which contribute to the radiative corrections via virtual loops.

A global fit to the precision observables can be used to extract a best value for the only unknown Standard Model parameter, the Higgs boson mass. The most recent result of such fit is summarized by the $\Delta\chi^2$ distribution reported in Figure 1.3 [30]. The curve presents a minimum for $m_h = 87^{+36}_{-27}$ GeV.

Though the derived 95% confidence level upper bound of 160 GeV is still compatible with the lower bound by LEP, a tension between the two results is present.

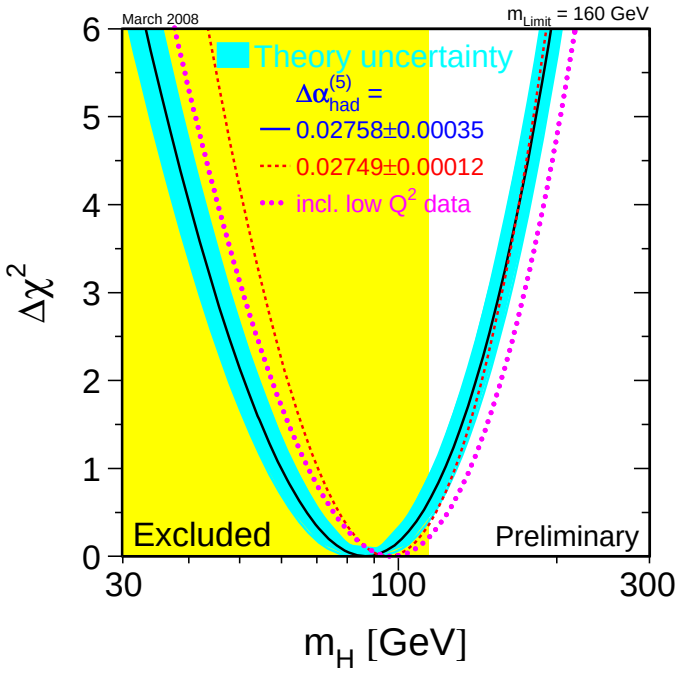

Figure 1.3: Distribution of the $\Delta\chi^2$ of the Standard Model fits to electroweak precision data, as a function of the Higgs boson mass [30].

1.5 What is missing?

Even if the presence of a Higgs boson would be experimentally confirmed, it is believed that the Standard Model is not the ultimate theory of particle physics. Indeed, observations such as cosmological dark matter [37, 38, 39, 40, 28], the baryon asymmetry in the universe [38, 39, 28] and neutrino masses and oscillations [41, 42, 43, 44, 28, 45] suggest the existence of new phenomena at present not yet observed.

Moreover, the naturalness problem that fundamental scalar particles bring to quantum field theory suggests that the Standard Model should be valid up to the TeV energy scale, at which it would break down leaving room for new particles and interactions. In fact, since no symmetry prevents the mass of scalar particles from receiving large radiative corrections, the Higgs mass becomes as large as the largest energy scale in the theory. For example, if the Higgs field couples to a fermion with mass m_f through

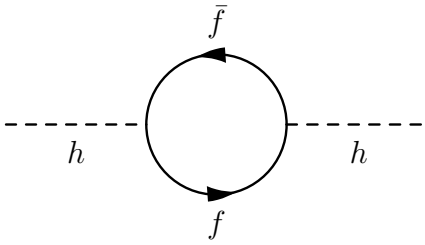

Figure 1.4: Feynman diagrams of the quantum correction from fermion loop to the Higgs squared mass.

a Yukawa interaction with strength λ_f, the Feynman diagram in Figure 1.4 yields a correction to the tree level Higgs mass

$$\Delta m_h^2 = \frac{\lambda_f^2}{8\pi^2}\left(-\Lambda_{\mathrm{UV}}^2 + 6m_f^2 \ln\frac{\Lambda_{\mathrm{UV}}}{m_f} + \dots\right). \tag{1.21}$$

The correction is proportional to the ultraviolet energy cut-off used to regularize the loop integral.

Assuming $\Lambda_{\mathrm{UV}} \sim \Lambda_{\mathrm{Planck}} \sim 10^{19}$ GeV, only an unnatural cancellation, called fine tuning, between the tree level Higgs mass and its correction would give the suitable value of $m_h \sim \Lambda_{\mathrm{EW}} \sim 100$ GeV. If we think that theory should not require this strange cancellation, we will conclude that $\Lambda_{\mathrm{UV}} \lesssim 1$ TeV and the Standard Model is just an effective low energy theory of some more fundamental theory, appearing at the TeV scale.

This problem of quadratically divergent mass is endemic to spin-zero fields. In fact, chiral symmetry and gauge symmetry protect respectively fermions and gauge bosons masses from receiving large radiative corrections.

A particularly surprising coincidence is that the interpretation of cosmological dark matter in terms of weakly interacting massive particles (WIMP's) also suggests new physics at the TeV scale [46, 47]. Indeed, if we assume the WIMP's to constitute dark matter and, furthermore, that they were in thermal equilibrium for some period in the early universe, we can deduce its cosmological relic density as a function of the thermal average of the dark matter pair annihilation cross-section times their relative average

velocity [48]

$$\Omega_{\rm cdm} h^2 \simeq \frac{0.1 \text{ pb}}{\langle \sigma v \rangle}. \tag{1.22}$$

Combining this result with the experimental estimate of dark matter density $\Omega_{\rm cdm} h^2 \sim 0.1$ we find $\langle \sigma v \rangle \sim 1$ pb. Interpreting this in terms of the WIMP mass, using $\langle \sigma v \rangle = \pi \alpha^2 / 8 m^2$, we find it to be of the order of magnitude of $m \sim 100$ GeV.

This remarkable connection between cosmology and particle physics pushes physicists to think that extensions of the Standard Model must also include a dark matter candidate.

2

THE MINIMAL SUPERSYMMETRIC STANDARD MODEL

2.1 The supersymmetric solution

At the end of the last chapter, we pointed out that the Higgs boson mass suffers from quadratically divergent corrections. Thus, unless an unnatural cancellation between its tree-level value and its radiative corrections is assumed, the Higgs mass is pushed more than 16 orders of magnitude away from the value required for the electroweak interactions.

However, if one supposes that a complex scalar particle with mass m_s exists and couples to the Higgs through a λ_s constant, then the left diagram in Figure 2.1 will give a contribution to m_h equal to

$$\Delta m_h^2 = \frac{\lambda_s}{16\pi^2}\left(\Lambda_{\mathrm{UV}}^2 - 2m_s^2 \ln\frac{\Lambda_{\mathrm{UV}}}{m_s} + \dots\right). \tag{2.1}$$

It is worth noting the relative minus sign between Equation 1.21 and 2.1. If each of the quarks and leptons of the Standard Model is accompanied by two complex scalar fields with $\lambda_s = \lambda_f^2$, then the quadratic divergences cancel. Actually, the presence of such bosonic partners can be the result of a new symmetry relating bosons and fermions, called supersymmetry (SUSY).

To prove that supersymmetry really provides the desired particle content, we shall examine the supersymmetry algebra. In quantum theory, a generator Q of supersymmetry must turn a bosonic state into a fermionic one and vice versa, thus they must

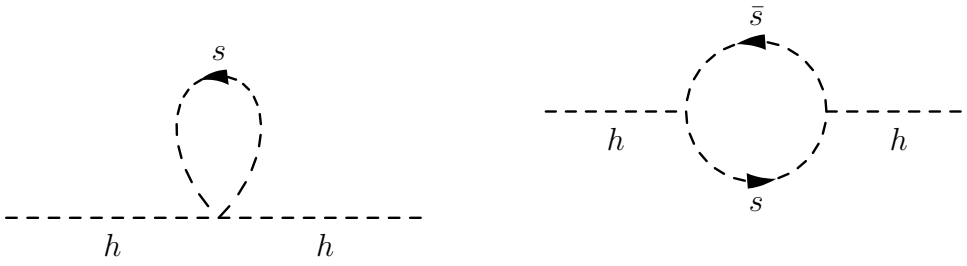

Figure 2.1: Feynman diagrams of the quantum correction from scalar loops to the Higgs squared mass.

carry spin angular momentum 1/2, as opposed to the Lorentz group or gauge group generators, all of which are bosonic. Since spinors are complex objects, the Hermitian conjugate of Q, $Q^\dagger$, is also a supersymmetry generator.

As Q and $Q^\dagger$ are conserved, so is their anti-commutator. This implies the existence of a conserved quantity that does not transform trivially under the Lorentz transformations, i.e. schematically:

$$\{Q, Q^\dagger\} = QQ^\dagger + Q^\dagger Q = P_\mu. \tag{2.2}$$

However, the form of the conserved four-vector P_μ is highly restricted by the Haag-Lopuszanski-Sohnius extension of the Coleman-Mandula no-go theorem [49, 50]. It states that in a relativistic quantum field theory with a conserved four-vector charge in addition to the energy-momentum there can be no scattering and so the theory is trivial. For instance, in two-body scattering, for fixed centre-of-mass energy, energy-momentum conservation leaves only two degrees of freedom, the two scattering angles. A second conserved four-vector would forbid almost all their possible values. Then P_μ must be the energy-momentum generator of space-time translations.

In general, it is possible to have $N \geq 1$ distinct copies of the supersymmetry generators Q, but phenomenological problems restrict the choice to $N = 1$, at least in four-dimensional field theories.

The particle states of supersymmetric theories, which are called supermultiplets, must be representations of the supersymmetry algebra. Their content in terms of bosonic and fermionic states can be derived from the algebra definition of Equation 2.2.

Consider the operator $(-1)^s$, where s is the spin angular momentum. For any representation of the algebra

$$\begin{aligned} \mathrm{Tr}[(-1)^s P_\mu] &= \mathrm{Tr}[(-1)^s Q Q^\dagger + (-1)^s Q^\dagger Q] = \\ &= \mathrm{Tr}[(-1)^s Q Q^\dagger + Q(-1)^s Q^\dagger] = \\ &= \mathrm{Tr}[(-1)^s Q Q^\dagger - (-1)^s Q Q^\dagger] = 0. \end{aligned} \tag{2.3}$$

The equality in the second line follows from the cyclic property of the trace, while in the third line we have used the fact that, since Q turns a boson into a fermion and vice versa, Q must anti-commute with $(-1)^s$. For fixed momentum, $\mathrm{Tr}[(-1)^s P_\mu]$ is simply proportional to the number of bosonic degree of freedom minus the number of fermionic degree of freedom. Therefore each supermultiplet contains the same number of fermionic and bosonic degrees of freedom.

Furthermore, supermultiplets own other interesting properties. By definition, two states residing in the same supermultiplet are related by some combination of Q and $Q^\dagger$. Since Q and $Q^\dagger$ do not carry Lorentz indices, they commute with P_μ and, thereby, with P^2; as a consequence, all the states within the same supermultiplet have equal masses. The supersymmetry generators also commute with the generators of gauge transformation and so particles in the same supermultiplet must also have identical gauge quantum numbers.

With such particle content, supersymmetry guarantees the cancellation of quadratic divergences, not only at one loop, as showed previously, but also at all orders in perturbation theory. Actually under exact supersymmetry, the whole fermionic and bosonic contributions completely cancel, giving a vanishing total correction to scalar masses. At one-loop order, this can be easily verified by adding to Equation 2.1 the amplitude of the right diagram in Figure 2.1 and setting $m_s = m_f$.

Though, supersymmetry is not an exact symmetry of nature, otherwise a bosonic partner of the electron with mass equal to $m_e \simeq 511$ keV would have been discovered long time ago; we have no experimental evidence of the existence of any supersymmetric partner of the SM particles up-to-date.

Thus, supersymmetry must be broken.

However, if supersymmetry is still to solve the naturalness problem, the breaking terms in the Lagrangian must not reintroduce the quadratic divergences in radiative corrections to the scalar masses. This class of terms is referred to as soft supersymmetry

breaking and leaves in the Δm_h^2 only logarithmic terms of Λ_{UV}:

$$\Delta m_h^2 \propto m_{\mathrm{soft}}^2 \ln \frac{\Lambda_{\mathrm{UV}}}{m_{\mathrm{soft}}} + \ldots, \tag{2.4}$$

where m_{soft} is the mass scale associated with the breaking terms, for example the mass splitting between SM particles and their supersymmetric partners.

From Equation 2.4, it must be clear that supersymmetric particles cannot be too heavy, but rather have masses of order 1 TeV at most, in order not to create again a fine tuning problem between the tree level Higgs mass and its correction, which is proportional to m_{soft}^2.

In the next sections, we review the supersymmetric extension of the Standard Model with the minimal possible addition of particles, the Minimal Supersymmetric Standard Model (MSSM).

2.2 Particles and interactions

The MSSM [51, 52, 53, 54] is constructed by placing each of the known particles in supermultiplets and subsequently adding its associated supersymmetric partner (or simply superpartner).

As each supermultiplet contains the same number of fermionic and bosonic degrees of freedom, the simplest possibilities are supermultiplets comprising:

- a two-component Weyl spinor and a complex scalar field (called chiral or matter supermultiplet);
- a massless gauge boson, which has two helicity states, and a two-component Weyl spinor (called gauge supermultiplet); gauge bosons can eventually acquire masses after the gauge symmetry is spontaneously broken.

In renormalizable supersymmetric field theories with only one SUSY generator Q, all possible forms of supermultiplets are combinations of these two.

Since the SM fermions reside in different representations of the gauge group than the gauge bosons, none of them can be identified with the superpartner of a gauge boson. Therefore we have to place them in chiral supermultiplets. Then, one gauge supermultiplet is needed per gauge boson.

The left-handed and right-handed parts of quarks and leptons are different two-component Weyl spinors, with different gauge properties, and each of them is accompanied by a new complex scalar field. By convention, the names of scalar superpartners are obtained by adding the prefix s to the SM particle names, for example sleptons, squarks or, collectively, sfermions. Sfermions can be left- or right-handed, referring to the helicity state of their SM partner.

The supersymmetric copies of gauge bosons are Weyl fermions and are called gauginos. In particular, the names of the partners of the gluon, W, Z and photon are the gluino, wino, zino and photino. The composition of zino and photino in terms of the original (i.e. before gauge symmetry breaking) massless $SU(2)_L$ and $U(1)_Y$ gauginos is the same as of Z and photon in terms of the massless $SU(2)_L$ and $U(1)_Y$ gauge bosons. Equivalently, if supersymmetry were unbroken, the zino and photino masses would be exactly m_Z and 0.

For reason that are postponed to Section 2.3, the one Higgs doublet model providing the $SU(2)_L \times U(1)_Y$ breaking does not work in supersymmetric extensions of the SM. The minimal choice for the Higgs sector is a pair of complex scalar $SU(2)_L$ doublets, with hypercharge $Y = +1/2$ and $-1/2$ respectively, that we will mark as

$$\begin{pmatrix} H_u^+ \\ H_u^0 \end{pmatrix} \text{ and } \begin{pmatrix} H_d^0 \\ H_d^- \end{pmatrix}. \tag{2.5}$$

These Higgs fields can only fit in chiral supermultiplets, together with four spin-1/2 higgsinos. After the scalar doublets acquire a non-zero ground state expectation value, three of the initial eight degrees of freedom become the longitudinal helicity states of the $W^\pm$ and Z^0 bosons. The remaining five turn into as many scalar fields: two neutral CP-even, the lightest called h, the heaviest H^0, one neutral CP-odd, A^0, and a positive and a negative one, $H^\pm$.

All new supersymmetric particles are represented by the symbols of the associated SM fields superposed by a tilde. Table 2.1 summarizes the new supersymmetric particles and Higgs bosons predicted by the MSSM. However, the supersymmetric particles listed are not necessarily the mass eigenstates of the model. Indeed, after symmetry breaking, particles with the same set of quantum numbers in general mix. This is the case for the charged $\tilde{W}^\pm$, $\tilde{H}_u^+$, $\tilde{H}_d^-$ and for the neutral $\tilde{Z}$, $\tilde{\gamma}$, $\tilde{H}_u^0$, $\tilde{H}_d^0$. The former combine to give two charginos $\tilde{\chi}_1^\pm$, $\tilde{\chi}_2^\pm$, while the latter mix-up into four neutralinos $\tilde{\chi}_1^0$, $\tilde{\chi}_2^0$,

Names		Spin	$SU(3)_C$	$U(1)_{EM}$
squarks ($\tilde{q}$)	$\tilde{Q} = (\tilde{u}_L, \tilde{d}_L)$	0	**3**	$(2/3, -1/3)$
($\times$ 3 families)	$\tilde{u}_R$	0	**3**	$2/3$
	$\tilde{d}_R$	0	**3**	$-1/3$
sleptons	$\tilde{L} = (\tilde{\nu}_L, \tilde{\ell}_L)$	0	**1**	$(0, -1)$
($\times$ 3 families)	$\tilde{\ell}_R$	0	**1**	-1
gluinos	$\tilde{g}$	1/2	**8**	0
winos, zino	$\tilde{W}, \tilde{Z}$	1/2	**1**	$\pm 1, 0$
photino	$\tilde{\gamma}$	1/2	**1**	0
Higgsinos	$\tilde{H}_u = (\tilde{H}_u^+, \tilde{H}_u^0)$	1/2	**1**	$(1, 0)$
	$\tilde{H}_d = (\tilde{H}_d^0, \tilde{H}_d^-)$	1/2	**1**	$(0, -1)$
Higgs bosons	h, H^0, A^0	0	**1**	$0, 0, 0$
	$H^\pm$	0	**1**	± 1

Table 2.1: Supersymmetric particles and Higgs bosons predicted by the MSSM, before mixing between states with the same set of quantum numbers occurs.

$\tilde{\chi}_3^0$, $\tilde{\chi}_4^0$. The subscripts indicate the order of the mass eigenvalues from the lightest to the heaviest. Also left- and right-handed sfermions in general mix. The corresponding lightest and heaviest mass eigenstates have subscripts 1 and 2 instead of L and R.

Now that we have drawn a picture of the particle content of the MSSM, we can outline the interactions between the different constituents. A complete and accurate discussion of the full Lagrangian and the deriving Feynman rules can be found in [55].

After writing down the kinetic terms for the fields of the theory, the local gauge invariance requires the substitution of ordinary derivatives with covariant derivatives for scalar and fermions, analogously to Sections 1.1 and 1.2. From this simple procedure, the gauge interactions already present in the SM arise for fermions and scalars in chiral supermultiplets:

- gauge-fermion-fermion;
- gauge-scalar-scalar;
- gauge-gauge-scalar-scalar.

The invariance of the Lagrangian under supersymmetry transformations is ensured by the presence of the interactions:

- gaugino-scalar-fermion;
- $(\text{Higgs})^4$.

Their strengths are fixed to be gauge couplings by the requirements of supersymmetry, even though they are not gauge interactions from the point of view of an ordinary field theory. Of course, the existence of gauge couplings for a specific chiral supermultiplet depends on its gauge charges; for instance, neither a pair of neutrinos nor a pair of sneutrinos interact with the photon, since they are electrically neutral.

For non-abelian gauge groups, in addition to the usual gauge boson cubic and quartic self-interactions, a coupling between vector bosons and their superpartners emerges, since, in this case, also the covariant derivative of gauginos contains a part proportional to the gauge field. Thus, the following interactions exist:

- $(\text{gauge})^3$;
- $(\text{gauge})^4$;
- gauge-gaugino-gaugino.

The most general supersymmetric non-gauge interactions are described by the Lagrangian:

$$-\frac{\partial W}{\partial \phi_i}\left(\frac{\partial W}{\partial \phi_i}\right)^* - \frac{1}{2}\left(\frac{\partial W}{\partial \phi_i \partial \phi_j}\psi_i\psi_j + \text{c.c.}\right), \tag{2.6}$$

where ϕ_i and ψ_i are the bosonic and fermionic components of the chiral supermultiplets and W is an analytic function of the scalar fields. Thus, once the gauge transformation properties of the fields are defined, the only missing input to build all the interactions of a supersymmetric theory is W, the superpotential. In the MSSM, it is:

$$W = \tilde{u}_R^{*i}\lambda_u^{i,j}\tilde{Q}^j H_u - \tilde{d}_R^{*i}\lambda_d^{i,j}\tilde{Q}^j H_d - \tilde{\ell}_R^{*i}\lambda_\ell^{i,j}\tilde{L}^j H_d + \mu H_u H_d. \tag{2.7}$$

The matrices $\lambda_{u,d,\ell}$ are equivalent to those in Equation 1.13 and μ corresponds to the Standard Model Higgs mass parameter of Equation 1.8. The generated vertices are:

- $(\text{Higgs})^2$, $(\text{higgsino})^2$;

- (Higgs)^2-(slepton)^2, (Higgs)^2-(squark)^2, (slepton)^2-(squark)^2;
- Higgs-(slepton)^2, Higgs-(squark)^2;
- Higgs-lepton-lepton, Higgs-quark-quark;
- higgsino-slepton-lepton, higgsino-squark-quark.

2.3 The Higgs sector

In Section 2.2, we anticipated that the Higgs sector of any supersymmetric extension of the SM model must contain at least two Higgs doublets. There are at least two reasons for this.

First, a single Higgs doublet would introduce a gauge anomaly, violating the local invariance of the model and causing the quantum theory to be inconsistent. Indeed, in the triangular Feynman diagram with one photon and two $SU(2)_L$ bosons at the vertices receive contributions from the loops of all the left-handed charged fermions. In the Standard Model the resulting total current vanishes and the gauge symmetry is preserved. The addition of a single left-handed charged higgsino would destroy this remarkable cancellation. Two Higgs doublet with opposite hypercharges, instead, would be accompanied by two left-handed higgsinos whose contributions to the anomalous current cancel each other.

The second motivation relies on the structure of supersymmetric theories and in particular to the superpotential. Indeed, since it must be analytic, it cannot contain both H_u and its complex conjugate. At the same time, the first term of the MSSM superpotential (Equation 2.7) needs a Higgs doublet with $Y = +1/2$ while the second and third require a Higgs doublet with $Y = -1/2$. If we leave out one of the Higgs multiplets, some quarks or leptons will be left massless.

2.4 R-parity

The superpotential defined in Equation 2.7 does not contain all the renormalizable terms allowed by the gauge invariance of the MSSM. However, the inclusion of terms

like

$$\tilde{L}^i \tilde{L}^j \tilde{\ell}_R^{*k}, \quad \tilde{L}^i \tilde{Q}^j \tilde{\ell}_R^{*k}, \quad \tilde{L}^i H_u, \quad \tilde{u}_R^{*i} \tilde{d}_R^{*j} \tilde{d}_R^{*k} \tag{2.8}$$

would lead to the violation of leptonic and baryonic numbers, already discussed in Section 1.3. This is rather disturbing, since such processes are severely constrained by experiments.

To prevent any undesired effect, we can postulate the conservation of the baryonic and leptonic numbers. However, this is clearly a step backward from the situation of the SM, where the preservation of these quantum numbers is an accidental consequence of the renormalizability. Even more important, baryonic and leptonic numbers are known to be violated by non-perturbative electroweak effects negligible for all ordinary energy experiments, but important for models describing the early universe. Therefore in the MSSM, instead of the baryonic and leptonic number conservation, a new discrete symmetry, called R-parity, is required.

R-parity is a defined as

$$R = (-1)^{B-L+2s}. \tag{2.9}$$

Quarks and anti-quarks have, respectively, $B = \pm 1$ and $L = 0$, while leptons and anti-leptons have $L = \pm 1$ and $B = 0$. The letter s stands for the spin. This symmetry forbids the unwanted superpotential terms, without affecting any of the others and without excluding the possibility of non-perturbative B and L violation.

It turns out that all the ordinary SM particles and the Higgs bosons have R-parity $R = +1$, while their supersymmetric partners have $R = -1$. Three important phenomenological implications follow:

- in collider experiments, sparticles are produced in even number;
- each sparticle can decay only into a state containing a odd number of sparticles;
- the lightest supersymmetric particle (LSP) is stable.

We can now have an insight into the MSSM phenomenology at colliders. After the production of a pair of sparticles, each of these decays into a SM and a SUSY particle. The two decay chains develop, resulting into a final state composed by two LSP's and a number of SM particles equal to the number of disintegration processes. Because of gauge couplings, the SM particles associated to the SUSY chains are expected to

be dominantly leptons at electron-positron colliders and quarks and gluons at hadron colliders.

The experimental signature of the passage of lightest supersymmetric particles at collider detectors is different depending on the nature of the LSP.

A neutral and weakly interacting particle crosses the detector without leaving any trace or energy deposit, behaving as a neutrino. If the detector has a full coverage of the spheric angle around the collision point, then a non-zero energy balance can be reconstructed and the missing energy of the escaped particles calculated. A LSP with such characteristics, i.e. neutral, massive, stable and weakly interacting, exactly fits our description of a possible dark matter candidate given in Section 1.5.

If the LSP is a charged slepton, it will look like a muon. However, since the slepton is heavy, its time of flight through the detector differs considerably from the muon one.

Another possibility is a coloured LSP, such as a squark or gluino. Because of colour confinement, the LSP hadronizes before crossing the detector, generating colour-singlet states called R-hadrons. The details of R-hadron interactions in matter are highly uncertain. However, the probability of an interaction between a squark or a gluino in the R-hadron and a quark in the target nucleon is low, since, according to perturbative QCD, the cross-section varies with the inverse square of the parton mass. Thus, stable R-hadrons escape the detector. But the light quarks bounded to the heavy parton may interact, causing small amount of energy losses and eventually charge flipping, providing additional discriminating signatures.

2.5 Soft SUSY breaking

Masses are added to supersymmetric particles by an explicitly soft supersymmetry breaking Lagrangian, that contains mass term for gauginos, such as $m\tilde{g}\tilde{g}$ and for scalar fields, $m^{i,j}\phi^{i*}\phi^{j}$, with i and j running on the family indices.

These are the only possible mass terms, since explicit vector boson and matter fermion masses are prohibited by gauge symmetry. This simple observation clarifies why none of the supersymmetric partners has been discovered yet. Actually, all the known particles acquire mass only through the Higgs mechanism, so they must have $m \sim v/\sqrt{2} \simeq 174$ GeV, while their superpartners have an explicit mass, that can be in

principle as high as 1 TeV.

Moreover, the scalar interactions

$$\tilde{u}_R^{*i} a_u^{i,j} \tilde{Q}^j H_u - \tilde{d}_R^{*i} a_d^{i,j} \tilde{Q}^j H_d - \tilde{\ell}_R^{*i} a_\ell^{i,j} \tilde{L}^j H_d + \text{c.c.} \tag{2.10}$$

are soft supersymmetry breaking terms and should be taken into account.

Before this section, the parameter μ in Equation 2.7 was the only newly introduced parameter. The soft SUSY breaking Lagrangian, instead, needs around a hundred new parameters: the gaugino masses, the Higgs boson masses, the 3×3 mass matrices for sleptons and squarks, the 3×3 $a_{u,d,\ell}$ complex matrices.

However, experimental evidences, especially from the flavour physics sector, already strongly constrain such parameters. For example, a non-diagonal mass matrix of sleptons would violate the stringent limits on the muon decay rate to an odd number of electrons, quoted in Equation 1.18. Equivalent arguments subsist for the mass matrix of squarks, which is restricted by limits on the flavour changing neutral currents. Under these assumptions, often called universality relations, the number of required parameters amounts to about twenty.

2.6 Spontaneous SUSY breaking

The relatively simple form of the SUSY breaking matrices deriving from experimental evidences is presumed to be the result of the existence of an underlying principle governing supersymmetry breaking. Indeed, suppose the diagonality conditions of sparticle mass matrices are exact at some very high energy scale. Then, the matrices must be evolved using the renormalization group equations (RGE) to the electroweak energy scale to perform predictions for the observables. Even though the diagonality relations are no longer exact, the flavour violating effects are enough suppressed to be compatible with experiments. Thus, the universality relations should be interpreted as high energy boundary conditions to the renormalization group equations.

Models that explain the origin of the soft supersymmetry breaking terms should address also the existence of such high energy conditions.

An interesting theoretical reason to believe in some simpler high energy principle is the unification of gauge couplings in the MSSM. The three coupling constants associated to the $SU(3)_C \times SU(2)_L \times U(1)_Y$ gauge groups can be evolved toward high

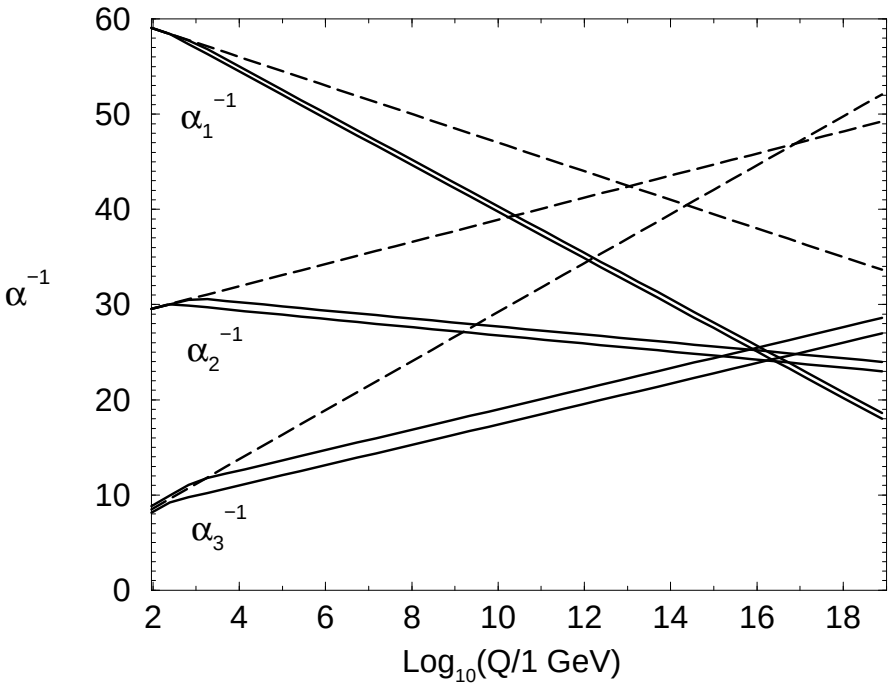

Figure 2.2: Renormalization group evolution of the inverse squared gauge couplings in the Standard Model (dashed lines) and in the Minimal Supersymmetric Standard Model (solid lines) [52]. Two loop effects are included. For the MSSM, SUSY particle masses are varied between 250 and 1000 GeV.

energies by solving the renormalization group equations. While in the Standard Model the three coupling constants fail to meet, the particle content of the Minimal Supersymmetric Standard Model give the possibility to unify the gauge couplings at the scale $\sim 10^{16}$ GeV. Figure 2.2 shows the graph of the evolution of the inverse squared gauge couplings in the SM and in the MSSM, including two loop effects [52].

The theoretical challenge is to explain the soft breaking parameters with a model for spontaneous supersymmetry breaking.

In principle, we could include in the MSSM a field whose vacuum expectation value leads to supersymmetry breaking, just as we insert a Higgs field to break the electroweak gauge symmetry. However, it has been shown that this cannot lead to phenomenologically viable models [56].

The solution is to introduce also a hidden sector which consists of some fields that do

not have any direct coupling to the visible sector containing the MSSM. Supersymmetry is spontaneously broken in this hidden sector. A weak interaction, called mediator and coupling the two sectors, then induces a supersymmetry breaking for the Standard Model particles and their superpartners. If the mediating interaction is independent of the flavour of the particles, the resulting soft supersymmetry breaking term will satisfy universality relations like those of Section 2.5.

Among the different proposals for the mediators, the most competitive two are based on gravity and on gauge interactions.

These models also offer predictive frameworks useful for phenomenological analyses of supersymmetry, since they describe all the MSSM masses and interactions in terms of few new parameters. For example, Minimal Supergravity (mSUGRA) [57, 58, 59, 60, 61, 62] is based on gravity mediation and is determined by only five parameters: three are defined at the unification energy scale, the universal mass of scalars (M_0) and fermions ($M_{1/2}$) and the strength of the cubic scalar coupling (A), while the remaining two parameters fix the Higgs sector at the electroweak scale, the ratio of the vacuum expectation values of the two Higgs doublets ($\tan\beta$) and the sign of the Higgs mass parameter in the superpotential (μ). Among the Gauge Mediated Supersymmetry Breaking (GMSB) models [63, 64], the most popular is defined by six parameters: Λ, the effective SUSY mass scale, N, the number of mediator generations, M, the mediator mass scale, C_g, the intrinsic SUSY breaking to messenger scale, and again $\tan\beta$ and the sign of μ.

3

THE ATLAS EXPERIMENT AT THE LHC

3.1 The Large Hadron Collider

The Large Hadron Collider (LHC) [65] is a proton-proton and heavy-ion collider, located at CERN, near Geneva (Switzerland), that occupy a circular underground tunnel with a circumference of about 27 km. Till 2000 the tunnel housed the Large Electron-Positron collider (LEP). The LHC is constructed and presently under commissioning and the first collisions are expected to be observed in September 2008. The centre-of-mass energy of the pp interaction is designed to be 14 TeV and the luminosity is expected to reach 10^{34} cm^{-2} s^{-1}.

The choice for proton-proton collisions is due to both technical and economical reasons. An e^+e^- circular accelerator was excluded; indeed, a charged particle running along a circular trajectory loses energy through synchrotron radiation

$$\frac{dE}{dt} \propto \frac{E^4}{m^4 R}, \tag{3.1}$$

implying that, for fixed energy and radius, electrons will lose $(m_p/m_e)^4 \sim 10^{12}$ times the energy lost by protons. With this rate of energy loss an electron beam with the same energy reached at LHC could not keep its orbit. To avoid this problem, either a new tunnel with greater radius or a linear collider would be needed. Both these solutions would have been too expensive in time and money.

Also a $p\bar{p}$ collider was not compatible with the luminosity to be achieved at the

LHC. The number of anti-protons to be produced, grouped into bunches and then accelerated would have been prohibitively small.

The LHC project will allow a broad and ambitious physics programme, ranging from the precision measurements of the properties of known objects to the exploration of the high energy frontiers. The primary goal is to probe the origin of the electroweak symmetry breaking, focusing on the search for the Higgs boson, in particular, but also for new phenomena extending the Standard Model. The purpose of the LHC experiments is also to test the validity of the Standard Model with precision measurements, for instance the W and top quark masses and couplings, and to investigate the CP violation and the quark flavour mixing by the study of the B-hadron system. The LHC can also be used to collide heavy ions such as lead (Pb) with centre-of-mass energy of 1.15 TeV. Heavy-ion collisions will allow the search for a phase of matter in which quarks are deconfined from the hadron volume and dissolved into a fluid of quarks and gluons, as predicted by lattice QCD. Such a state, if it exists, would be called quark-gluon plasma.

The bunches of protons or heavy ions circulating in opposite directions will intersect at four points where the experiments are placed. Two detectors, ATLAS and CMS, are dedicated to new physics signatures and precision measurements, LHCb is designed to study the B-physics and ALICE is a heavy-ion experiment.

3.2 Detector overview

The ATLAS (A Toroidal LHC ApparatuS) detector [66, 67, 68] is an apparatus with cylindrical symmetry, with longitudinal axis coinciding with the beam direction, conventionally referred to as z. The xy-plane is the plane transverse to the z-axis and passing through the nominal pp interaction point, which act as the origin of the frame of reference. The x-axis positive direction is defined as pointing from the origin to the centre of the LHC ring and the positive y-axis as pointing upwards. To complete the coordinate nomenclature, the azimuthal angle ϕ is measured in the xy-plane with respect to x-axis and ϑ is the polar angle defined from the z-axis. The ϑ coordinate can be replaced by the pseudorapidity, defined as $\eta = -\ln\tan(\vartheta/2)$. The pseudorapidity is preferred over the polar angle because the number of particles produced at hadron

colliders per unit of pseudorapidity is approximately constant.

The main requirements for the detector are determined either by the mentioned physics programme and by the extremely challenging experimental conditions. Indeed, during pp operations, the total inelastic cross-section is about 80 mb, producing 10^9 events per second at the design luminosity. The large majority of these events are due to long distance collision between the two incoming protons, in which the produced particles have small transverse momentum, $\langle p_T \rangle \sim 500$ MeV, and have little physics interest. Since the beam bunches cross every 25 ns, when an interesting high-p_T event takes place, it is overlapped with about 25 inelastic events, constituting the pile-up. Moreover, the high-p_T event cross-section is dominated by jet production in QCD events, as shown in Figure 3.1 [69]. Thus the identification of rare process signatures demands great particle-identification capabilities for the detector.

The main set of general detector requirements is summarized as follows.

- A fast detector response and high granularity are required to minimize the signal contamination from overlapping events. The response time is different for the various subdetectors and represents the best compromise between technological limits and detector features. The high detectors granularity imply a large number of readout channels with a challenging acquisition, calibration and monitoring system.

- The radiation flux coming from the pp collisions, depends on the subdetector position with respect to the interaction point. In the forward region, for instance, the integrated flux of particle over ten years of operation in the high luminosity conditions will amounts up to $\sim 10^{17}$ neutrons/cm^2 and $\sim 10^7$ Gy. Due to this huge particle flux all the subdetector components should pass severe radiation hardness criteria.

- The trigger is a critical issue for the LHC experiments. The interaction rate of 10^9 events/s must be reduced to about 200 recorded events/s due to the storage system limits and therefore a very efficient and selective trigger is needed.

- The almost fully hermetic coverage allows a large acceptance for rare physics signals and the possibility to measure the missing transverse energy (E_T^{miss}) due to the passage of neutral weakly interacting particles escaping detection. Indeed,

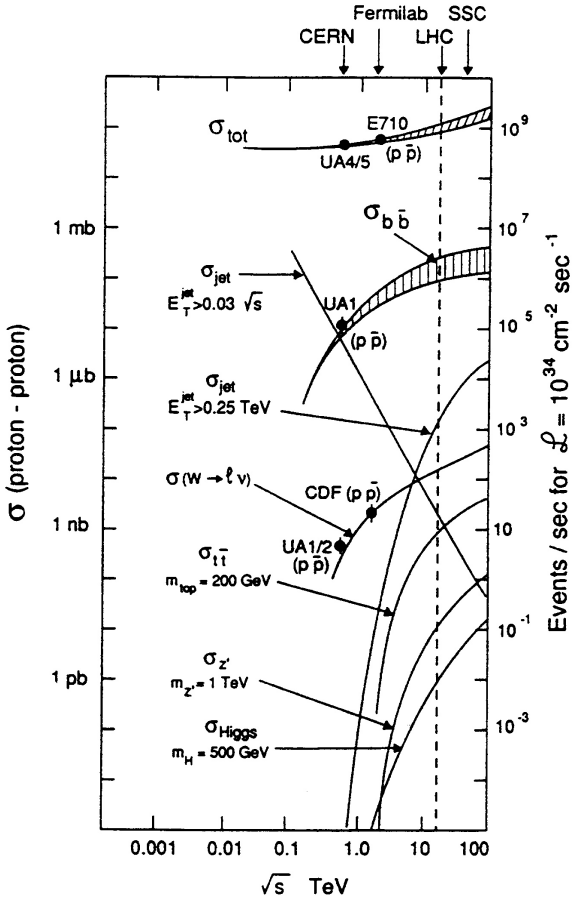

Figure 3.1: Proton-proton inelastic cross-sections as a function of the centre-of-mass energy [69].

even though at hadron colliders the longitudinal momenta of the interacting constituents of the incoming protons are unknown, the total transverse energy is, in first approximation, zero and the E_T^{miss} can be measured.

- An excellent energy and momentum resolution is needed for photons, electrons and muons. They should be measured over a p_T range from a few GeV up to a few TeV.

- Excellent performances on the identification of photons, electrons, muons, τ-jets and b-jets are required.

The overall detector layout is shown in Figure 3.2.

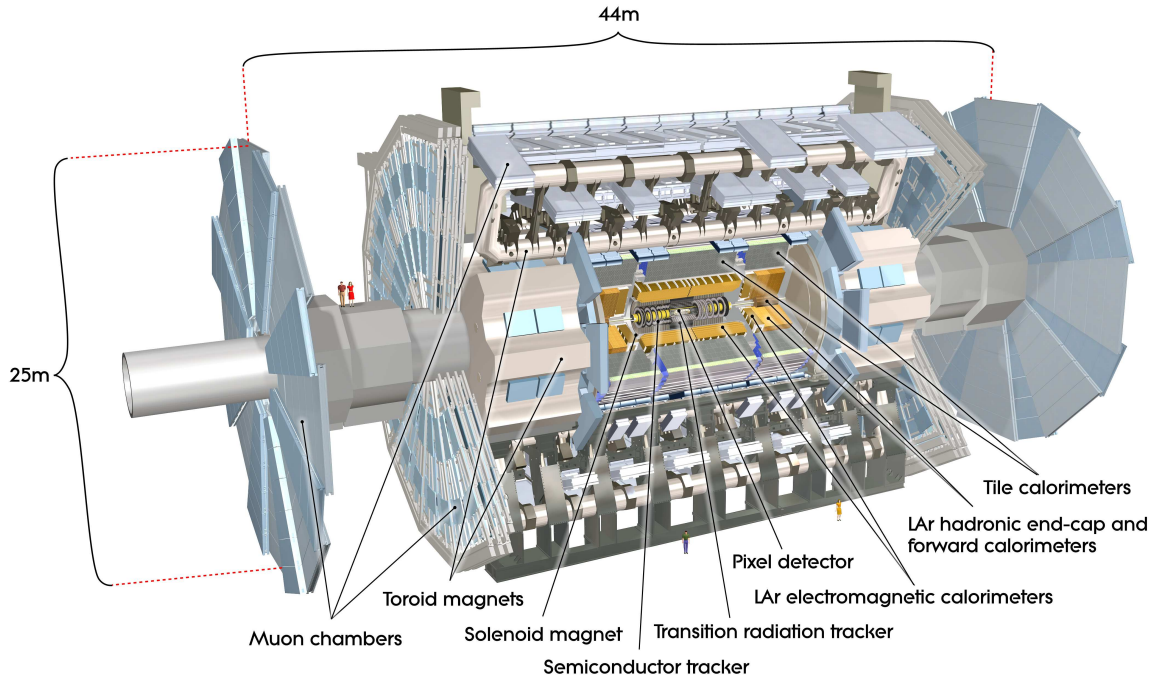

Figure 3.2: Cut-away view of the ATLAS detector.

Like all multi-purpose detectors, ATLAS comprehends many subdetectors with different capabilities. Close to the interaction point is the inner detector, a tracking system immersed into a 2 T solenoidal magnetic field, which allows to measure the momentum of charged particles and to reconstruct primary and secondary vertices. Moving toward the outside of the detector, we encounter the calorimeters, subdivided in electromagnetic and hadronic calorimeter. The electromagnetic calorimeter is the innermost one and its main task is to reconstruct the energy of photons and electrons. The energy of jets of hadronic particles mostly rely on the hadronic calorimeter, optimized to measure strongly interacting particles. Finally, an air-core toroid system surrounding the calorimeters provides the required magnetic field necessary to deflect muons which muon chambers can identify and measure.

The following sections review the different ATLAS subdetectors and systems.

3.3 Inner tracking system

Given the very large track density expected at the LHC, high-precision measurements of momenta and vertices need fine-granularity detectors. Due to the high cost of precision layers, the ATLAS inner detector [70, 71] combines high-resolution systems around the interaction point region with gaseous tracking elements at outer radii, all immersed in a 2 T magnetic field parallel to the beam axis. Figure 3.3 shows a cut-away view of the inner tracking system.

The precision layers are semiconductor tracking detectors, using silicon pixel and microstrip (SCT) technologies, covering the pseudorapidity region of $|\eta| < 2.5$. In the central region, they are arranged on concentric cylinders around the z-axis, while two end-cap regions are located on disks perpendicular to the beam direction. The highest granularity is provided by the silicon pixel layers, which are the closest to the interaction point. In particular, the first layer is placed at a radius of about 5 cm from the beams. Each track typically crosses three layers, with intrinsic accuracies of 10 μm in the $R-\phi$ plane and of 115 μm in the z (R) coordinate in the barrel (end-caps). The SCT layers are composed by small angle (40 mrad) stereo strips, parallel to the beam direction, to measure both coordinates. Eight layers are crossed by each track. They provide an intrinsic accuracy of 17 μm in the $R-\phi$ plane and 580 μm z (R) coordinate in the barrel (end-caps).

A larger number of tracking points will be provided by the transition radiation tracker (TRT). It is composed of 4 mm diameter straw tube detectors, achieving typically 36 points per track with much less material and a lower cost with respect to the precision layers. It covers the pseudorapidity range up to $|\eta| = 2$, with an intrinsic accuracy of 130 μm per straw in the $R-\phi$ coordinates. Electron identification capability is enhanced by employing xenon gas to detect transition-radiation photons created between the straws.

The combination of semiconductor layers with the TRT results in very robust pattern recognition and high precision in both ϕ and z coordinates. The semiconductor trackers also allow the reconstruction of the primary vertex of the pp interaction, as well as the measurement of track impact parameters and secondary vertices, useful for tagging jets arising from b-flavoured hadrons.

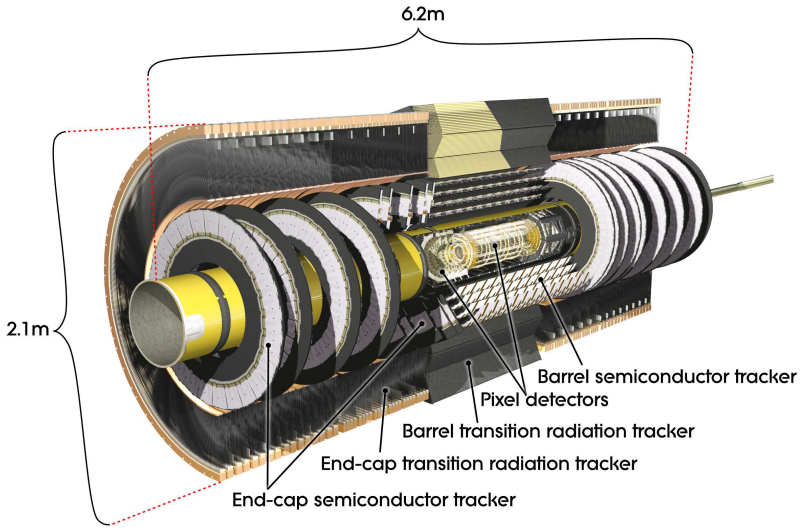

Figure 3.3: Cut-away view of the ATLAS inner tracking detector.

3.4 Calorimetry

The ATLAS calorimetric system [72] is represented in Figure 3.4 and consists of electromagnetic and hadronic calorimeters. Liquid-argon (LAr) electromagnetic sampling calorimeters cover the region $|\eta| < 3.2$. The hadronic calorimetry in the pseudorapidity range $|\eta| < 1.7$ is provided by scintillator-tile hadronic calorimeters, while in the end-cap regions ($1.5 < |\eta| < 3.2$) the liquid-argon technology has been chosen. In the forward regions, LAr calorimeters are used for both electromagnetic and hadronic energy measurements, extending the pseudorapidity coverage to $|\eta| = 4.9$.

3.4.1 Electromagnetic calorimetry

The electromagnetic (EM) calorimeter is a LAr detector with accordion-shaped kapton electrodes and lead absorber plates over its full coverage. Thanks to the accordion geometry a complete ϕ coverage can be achieved, without azimuthal cracks. The barrel part covers the $|\eta| < 1.475$ region and two end-caps complete the coverage up to $|\eta| < 3.2$. Each component is housed in its own cryostat. In order to reduce the upstream material, the central solenoid and the LAr calorimeter share a common vacuum vessel, thus eliminating two vacuum walls.

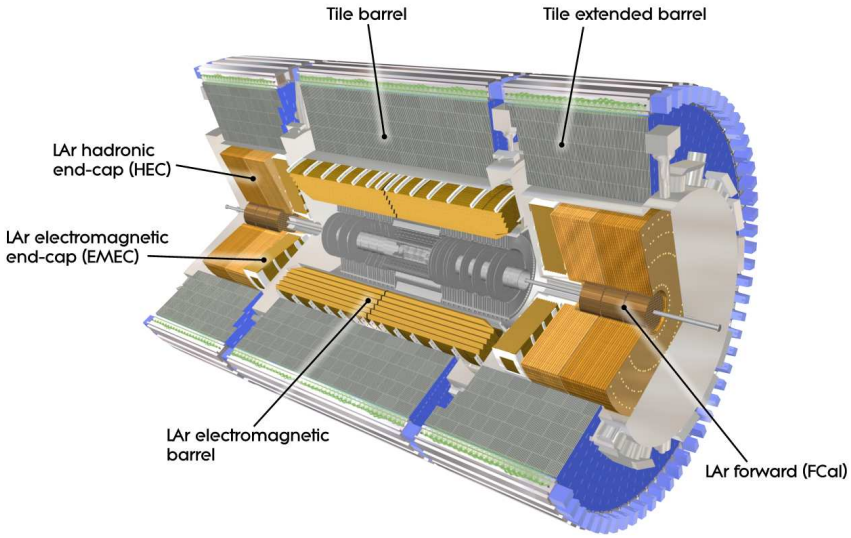

Figure 3.4: Cut-away view of the ATLAS calorimeter system.

The pseudorapidity region $|\eta| < 2.5$ is devoted to precision physics. Indeed, over this region the granularity is finer and the EM calorimeter is segmented into three longitudinal sections: the strips, the middle and the back section, while for $|\eta| > 2.5$ the granularity is coarser with only two longitudinal sections. The coverage, granularity and longitudinal segmentation of each calorimeter section is reported in Table 3.1.

Furthermore, over the pseudorapidity range $|\eta| < 1.8$, a presampler detector is installed before the calorimeter front face and is used to correct for the energy lost by electrons and photons in the material upstream the calorimeter.

The total thickness of the EM calorimeter varies with η, being > 22 radiation lengths (X_0) in the barrel and > 24 X_0 in the end-caps.

3.4.2 Hadronic calorimetry

The hadronic calorimeter consist of three barrel parts (one central and two identical extended barrels) covering $|\eta| < 1.7$ and two end-cap parts in the $1.5 < |\eta| < 3.2$ region. The total interaction length of active calorimeter is approximately 9.7λ in the barrel and 10λ in the end-caps, providing good shower containment for energy measurement as well as for limiting hadronic punch-through into the muon system.

EM Calorimeter	**Barrel**	**End-caps**	
Coverage	$\|\eta\| < 1.475$	$1.375 < \|\eta\| < 3.2$	
Granularity ($\Delta\eta \times \Delta\phi$)			
Strips	0.003×0.1	0.025×0.1	$1.375 < \|\eta\| < 1.5$
		0.003×0.1	$1.5 < \|\eta\| < 1.8$
		0.004×0.1	$1.8 < \|\eta\| < 2.0$
		0.006×0.1	$2.0 < \|\eta\| < 2.5$
		0.1×0.1	$2.5 < \|\eta\| < 3.2$
Middle	0.025×0.025	0.025×0.025	$1.375 < \|\eta\| < 2.5$
		0.1×0.1	$2.5 < \|\eta\| < 3.2$
Back	0.05×0.025	0.05×0.025	$1.375 < \|\eta\| < 2.5$

Table 3.1: Electromagnetic calorimeter coverage, granularity and longitudinal segmentation.

The barrels are based on a sampling technique with plastic scintillator plates (tiles) embedded in a steel absorber. Two sides of the scintillating tiles are read out by wavelength shifting fibres into two separate photomultiplier tubes. The detector is longitudinally segmented in three layers.

At larger pseudorapidities, where higher radiation resistance is needed, a LAr calorimeter is used, with copper absorbers and parallel plate geometry. It is located behind the electromagnetic end-cap calorimeters and shares the same LAr cryostats. The hadronic end-cap calorimeters (HEC) extend from $|\eta| = 1.5$ to $|\eta| = 3.2$, hence overlapping with both the tile and the forward calorimeters, and are divided into four longitudinal segments.

3.4.3 Forward calorimetry

The forward calorimeter (FCal) is integrated into the end-cap cryostats. This reduces the drop of material density at the transition between the end-cap and the forward region, thus providing a better calorimeter coverage and in addition diminishing the level of radiation in the muon spectrometer.

Moreover, in order to reduce the neutron reflection into the inner detector system,

the forward calorimeter front faces are shifted about 1.2 m farther away from the interaction point, with respect to the end-cap front faces. This limits the available longitudinal space and, thus, requires high-density design.

The forward calorimeter consists of three modules at each side of the ATLAS detector. Each module is composed of rod-shaped electrodes in a metal matrix filled with LAr as active material. The first module, intended to suit for electromagnetic measurements, is made of copper, while the other two are made in tungsten and measure predominantly hadronic energy deposits. The approximative total thickness is about 10 interaction lengths.

3.5 Muon spectrometer

The muon spectrometer [73] is based on the magnetic deflection of muon tracks in the large superconducting air-core toroid magnets, instrumented with separate high-precision and trigger tracking chambers. Its layout is shown in Figure 3.5.

The magnetic bending is provided by a large barrel toroid and by two smaller end-cap magnets inserted into both ends of the barrel toroid. The resulting magnetic field lines are circular and rolled around all the calorimeters. This configuration provides a field that is mostly orthogonal to the muon trajectories. The air-core structure minimizes multiple-scattering effects.

The four different type of chambers are used, based on the following technologies.

- The Monitored Drift Tubes (MDT's) are composed of several layers of aluminium drift tubes with a 50 μm diameter central wire.

- The Cathode Strip Chambers (CSC's) are multiwire proportional chambers with cathode strip readout in which the anode-cathode spacing is equal to the anode wire pitch.

- The Resistive Plate Chambers (RPC's) are gaseous avalanche detectors with no wires. The basic unit is a narrow gas gap formed by two parallel resistive plates, separated by insulating spacers.

- The Thin Gap Chambers (TGC's) are similar to multiwire proportional chambers

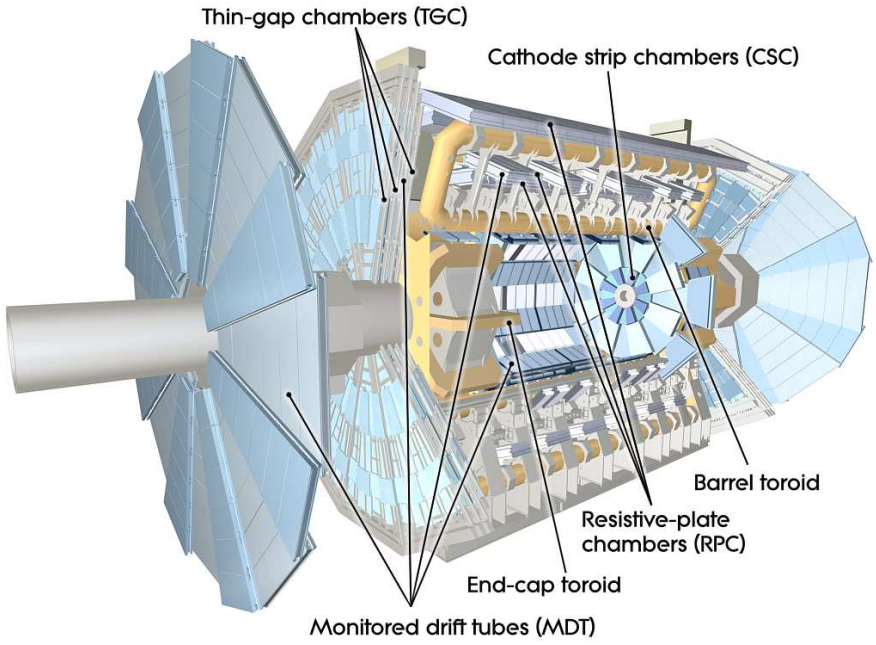

Figure 3.5: Cut-away view of the ATLAS muon system.

with the difference that the anode wire pitch is larger than the cathode-anode distance.

In the barrel region, tracks are measured in chambers arranged in three cylindrical layers around the beam axis, while in the end-cap region, the chambers are installed vertically. Over most of the η-range, the precision measurement of track coordinates are provided by MDT's. At large pseudorapidity CSC's with higher granularity are used in the innermost plane over $2 < |\eta| < 2.7$, to withstand the demanding rate and background conditions. Optical alignment systems have been designed to meet the stringent requirements on the accuracy on the relative position of the chambers.

Since electron drift times in MDT's and CSC's are large, respectively 700 ns and 30 ns, the capability to trigger on muon tracks is supplied by fast chambers capable of delivering signals with a spread of 15-25 ns. The RPC's, with time resolution of 1.5 ns, are used in the pseudorapidity range $|\eta| < 1.05$, while the TGC's complete the coverage up to $|\eta| < 2.4$ and have a time resolution of 4 ns. Thanks to their fast response, both chamber types provide the ability to tag the beam-crossing. In addition to their trigger function, these chambers also measure the muon coordinate orthogonal

to that determined by the precision-tracking chambers.

3.6 Trigger and Data Acquisition systems

The ATLAS trigger and data acquisition system (TDAQ) is based on three levels of event selection. Each trigger level refines the decision made at previous level applying additional selection criteria in order to progressively reduce the amount of data: starting from an interaction rate of 10^9 events/s at design luminosity, the rate of selected events is reduced to ~ 200 events/s for permanent storage. A simplified block diagram of the ATLAS TDAQ system is reported in Figure 3.6.

The first level trigger (L1) [74] makes an initial selection based on reduced granularity information from the calorimeters and on the trigger chambers of the muon spectrometer, looking for high-p_T particles and jets as well as large total and missing energy. Different thresholds combinations can be set for different signature selection. The L1 trigger is able to reduce the event rate to 100 kHz with a latency time of ~ 2 μs. During this latency time the information from all detectors channels are conserved in pipeline memories. For each event, the L1 trigger also defines the Region-of-Interests (RoI's), i.e. detector regions where interesting objects have been identified.

The second level trigger (L2) [75] refines the available information in the selected RoI's using more detailed detectors data, such as the full granularity and segmentation of the calorimeters. The L2 trigger reduces the rate to ~ 3.5 kHz with a latency time variable from 1 to 10 ms.

The third level is referred to as event filter (EF) [75] and is the last stage of selection. It will employ offline algorithms and it will use the most up to date calibration, alignment information and magnetic field map. The event rate after the event filter is ~ 200 Hz with an output size of approximately 1.3 MBytes/event to be written to mass storage for subsequent full offline analysis.

3.7 Computational aspects

Despite the 10^7 event rejection factor provided by the trigger system, the data volume expected in ATLAS amounts to about 10 PBytes per year. To match the required level

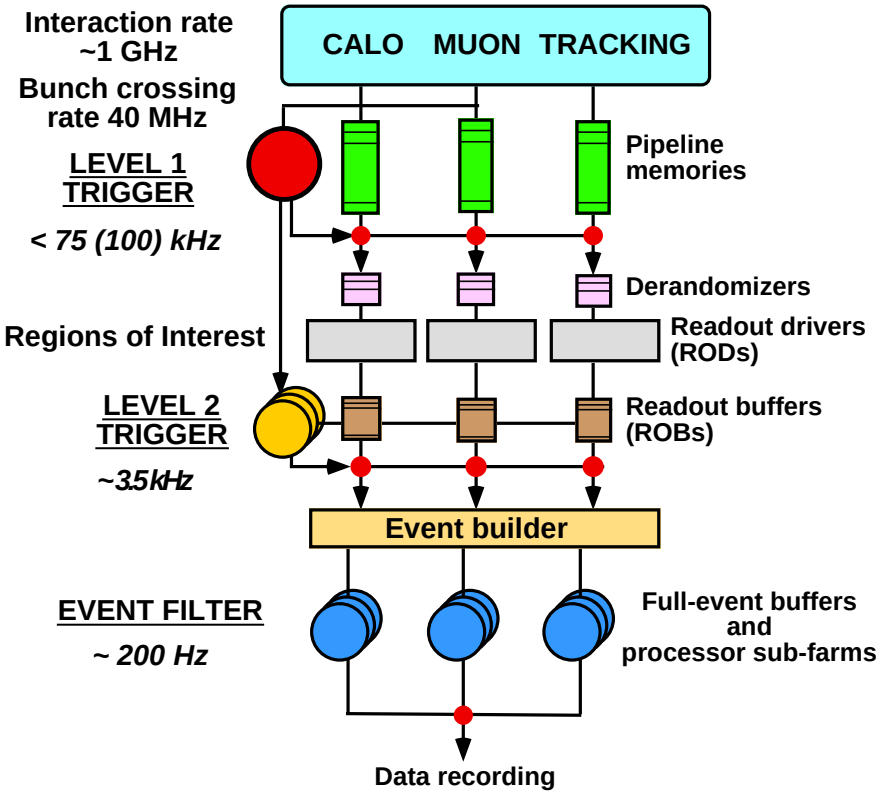

Figure 3.6: Block diagram of the ATLAS Trigger and data acquisition system.

of storage, computing power and data accessibility for physics analysis, the ATLAS computing model embraces the Grid paradigm with a high degree of decentralization and sharing of resources [76].

The data output from the event filter (RAW data) are copied and archived in a *Tier-0* facility at CERN. Here also a first event processing occurs within 48 hours after the data taking. The processing outputs, together with the RAW data, are distributed to the *Tier-1* facilities around the world. These facilities provide reprocessing capacity as well as data access for analysis by the physics groups. Output data derived from physics group analyses are copied to the *Tier-2* facilities for further analysis. *Tier-1* and *Tier-2* centres also provide the capacity to produce and store simulated data for the experiment.

In this context, the software is important to the whole experiment success and it must be maintained for the lifetime of about 20 years of the project. ATLAS has

adopted an object-oriented approach to software, based primarily on the `C++` programming language. All levels of processing of ATLAS data take place within the `Athena` framework. These comprise the event simulation and the treatment of real data. The simulation data flow is separated in three main steps:

- the generation of physics processes, i.e. the production of particles at the pp interaction, the decay of unstable particles, the radiation of initial and final states and the hadronization of eventual coloured final states; for this purpose a variety of external Monte-Carlo generators are interfaced with `Athena`;
- the simulation of the propagation and the interaction of the produced particles in the different ATLAS detector materials; this step is based on the `Geant 4` software [77, 78];
- the digitization of the fully simulated events, where the `Geant 4` output is translated into the output actually produced by the ATLAS detector subsystems.

Then, the produced samples pass through the same chain as real data:

- the L2 and event-filter trigger algorithm processing;
- the transformation of the detector output to physics objects (offline reconstruction);
- the physics analysis.

For physics studies requiring large statistics samples, a fast simulation of the ATLAS detector can also be used instead of the accurate but very CPU-consuming full-simulation sequence. In this case, the `Geant 4`, the digitization, the trigger and the offline reconstruction steps are skipped and the reconstructed physics objects are obtained by smearing the generated particle four-momenta, using a parametrization of the full-simulation ATLAS performances.

4

EXPECTED ATLAS PERFORMANCE

4.1 Particle reconstruction

The final state particles produced in a single event are reconstructed by combining the information coming from all output signals of the different subsystems of the ATLAS detector.

In the present section, we review the ATLAS performances in measuring and identifying photons, electrons, muons, jets, τ-jets, b-jets and missing transverse energy. The results are based on full simulation studies, considering both the most up-to-date ATLAS geometry and an experimental set-up with position shifts and material distortions, as expected for the real detector [68].

4.1.1 Photons and electrons

The ambitious physics program and the challenging background conditions at the LHC place severe requirements on the electromagnetic calorimeter performance in terms of photon and electron identification capabilities as well as energy and angular resolution. Indeed, the enormous cross-section of QCD processes is expected to overwhelm the inclusive production of photons and electrons. For instance, the electron-to-jet ratio is expected to be $\sim 10^{-5}$ at transverse momenta of 40 GeV. In addition, the material in front of the calorimeter causes substantial energy losses by electrons and high probability of photon conversions into pairs of electrons and positrons.

The reconstruction of electrons and photons starts with the clustering of electro-

magnetic energy deposits in the LAr calorimeter. A window with fixed dimension 1.25×1.25 in $\Delta\eta \times \Delta\phi$, equivalent to 5×5 cells of the calorimeter middle layer, is slided over all the calorimeter. Windows with total transverse energy above 3 GeV are kept as seeds. A cluster is built around the seed centre, with fixed dimension in $\Delta\eta \times \Delta\phi$ and comprising the three LAr layers and the presampler. For unconverted photons impinging on the barrel region, the choice of the cluster size of 3×5 cells is a compromise between shower containment and minimization of the contributions from electronic noise and pile-up. Instead, the energy of photons with a recognized conversion pattern and electrons is measured in a 3×7 cluster, since the electron-positron pair or the eventual photon-electron pair from hard bremsstrahlung are separated by the inner detector magnetic field. In the end-caps, where the cell size along ϑ is smaller than in the barrel, a window of 5×5 is chosen for both photons and electrons.

The method used for the energy calibration is based on the assumption that the energy lost by an incoming particle in the material in front of the calorimeter and the longitudinal leakage can be recovered by properly weighting the presampler and back compartment energy. In this hypothesis the corrected energy can be written as a weighted sum of the energies in the different longitudinal compartments:

$$E = s(\eta)\left[c(\eta) + w_0(\eta)E_{\mathrm{PS}} + E_{\mathrm{strips}} + E_{\mathrm{middle}} + w_3(\eta)E_{\mathrm{back}}\right]. \tag{4.1}$$

The η-dependent weights, s, c, w_0 and w_3, are determined separately for photons and electrons by minimizing the energy resolution, using full-simulated single particles, with energies ranging from 5 to 200 GeV. The relative energy resolution as a function of energy is shown in Figure 4.1 for electrons and photons at $\eta = 0.3$, 1.1, 2.0 and it can be expressed as

$$\frac{\sigma_E}{E} = a\sqrt{\frac{\mathrm{GeV}}{E}} \oplus b\frac{\mathrm{GeV}}{E} \oplus c. \tag{4.2}$$

The stochastic term, a, is between 10% and 12% for photons and between 10% and 15% for electrons, showing that the latter are more sensitive to the material in front of the calorimeter. The expected noise contribution is $b \sim 0.18$-0.23, while the constant term, c, reflects non-uniformities in the response of the calorimeter, due to, for example, temperature gradients and mechanical deformations of the detector. The goal for ATLAS is to achieve a constant term of 0.7% or smaller over the full acceptance. Electron test-beam results confirm these performances [79].

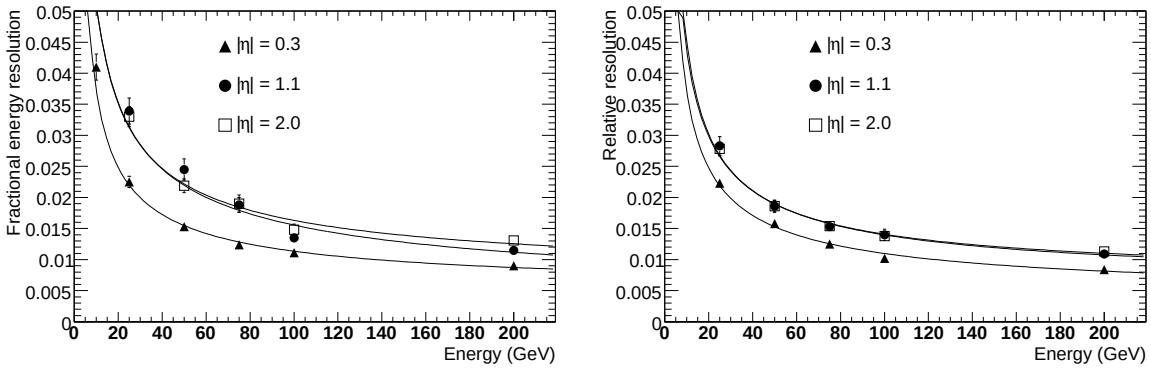

Figure 4.1: Relative energy resolution as a function of energy for electrons (left) and photons (right). The curves represent fits by the function in Equation 4.2.

Thanks to its fine granularity, the calorimeter also provides a measurement of the η and ϕ positions. The resolution in η for photons with an energy of 100 GeV is 2.5-3.5 $\times 10^{-4}$ in the strips and 5-6 $\times 10^{-4}$ in the middle layer, only slightly dependent on the calorimeter η region. The ϕ measurement is dominated by the middle layer, since the strips are coarser along this coordinate. The resulting resolution is expected to be about 1 mrad for photons with an energy of 100 GeV.

Photons and electrons can be discriminated from jets using selection cuts based on shower-shape variables, such as lateral and longitudinal profiles. Additionally, the information on tracks reconstructed in the inner detector is exploited to improve the separation power with respect to jets as well as to define unconverted photons, converted photons and electrons. As an example, the obtained identification efficiency for photons with transverse momentum above 25 GeV is 84% and the corresponding jet rejection is about 5000.

4.1.2 Muons

Muon tracks are reconstructed, identified and measured by the muon spectrometer alone or combined with the inner detector. Additional calorimeter information is used to improve the momentum resolution and the muon identification purity, especially rejecting non-isolated muons coming from the decay of heavy flavoured hadrons, i.e. hadrons containing c or b valence quarks.

Accurate muon identification and momentum measurement covers the energy spectrum from 3 GeV to 3 TeV, with a full acceptance over the region $|\eta| < 2.7$. Tracks reconstructed in the muon spectrometer are propagated back to the interaction point and are combined to inner-detector tracks. The pseudorapity region where combination is performed is limited by the geometrical acceptance of the inner detector ($|\eta| < 2.5$). The combination with the inner detector contributes to ameliorate the momentum resolution for tracks with momenta below 100 GeV. A correction for the energy lost in the calorimeters is estimated by a parametrized calculation or by the measured energy deposit.

Figure 4.2 shows the muon relative momentum resolution and the reconstruction efficiency. Stand-alone spectrometer performances are compared to results after the combination with the inner detector. In the right plot, for muons with $p_T \lesssim 10$ GeV, the efficiency loss is recovered by the extrapolation of inner-detector tracks to the muon spectrometer, where track segments are searched and merged to the seed track. Indeed, in this momentum range, muon tracks may not reach the middle and outer spectrometer stations, causing incomplete track reconstruction.

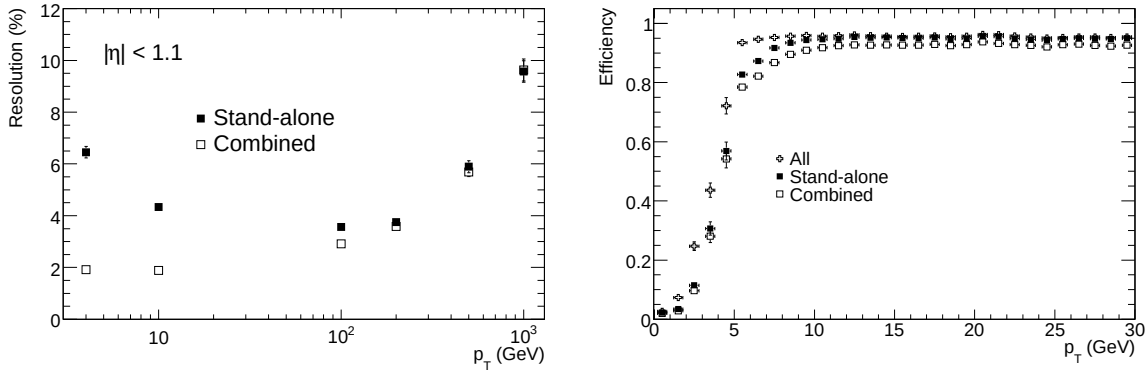

Figure 4.2: Relative momentum resolution (left) and reconstruction efficiency (right) with the muon spectrometer stand-alone (full squares) and after the combination of the inner detector (empty squares). The efficiency losses for $p_T \lesssim 10$ GeV is recovered by the addition of muons reconstructed starting from the inner detector and extrapolated to the muon spectrometer (full crosses), as explained in the text.

4.1.3 Jets

Jets of hadronic particles are reconstructed by applying a jet finding algorithm to calorimeter signals. In ATLAS, the two most commonly used jet finding algorithms are a fixed-size cone algorithm and a k_T algorithm [80]. The input calorimeter signals can be either towers or topological clusters. Towers are formed by collecting the energy of all cells in a geometrical region with size $\Delta\eta \times \Delta\phi = 0.1 \times 0.1$. The topological cluster algorithm, instead, reconstructs the three-dimensional energy deposit in the calorimeter, starting from an energetic seed cell and then adding neighbouring cells passing less severe energy thresholds. Since all the energy thresholds depend on the expected total noise in the cells, this clustering algorithm, in contrast with tower building, includes actual noise suppression.

The signals of all the calorimeter cells belonging to the jet are summed together, weighted by the w function, depending on the energy density $\rho = E/V$ and on the calorimeter module of the cell (identified by the cell position $\vec{X}$). An extra term, recovering for energy losses in the cryostat between the electromagnetic barrel and the tile calorimeter, is calculated for each jet in terms of the jet-energy deposited in the last compartment (E_{back}) of the LAr calorimeter and in the first layer of the tiles (E_{tile0}). The calibrated energy can then be expressed as

$$E = \sum_{i}^{\text{cells}} w(\rho_i, \vec{X}_i) E_i + \alpha \sqrt{E_{\text{back}} E_{\text{tile0}}}. \tag{4.3}$$

The w and α parameters are extracted by minimizing the relative energy resolution, using QCD di-jet events and comparing cone jets from tower signals to cone jets with the Monte-Carlo particles as input. The relative energy resolution for jets can be written in a form analogous to Equation 4.2, with a stochastic term a of about 60% in the central region of the detector.

4.1.4 Hadronic τ decays

The heaviest charged lepton, the τ-lepton, is an unstable particle with branching ratio to final states containing hadrons of about 65%. Hadronic τ decays, commonly called τ-jets, can be identified by the ATLAS detector. In general, they are characterized

by a collimated group of tracks, with total charge consistent to the τ-lepton charge, pointing to a narrow cluster of energy deposit.

In ATLAS, two complementary strategies have been studied. An algorithm starting from tracks reconstructed in the inner detector is optimized for τ's with visible transverse energies in the range between 10 and 80 GeV, while a calorimeter-based algorithm, which relies on clusters reconstructed in the calorimeter, is optimized for visible τ energies above 30 GeV. The expected rejection factor against jets from QCD events as a function of the efficiency of τ-jet reconstruction and identification is shown for both algorithms in Figure 4.3.

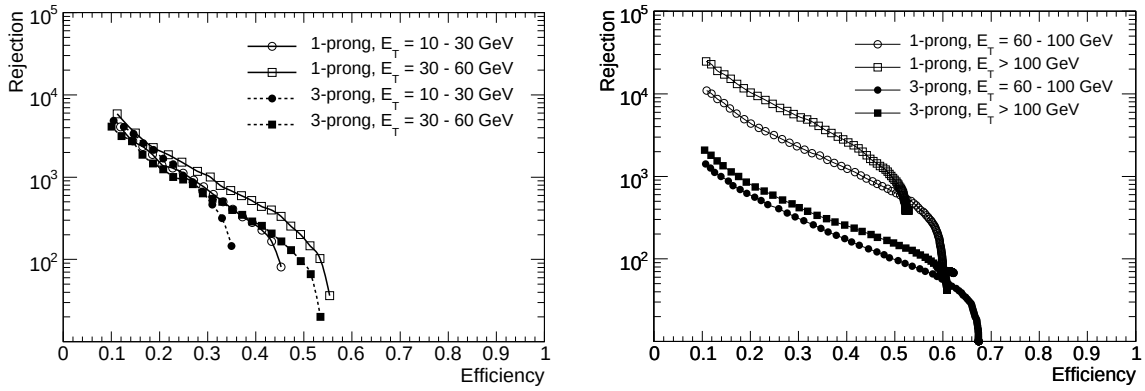

Figure 4.3: Expected rejection against jets from QCD events as a function of the efficiency of τ-jet reconstruction and identification. The left plot shows the performance of the track-based algorithm, while the right plot shows the performance of the calorimeter-based algorithm. The results are shown separately for decays into a single and three charged hadrons (prongs).

4.1.5 Tagging b-flavoured jets

Jets arising from b-quarks can be tagged by exploiting the fact that b-flavoured hadrons have a sufficient lifetime to travel between 0.5 mm to few centimetres before decaying, depending on their boost. Thus, the measurement of track impact parameters, calculated with respect to the reconstructed primary vertex, and the identification of secondary vertices are used to discriminate between b-jets, c-jets and jets initiated by

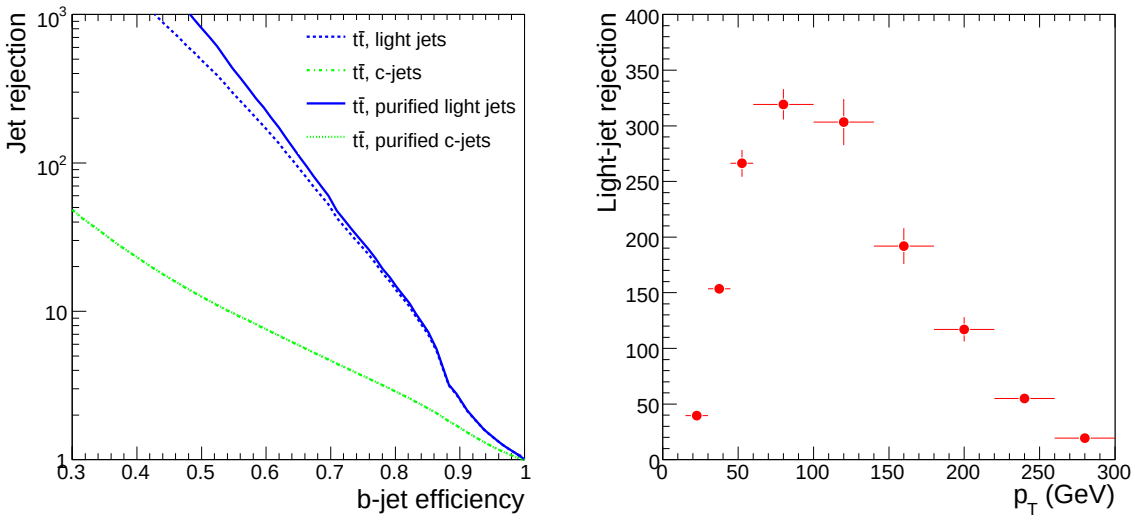

Figure 4.4: Left: rejection against light and c-jets as function of b-jet identification efficiency. Purified jet collections are obtained by asking that neither Monte-Carlo b-quarks nor Monte-Carlo τ-leptons are found inside a cone around the jet axis. Right: rejection against light jets for a fixed 60% efficiency as a function of the jet transverse momentum.

u-, d-, s-quarks and gluons (light jets).

Calorimeter jets are associated to inner-detector tracks and secondary vertices satisfying severe quality cuts, to reject fake tracks and secondary tracks from long-lived hadrons, such as K_s^0 and Λ, and photon conversions. For instance, tracks must have transverse momentum above 1 GeV and a hit in the first pixel layer.

For each track and secondary vertex, discriminating variables are compared to predefined normalized distribution for both b- and light jets and the probabilities for the two hypotheses are computed. The ratio of the probabilities defines the track or vertex weight, which are multiplied together to extract a jet weight. A selection cut on the jet weight defines the b-jet tagging.

The left plot in Figure 4.4 shows the rejection against light and c-jets as function of b-jet identification efficiency in $t\bar{t}$ events. For 60% efficiency, the light jet rejection is more than 100, while the c-jet rejection is around 10.

For a fixed efficiency, the rejection factor depends strongly on the jet p_T (Figure 4.4,

right) and η. At low transverse momenta and high pseudorapidities, the performance degrades mostly because of the increase of multiple scattering and secondary interactions. At high p_T, more B-hadrons decay outside the vertexing layer, causing a deficiency in track selection. Therefore, some gain should be achievable by adjusting the track quality cuts. However, at very high p_T, tracks in jets become very dense causing track-pattern reconstruction very difficult, thus deteriorating the rejection capability.

4.1.6 Missing transverse energy

At the LHC the two incoming partons have, in first approximation, transverse momenta equal to zero. Thus, an unbalanced total transverse momentum is the signal of the passage of particles escaping from the detector without interacting.

The missing transverse energy is a two-component vector of the xy-plane, calculated in ATLAS as the minus-signed vectorial sum of the energy deposits in the calorimeters and the measured muon momenta.

As first step of the reconstruction, a noise suppression algorithm is executed on the calorimeter cells and only the surviving ones are taken into account for the calculation of

$$\vec{E}_T^{\text{miss,Cal}} = -\sum_i^{\text{cells}} w(\rho_i, \vec{X}_i)\vec{E}_{T,i}. \tag{4.4}$$

The topological clustering (Section 4.1.3) is the most promising noise suppressor. The cell energy weights w are the same used to calibrate jets. The energy lost in the cryostat between the LAr electromagnetic barrel and the tile calorimeter, is computed for every jet in the event according to the last term of Equation 4.3. Thus the contribution to the missing transverse energy is

$$\vec{E}_T^{\text{miss,Cryo}} = -\sum_i^{\text{jets}} \left(\alpha\sqrt{E_{i,\text{back}}E_{i,\text{tile0}}}\right)\frac{\vec{E}_{T,\text{jet}}}{E_{\text{jet}}}. \tag{4.5}$$

The additional term $\vec{E}_T^{\text{miss,Muons}}$ is calculated from muons with a matched track in the inner detector to reduce fake muons, sometimes created from high hit multiplicities in the spectrometer in events with very energetic jets. The muon momenta are measured by the spectrometer alone, to avoid double counting of muon energy deposited in the

calorimeter. The final missing transverse energy is the sum of the three terms above:

$$\vec{E}_T^{\text{miss}} = \vec{E}_T^{\text{miss,Cal}} + \vec{E}_T^{\text{miss,Cryo}} + \vec{E}_T^{\text{miss,Muons}}. \tag{4.6}$$

In a final step, each calorimeter cell can be associated to a reconstructed particle in the event and recalibrated differently according to the nature of the parent object. Cells passing the noise suppression but which do not contribute to any reconstructed particle are kept in the calculation with the unmodified weight w.

Figure 4.5 shows the missing transverse energy performance, evaluated in simulation studies by comparing the reconstructed quantity to the transverse momentum brought by non-interacting Monte-Carlo particles. The linearity of the E_T^{miss} response (left), as function of the true value in $A \rightarrow \tau^+\tau^-$ events, evolves from 10%-30% before applying the cell weights w to less than 5% after the global and refined calibration steps. The E_T^{miss} resolution (right) is, in good approximation, proportional to the square root of the scalar sum of the transverse energies of the calorimeter cells. The fitted proportionality coefficient is found to be comprised between 0.53 and 0.57.

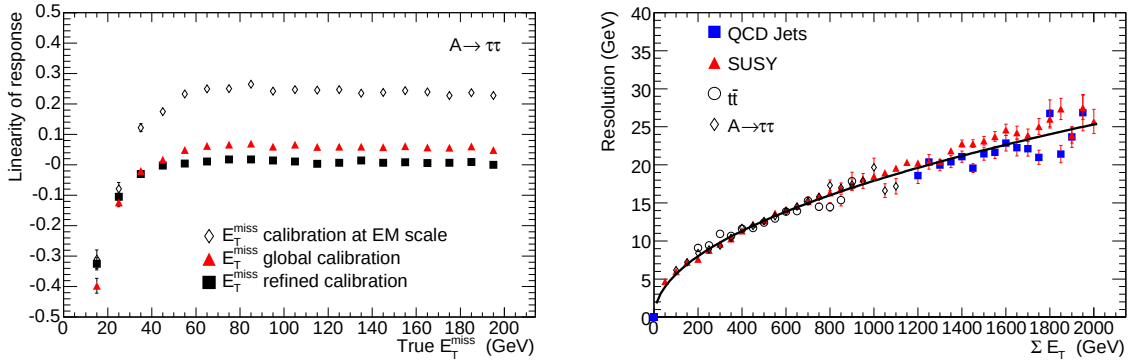

Figure 4.5: Linearity of the E_T^{miss} response as function of the true value in $A \rightarrow \tau^+\tau^-$ events (left) and E_T^{miss} resolution as function of the scalar sum of the transverse energies of the calorimeter cells in different simulated events (right).

4.2 Trigger performance

The trigger system should guarantee coverage of the full physics programme, ranging from Standard Model precision measurements to new physics searches, while retaining the required rejection power demanded by storage limitations. In addition, the trigger selection algorithms must fulfil high flexibility in order to adapt to changes in the luminosity and background conditions.

The trigger signatures are defined by the identification of high-p_T objects in the calorimeter or in the muon trigger chambers. Multiple object signatures are then obtained by combination of the different identified signals. Global variables, for instance missing transverse energy, complete the physics coverage.

A possible set of signatures with the respective momentum thresholds, in general called trigger menu, has been appositely studied for the LHC start-up conditions. Indeed, the initial luminosity is expected to be around 10^{31} cm^{-2}s^{-1}, allowing convenient conditions for commissioning of the trigger system and algorithms. As the LHC luminosity ramps up toward its design value, the trigger menu will evolve to a set of tighter criteria.

Table 4.1 displays an example of some possible trigger signatures to be used during stable data taking at luminosity 2×10^{33} cm^{-2}s^{-1}. The first level and high level (L2+EF) trigger menus are shown separately. Every trigger signature is labeled by a symbol representing the triggered object type, preceded by the number of objects that should be found and followed by the transverse momentum lower cut in GeV. It should be noticed that first level and high level particles have different symbols. An extra i (or I) is added if an isolation specification is required. The term xE (or XE) stands for missing transverse energy.

4.3 SM Higgs boson discovery potential

The experimental observation of the Higgs boson is, of course, a crucial topic of ATLAS searches. Many studies have been performed in order to ensure a good discovery potential over the allowed mass range of a SM Higgs boson, 100 GeV $\lesssim m_h \lesssim$ 1 TeV. The lower mass bound comes from loosen exclusion limit from direct searches at LEP (Section 1.4), while the upper bound is needed to preserve the unitarity of the

	L1	Rate (kHz)	L2+EF	Rate (Hz)
Electrons and photons	EM18I	12.0	e22i	40
	2EM11I	4.0	2e12i	< 1
			γ55i	25
			2γ17i	2
Muons	MU20	0.8	μ20i	40
	2MU6	0.2	2μ10	10
Jets and E_T^{miss}	J140	0.2	j370	10
	3J60	0.2	4j90	10
	4J40	0.2	j65+xE70	20
	J36+XE30	0.4		
τ-jets	TAU16I+XE30	2.0	τ35i+xE45	5

Table 4.1: An example of some possible trigger signatures to be used during stable data taking at luminosity 2×10^{33} cm^{-2}s^{-1}. The first level and high level (L2+EF) trigger menus are shown separately.

scattering matrix in vector boson elastic processes [81].

For a Higgs mass just above the present exclusion limit, three main decay modes are taken into consideration for ATLAS searches, $h \to b\bar{b}$, $h \to \gamma\gamma$ and $h \to \tau^+\tau^-$. The decay into a pair of b-quarks has the higher branching ratio since it is the heaviest particle pair kinematically accessible in this Higgs mass region. But, even though the decay in a pair of b-quarks has the highest branching ratio and the total production of Higgs decaying into this channel is large, about 20 pb, the signal to background ratio is less then 10^{-5} and the QCD $b\bar{b}$ processes overcome the Higgs signal. However, selecting only the events of Higgs produced in association with a vector boson or with two t-quarks significantly reduces the level of background, by virtue of final states with leptons, although it decreases the cross-section to about 1 pb. The $pp \to h \to \gamma\gamma$ cross-section is very small ($\simeq 50$ fb) but, because of its very clear signature, it is expected to be one of the most important channel in the low Higgs mass region This channel places severe requirements on the performance of the electromagnetic calorimeter. Indeed, excellent energy and angular resolution are needed to observe the narrow peak above

the $\gamma\gamma$ continuum background and powerful photon to jet separation capability is required to reject the large QCD background. More recent studies have been carried out on the Higgs production via fusion of weak vector bosons, followed by the decay to $\tau^+\tau^-$. In this events, the presence of two forward jets produced in association with the Higgs boson can be used to suppress the background.

For intermediate Higgs masses, $140 \lesssim m_h \lesssim 2m_Z$ the main discovery channels are expected to be $h \to ZZ^* \to 4\ell$ and $h \to WW^{(*)} \to \ell\nu_\ell\ell\nu_\ell$ ($\ell = e, \mu$). The first process gives rise to a very distinctive four lepton state. The main irreducible background consists of ZZ^* and $Z\gamma^*$ continuum production. For Higgs mass around 160 GeV, the branching ratio of $h \to ZZ^*$ is reduced because of the opening of the WW decay mode. For these values of m_h, the $H \to WW^{(*)} \to \ell\nu_\ell\ell\nu_\ell$ branching ratio is approximately a hundred times larger than that of the $h \to ZZ^* \to 4\ell$ channel. However, the presence of the two neutrinos make it impossible to reconstruct the Higgs boson mass peak but only an excess of events can be observed.

The case of an Higgs boson with mass between $2m_Z$ and ~ 700 GeV is the LHC best possible scenario. The gold-channel with two real Z bosons in the final state opens up. The signal events with both Z bosons decaying into a pair of electrons or muons are expected to be greater than the background, which is dominated by the continuum production of Z pairs. No severe requirements are necessary since the leptons momenta are high and also the intrinsic Higgs width dominates the experimental resolution for $m_h > 300$ GeV, as it grows rapidly with increasing m_h. For Higgs masses larger than about 700 GeV the $h \to ZZ \to 4\ell$ becomes rate-limited. The two main decay channel for Higgs around the TeV region are $h \to ZZ \to \ell\ell\nu_\ell\nu_\ell$, with a rate six times greater than the four leptons mode, and $h \to WW \to \ell\nu_\ell qq$, with a rate more than a hundred times greater than the four leptons mode.

The overall sensitivity for the discovery of a Standard Model Higgs boson over the discussed mass range is reported in Figure 4.6 for an integrated luminosity of 30 fb^{-1}, that is expected to be accumulated in a few years of running in the so-called low luminosity phase of the machine (10^{33} cm^{-2} s^{-1}). A 5σ significance should be reached. Moreover, an eventual discovery claim for a Standard Model Higgs would be quite robust, since more than a single channel can be observed over almost the full mass range.

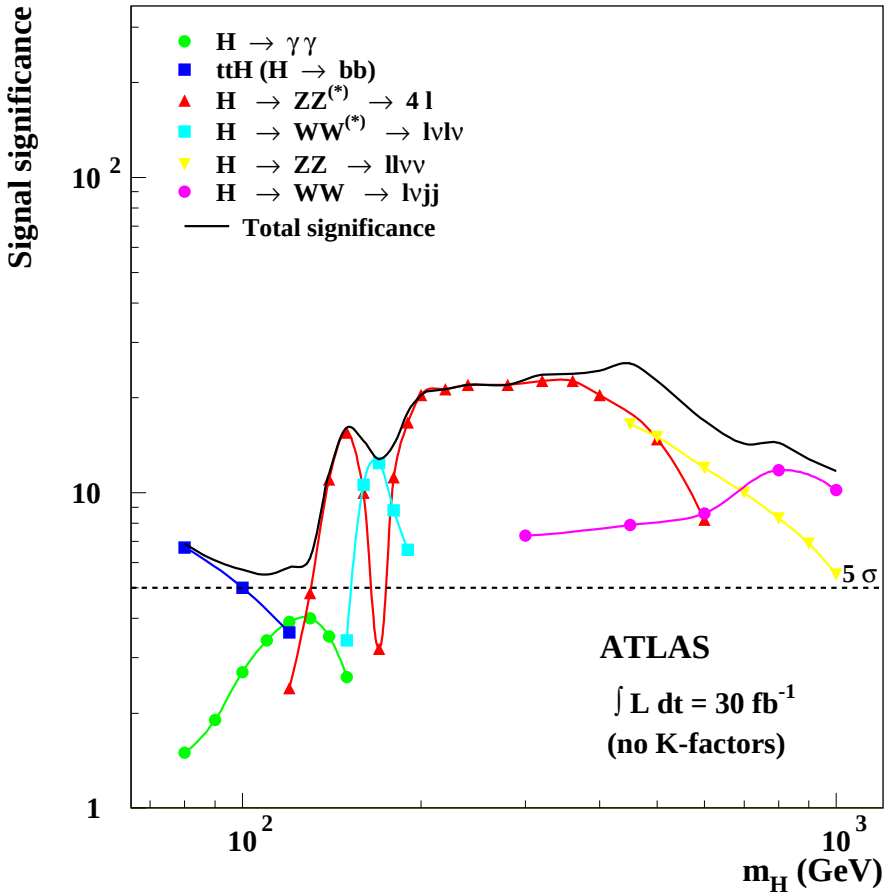

Figure 4.6: Expected signal significance for a Standard Model Higgs boson in ATLAS as a function of the Higgs mass and for an integrated luminosity of 30 fb^{-1} [67]. In the low mass region, the $h \to \tau^+\tau^-$ channel is not included; an equivalent plot for the region $m_h < 200$ GeV comprising this channel can be found in [82].

4.4 MSSM Higgs discovery potential

In the MSSM, the potential for the two Higgs doublets is completely defined by the gauge couplings between four Higgs fields and by the Higgs mass terms in the superpotential and in the soft supersymmetry breaking Lagrangian. For suitable values of the input parameters, the potential has a minimum for the values of the two electrically neutral Higgs components, $\langle H_u^0 \rangle = v_u$ and $\langle H_d^0 \rangle = v_d$, causing the $SU(2)_L$ symmetry breaking to occur.

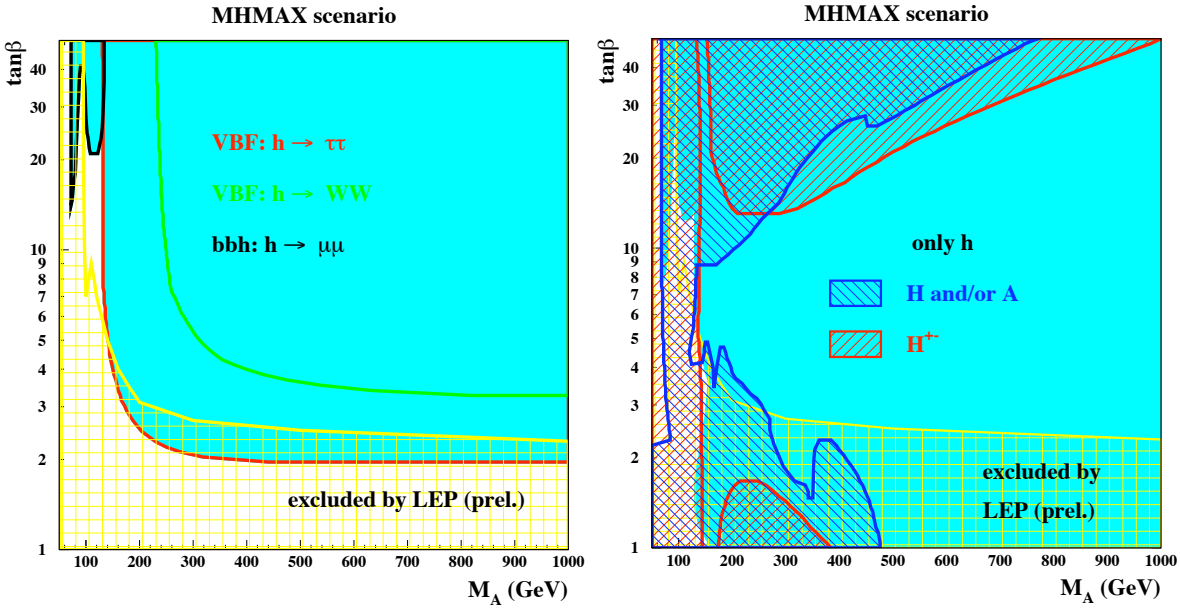

Figure 4.7: Left: lightest Higgs boson h discovery potential in the m_h-max scenario for 30 fb^{-1} of integrated luminosity. Right: overall discovery potential for Higgs bosons in the m_h-max scenario for 300 fb^{-1} of integrated luminosity.

At tree level, all masses and couplings of the MSSM Higgs sector can be expressed in terms only of the measured SM parameters and two additional ones. The latter are usually taken to be $\tan\beta = v_u/v_d$ and the mass of the CP-odd Higgs boson, m_A. The combination $v^2 = v_u^2 + v_d^2$ is fixed by weak interaction measurements. However, the Higgs sector receives large radiative corrections and additional SUSY parameters are needed to consider higher order effects. For example, the tree-level mass of the lightest Higgs, m_h, is constrained to be smaller than the Z boson mass, but after the inclusion of quantum corrections it can be as large as 140 GeV.

In the following, we present the so-called m_h-max scenario [83], in which the SUSY parameters are designed to yield the largest value of m_h for a given $(m_A, \tan\beta)$. Results for this and other three different scenarios are discussed in [84, 85]. Moreover, scenarios where CP-parity is not conserved in the Higgs sector are also possible. Their phenomenology and experimental signatures are studied in [86].

The discovery potential for the lightest Higgs boson h is shown in Figure 4.7 (left), after collecting 30 fb^{-1} of integrated luminosity. The Higgs produced via weak vector

boson fusion (VBF) and then decaying into a pair of τ-leptons provide the dominant discovery channel. The region at small m_A and large $\tan\beta$ is covered by the $h \to \mu^+\mu^-$ channel produced in association with two b-quarks. The observation of the VBF $h \to WW$ mode, when possible, should allow to measure the ratio of $BR(h \to \tau^+\tau^-)/BR(h \to WW)$, a variable with potential discriminating power between SM and MSSM Higgs boson. The observation of the $h \to \gamma\gamma$ and $h \to b\bar{b}$ decays has the same interest. Indeed, even though they are expected not to be competitive for early Higgs discovery, the measurement of the ratio of their branching fractions should be possible by studying both channels in the $t\bar{t}$-associated mode.

The discovery potential for the heavy neutral Higgs bosons H and A is given by associated production with b-quarks and the decay into a pair of muons and τ-leptons. Charged Higgs bosons can be observed from top quark decays for $m_{H^\pm} \lesssim 170$ GeV and from fusion of a gluon and a b-quark for $m_{H^\pm} \gtrsim 180$ GeV. Figure 4.7 (right) shows the overall discovery potential for the five Higgs bosons for 300 fb^{-1} of integrated luminosity. As it can be noticed, an area at intermediate values of $\tan\beta$ remains where only the light CP-even Higgs boson h can be observed.

4.5 SUSY discovery potential

Since supersymmetric particles have the same gauge couplings as Standard Model particles, strongly interacting squarks and gluinos are expected to be the most copiously produced SUSY particles at the LHC.

As explained in Section 2.4, if R-parity is conserved, each of the produced particles generates a decay chain ending with the lightest supersymmetric particle. In most SUSY models, the LSP is a neutral weakly interacting particle that passes through the detector without radiating or ionizing, but leaving a missing transverse energy signal. During the decay cascade, SM particles are also emitted. At the LHC, these are mainly the SM partners associated to squarks and gluinos. Thus, SUSY events contains hadronic jets, that in addition are very energetic since they come from massive states.

Starting from these characteristic features, inclusive search strategies have been developed to detect SUSY particle production with the ATLAS detector [87]. Detailed

studies are carried out for various signatures using fully simulated data sets for specific SUSY benchmark points and for the relevant SM backgrounds. The few sets of selection cuts derived from these investigations are then used to test the discovery potential over a larger range of models. For this purpose, the parameter spaces of some SUSY breaking model, such as Minimal SUGRA and GMSB, considered as representative of the MSSM phenomenology, are scanned with a fast simulation of the ATLAS detector.

The standard inclusive analyses are based on a four-jet signature, since a high jet multiplicity helps to reduce the background from QCD and weak boson production. The basic selections applied are:

1. Four jets with $p_T > 50$ GeV, including at least one with $p_T > 100$ GeV, and $E_T^{\rm miss} > 100$ GeV;
2. $E_T^{\rm miss} > 0.2 M_{\rm eff}$;
3. $S_T > 0.2$
4. $|\phi(E_T^{\rm miss}) - \phi({\rm jet})| > 0.2$, for each of the three jets with leading transverse momentum.

The introduced $M_{\rm eff}$ and S_T are respectively the effective mass and the transverse sphericity, two global event variables defined as

$$M_{\rm eff} = E_T^{\rm miss} + \sum_i^{\rm jets} p_{T,i} + \sum_i^{e,\mu} p_{T,i}, \tag{4.7}$$

$$S_T = \frac{2\lambda_2}{\lambda_1 + \lambda_2}, \tag{4.8}$$

where $\lambda_{1,2}$ are the eigenvalues of the 2×2 matrix $S^{ab} = \sum_i^{{\rm jets},e,\mu} p_{T,i}^a p_{T,i}^b$ (with a, b representing the geometrical x and y coordinates). In particular, the cut on the transverse sphericity aims to suppress QCD di-jet events in favour of spherical topologies with high particle multiplicity. For instance, an event with exactly two back-to-back particles in the ATLAS transverse plane has $S_T = 0$, while an event composed by four jets, all with identical p_T and separated by a right angle in ϕ, has $S_T = 2$.

An additional request on the number of identified leptons defines three different analyses, completely non overlapping: the 0-lepton, the 1-lepton and the 2-lepton mode.

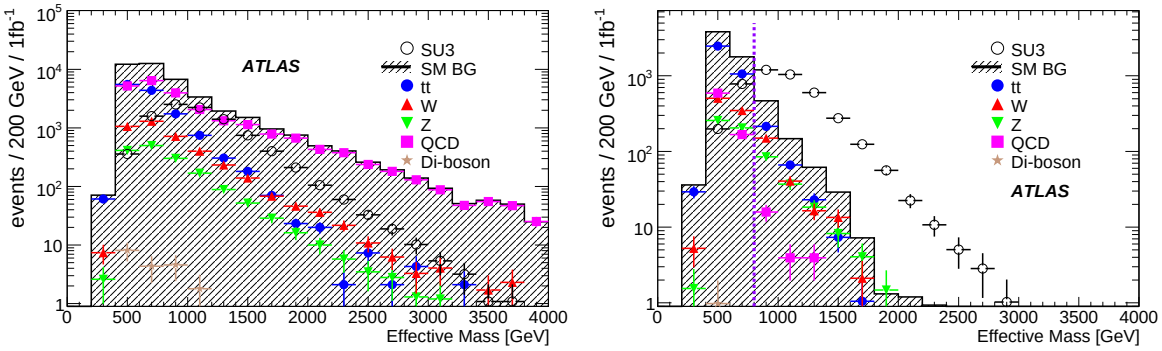

Figure 4.8: Effective mass distribution for the mSUGRA point SU3 and the Standard Model background after 1 fb^{-1} of integrated luminosity. For the left plot only cut 1 is applied, while for the right plot the complete selection of the 0-lepton mode is used.

This approach has been chosen to ease the future combination of the three channels. For the 2-lepton signature, the signal-to-background separation power is enhanced by demanding the two leptons to have opposite-sign electric charge and same flavour.

In addition to the four-jet channels, signatures with lower jet multiplicity are also addressed. These signatures have more backgrounds, but might be favoured in some SUSY models. This is the case of GMSB models, where a single-jet plus three-lepton analysis seems more promising.

Figure 4.8 shows the effective mass distribution for the mSUGRA benchmark point called SU3 ($M_0 = 100$ GeV, $M_{1/2} = 300$ GeV, $A = 300$ GeV, $\tan\beta = 6$, $\mu > 0$) and the SM backgrounds, as expected for 1 fb^{-1} of integrated luminosity and at different stages of the selection flow. The left plot is obtained by applying only cut 1, while for the right plot all listed selection cuts plus a 0-lepton request are used.

The discovery potential for mSUGRA and GMSB models is shown in Figure 4.9, after 1 fb^{-1} of collected luminosity. The mSUGRA scan is performed for fixed values of $A = 0$ GeV, $\tan\beta = 10$ and positive μ. The GMSB parameters are fixed at $N = 5$, $M = 500$ TeV, $C_g = 1$ and $\mu > 0$. Refer to Section 2.6 for the definition of mSUGRA and GMSB parameters.

The signal significance is evaluated by counting the signal and background events with effective mass greater than 800 GeV. The background uncertainty has two contri-

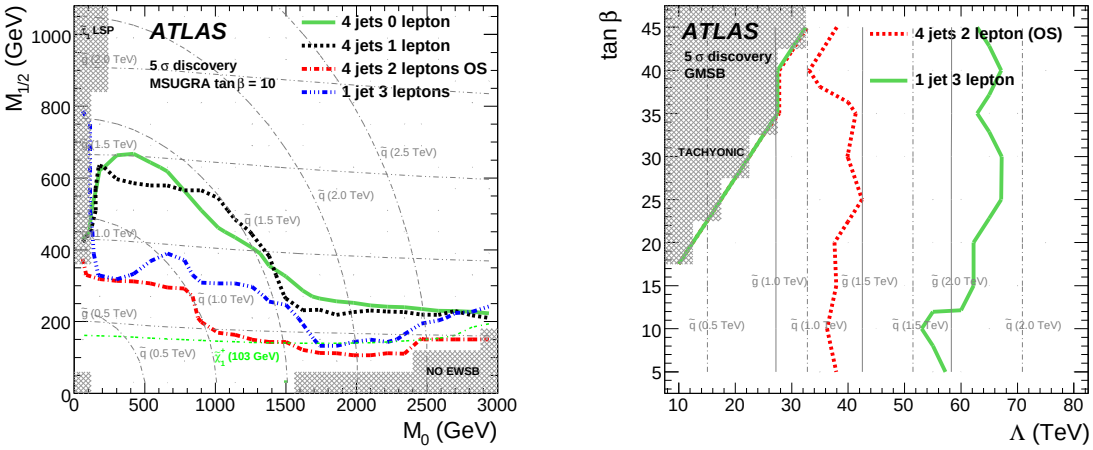

Figure 4.9: Discovery potential for mSUGRA and GMSB models for different analyses.

butions that are taken into account: one due to Poisson statistics and another Gaussian error corresponding to the systematic uncertainty on the SM rate prediction. The latter can be extracted with methods based on both Monte-Carlo simulations and real data. For a cumulated statistics of 1 fb^{-1}, they are estimated to be 50% for the QCD events and 20% for the $t\bar{t}$, W and Z events.

For mSUGRA, the 0-lepton and 1-lepton modes have comparable reach, covering the region with squark and gluino masses up to 1.5 TeV.

All the models considered in the GMSB case have abundant production of events with at least two leptons, so the signatures are easier to distinguish from Standard Model backgrounds. The reach for three leptons is significantly better than for two leptons and extends to gluino masses of more than 2 TeV.

5

MISSING TRANSVERSE ENERGY STUDIES AND MONITORING

5.1 Introduction

The missing transverse energy reconstruction plays an important role in SUSY searches, as explained in the previous chapter. In addition, a precise measurement of E_T^{miss} in terms of absolute scale and resolution is important for physics analyses where the mass of a particle decaying to neutrinos must be reconstructed. This is the case, for instance, of the measurement of the top quark mass in $t\bar{t}$ events where one top decays to leptons, but also for searches for a Higgs boson decaying into a pair of τ-leptons.

Another important requirement on the reconstruction of missing transverse energy is the minimization of events that have a large amount of fake E_T^{miss}, i.e. due to instrumental effects. A large rate of such events could significantly enhance, for example, the backgrounds from QCD events to possible signals of new physics, such as supersymmetry. The wide calorimeter coverage, extending up to $|\eta| = 4.9$, already minimizes by design the impact from particles escaping at large pseudorapidities. However, the presence of non-instrumented transition region between different calorimetric systems may lead to occasional overestimates of the missing energy. Other effects, notably hadronic energy fluctuations, dead or noisy calorimeter cells and regions, may degrade the E_T^{miss} reliability.

In this chapter we discuss how to deal with instrumental (or fake) missing transverse energy, defined as the vectorial difference between the reconstructed E_T^{miss} and the

transverse momentum carried by neutral weakly interacting particles, as generated in Monte-Carlo simulations.

We first explore the possibility to put in evidence instrumental effects through the study of correlations between jet and E_T^{miss} directions. Since accurate E_T^{miss} direction measurement is important for this study, in Section 5.2 we estimate its expected resolution in ATLAS. Section 5.3 shows, through illustrative examples, the correlation of E_T^{miss} with the direction of jets.

In Section 5.4, we discuss the importance of constantly monitoring the E_T^{miss} variables during the data-taking operations and we describe the implementation of the E_T^{miss} monitoring infrastructure in ATLAS. Then, the capability of the monitoring system in detecting E_T^{miss} problems is tested in Section 5.5.

5.2 Measurement of E_T^{miss} direction

In QCD multi-jet events, where energy carried by neutrinos is typically small, fake E_T^{miss} will be the main component of the total reconstructed E_T^{miss}. Large hadronic energy fluctuations and losses cause the E_T^{miss} vector to be more likely aligned to the transverse momentum of jets. This is generally not true for events with a genuine missing transverse energy. Thus, in physics analysis looking for production of neutral weakly interacting particles, such as top studies or supersymmetry searches, an isolation cut on the angular difference between the E_T^{miss} vector and the jet directions can help to select the signal and reject the background. The application of such a criterion is analysis dependent; an example of its implementation can be found in the next section.

The isolation of E_T^{miss} relies, of course, on the reconstruction of the its direction. In Figure 5.1 (left) the difference between the reconstructed and generated $\phi_{E_T^{\text{miss}}}$ is shown for $t\bar{t}$, $Z \to \tau^+\tau^-$ and $W \to e^{\pm}\nu_e$ samples.

As it can be noticed, the E_T^{miss} angular resolution depends on the event topology. Indeed, it is related to the amount of true missing energy and of total visible energy, in particular of its hadronic part, since it is much more affected by mismeasurements. It also depends on additional instrumental effects causing E_T^{miss}, like dead or hot cells, but here we assume that such experimental issues can be kept under control. The strongest dependence, shown in the right plot of Figure 5.1, is on the true E_T^{miss} absolute value.

Once its value is fixed, the resolution differences between physics samples is reduced, especially for high missing transverse energies. For example, for $E_T^{\text{miss}} = 80$ GeV, the angular resolution only changes from 0.1 to 0.15 radians, switching from $W \rightarrow e^{\pm}\nu_e$ to $t\bar{t}$. Moreover, this resolution is smaller than the typical jet cone size. Thus, if we expect neutral weakly interacting particles produced far from jets, an isolation cut as small as the average expected jet cone radius can be applied with few signal events lost.

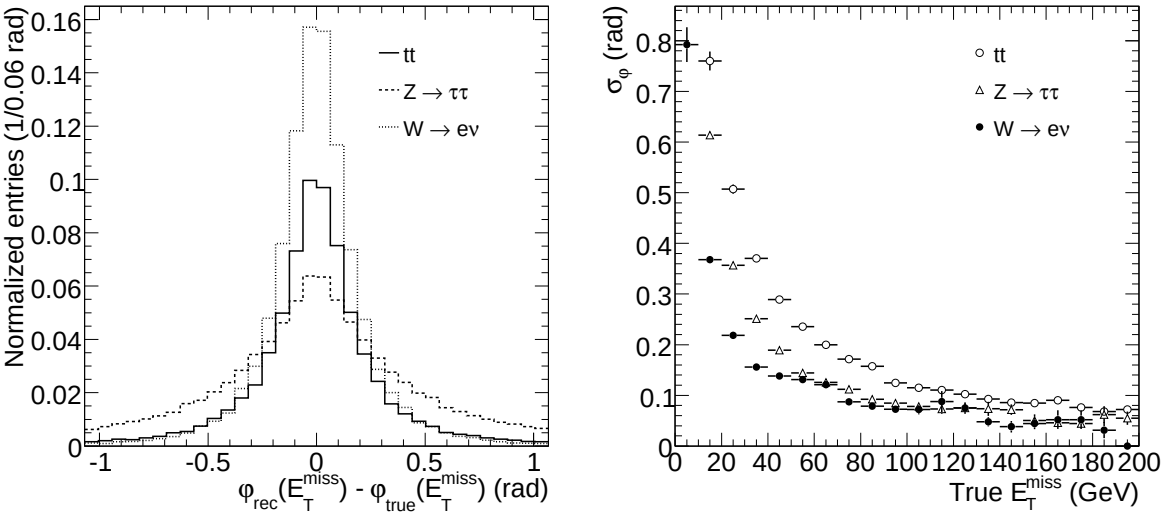

Figure 5.1: Angular difference between reconstructed and true E_T^{miss} (left) and angular resolution as a function of the true E_T^{miss} (right) for three different physics channels.

5.3 Fake E_T^{miss} correlation with jet direction

Problematic detector regions may be revealed by looking at the correlation between E_T^{miss} and the direction of jets, in particular in QCD di-jet events. Indeed, in this kind of events E_T^{miss} is mainly due to jet mismeasurements, which will affect more the E_T^{miss} component parallel to the di-jet axis than the perpendicular one.

Figure 5.2 shows the different behaviours of these two E_T^{miss} components as a function of the polar direction of the jet with highest transverse momentum (η_{jet}). This jet will be called in the following leading jet. A simulated sample of QCD di-jet events

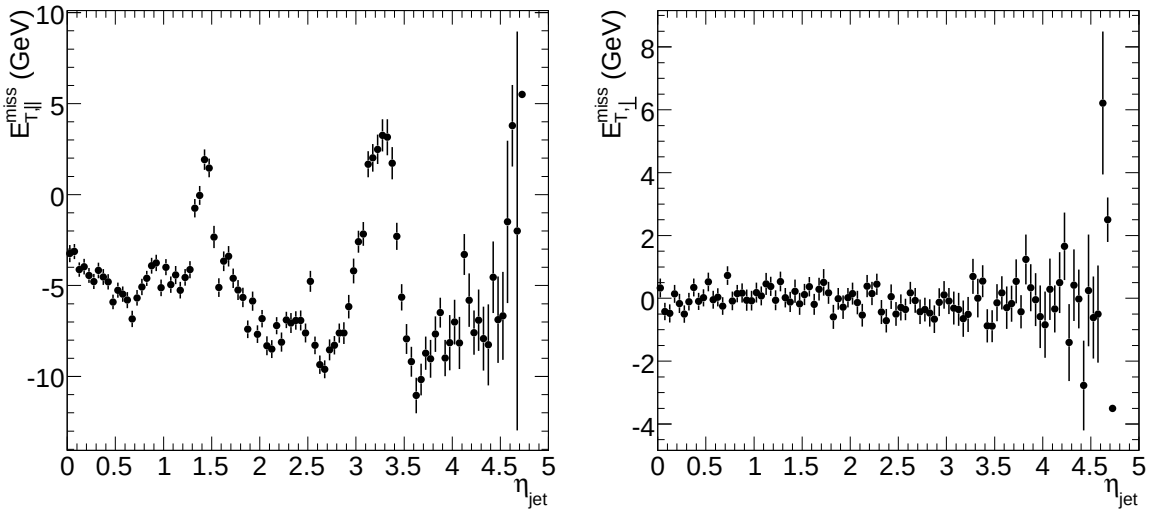

Figure 5.2: Missing transverse energy parallel and perpendicular components with respect to the direction of the jet with highest transverse momentum, as a function of η_{jet}. The used di-jet sample J3 is defined in the text.

with jet transverse momentum comprised between 70 and 140 GeV (sample J3) is used. The parallel component is sensitive to calorimeter gap regions ($\eta_{\text{jet}} \sim 1.5$ and $\eta_{\text{jet}} \sim 3.2$) while the perpendicular one is not. Detector defaults or wrong calibration sets in some calorimeter regions may be revealed as unexpected peaks in such plots.

Similarly, in a detector with ideal symmetry under rotations in ϕ, missing energy distribution is expected to be uncorrelated to the azimuthal direction of jets, or to the azimuthal direction of E_T^{miss} vector itself. Thus, observations of ϕ asymmetries may be a hint of instrumental problems.

While the distribution of the ϕ direction of E_T^{miss} should be flat when the azimuthal angle is calculated with respect to a fixed detector axis, this is not generally true when the ϕ coordinate is referred to the axis of a particular physics object produced in pp collisions. For example, QCD di-jet events have a preferred azimuthal orientation defined by the jet directions, that are back-to-back in the ATLAS transverse plane. As pointed out in the previous section, missing transverse energy depends deeply on the reconstructed energy flow along this axis, thus resulting more likely aligned to it.

This fact can be exploited to discriminate between QCD events and events with

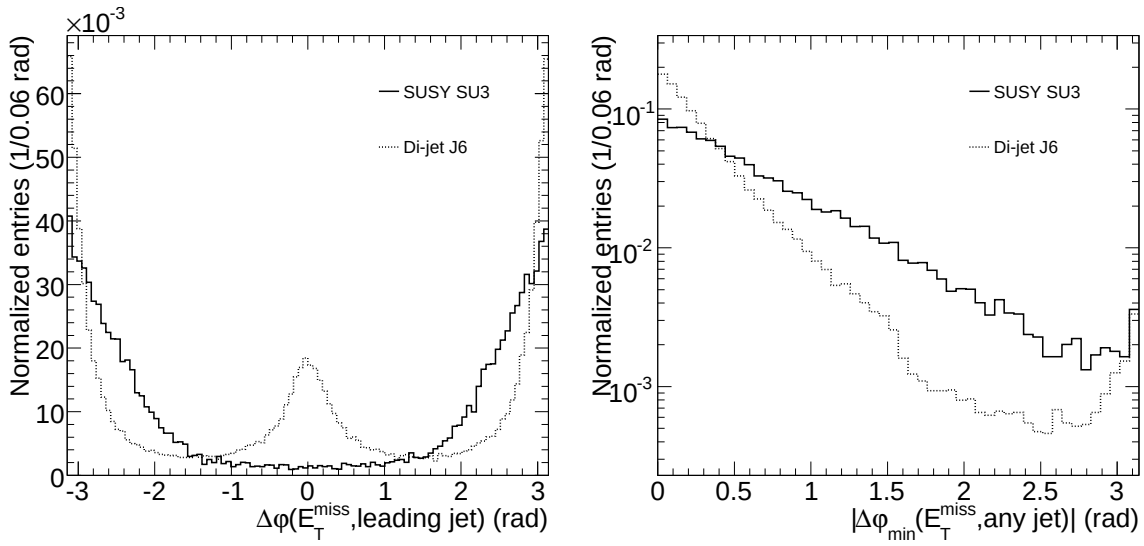

Figure 5.3: Normalized distribution of $\Delta\phi(E_T^{\mathrm{miss}}, \text{leading jet})$ and $|\Delta\phi_{\mathrm{min}}(E_T^{\mathrm{miss}}, \text{any jet})|$. Full (dotted) line represents a SUSY SU3 (di-jet J6) sample, defined in the text.

production of neutral weakly interacting particles. As an illustrative example, in the left plot of Figure 5.3 the normalized distribution of $\Delta\phi(E_T^{\mathrm{miss}}, \text{jet}) = \phi_{E_T^{\mathrm{miss}}} - \phi_{\mathrm{jet}}$ is shown for a SUSY SU3 (defined in Section 4.5) and a di-jet J6 (560 GeV $< p_{T,\mathrm{jet}} <$ 1120 GeV) samples for the leading jet in the event.

As it can be noticed from the right plot of Figure 5.3, another interesting variable potentially discriminating between E_T^{miss} signal and background is the angular difference between E_T^{miss} and its nearest jet, i.e. $|\Delta\phi_{\mathrm{min}}(E_T^{\mathrm{miss}}, \text{any jet})|$. The nearest jet is chosen among jets with transverse momentum greater than 15 GeV.

5.4 Monitoring of E_T^{miss} quality

Missing transverse energy is a global event variable. Indeed, it is built from the totality of the ATLAS calorimetric system and muon spectrometer. Because of this nature, missing transverse energy results are very sensitive to detector failures and inefficiency. In particular, it can be easily affected by an inaccurate calibration of the calorimeters.

For these reasons, physics analyses requiring non-zero E_T^{miss} rely on a good knowl-

edge of the detector systems and of the possible instrumental effects which may contribute to shift the event energy balance.

The identification and, eventually, the correction of experimental problems can be carried out during the physics analysis on the collected data. The studies reported in Section 5.3 are examples of such a procedure. However, this is only partially satisfying, since a large fraction of the collected events could then become unusable, reducing the integrated luminosity available for physics investigations. The majority of instrumental failures should be identified during, or immediately after, data taking, allowing for prompt intervention and thus minimizing data losses. During physics analysis, more refined corrections may still be applied; in some cases such refined corrections are mandatory.

The effort to achieve the best possible reliability of ATLAS data is referred to as monitoring of data quality. Its aim is to constantly control the status of the different systems involved in data taking and processing and to define standards to evaluate the goodness of the running conditions. The result of the examination is recorded and made accessible for physics analyses.

The overall data quality assessment is derived from the status of the trigger, of the detectors and of the reconstructed physics objects. Also the informations about the situation of each of them must be available. Moreover, the time interval of data-taking for which a quality evaluation is performed should be kept as fine as possible. Each one of such time periods, called luminosity blocks, are assigned a consistent set of quality status information. Figure 5.4 shows a schematic view of the data flow for data-quality assessment in ATLAS [88].

The control of data-quality starts with the online monitoring, using the computing resources of the trigger and data acquisition system. Detector readout drivers (ROD's) can accumulate statistics locally based on one or more channels, the L2 trigger can access part of events (one or more RoI's), while at event filter level entire events are assembled, though resources for monitoring are severely restricted by time requirements. In addition the detector control system (DCS) information includes items like detector high-voltage and electronics crate low-voltage status.

Beyond the online environment, the ATLAS data quality extends to the offline reconstruction systems. The first full ATLAS event reconstruction occurs at the *Tier-0*

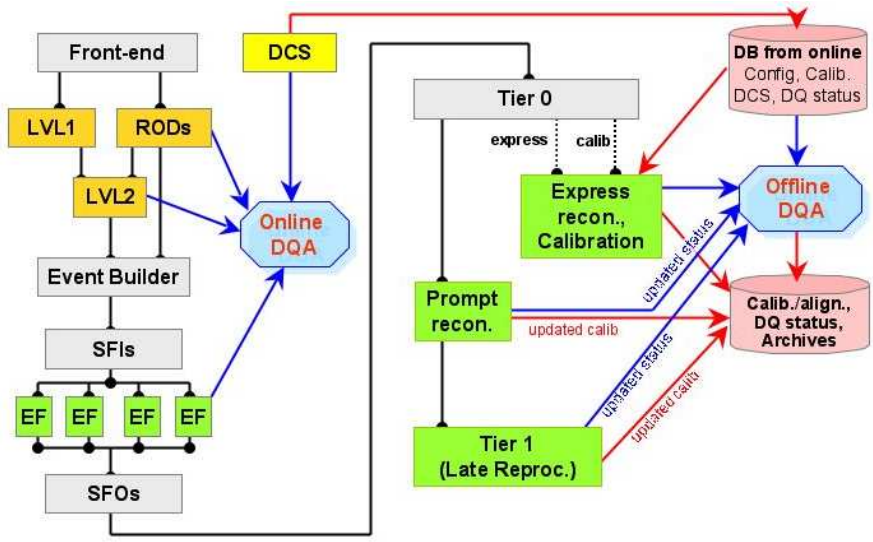

Figure 5.4: Schematic view of the data flow for data-quality assessment in ATLAS [88].

computer centre. Unlike the event filter where a processing time of only about one second is permitted per event, requiring simplified reconstruction algorithms, the *Tier-0* uses the full offline event reconstruction and some tenths of seconds are available per event. More detailed monitoring is therefore possible at the *Tier-0*. The monitoring of subdetectors can be completed by accurate tests of combined performance for particle object reconstruction.

Collected data are passed to the *Tier-0* through different types of streams. The express and calibration streams are processed within few hours after acquisition; they contain either full events passing restricted trigger requirements (express stream) or partial events (calibration streams). The infrastructure should guarantee the ability to feedback data-quality error and warnings present in such streams to data-taking controllers. The full data stream, containing the complete set of events, is reconstructed in 24 to 48 hours after acquisition. The output of data-quality monitoring for the express and calibration streams can be used to flag the status of events when performing the full data stream reconstruction. It is conceivable, at least eventually, that events with particularly bad data quality could skip the reconstruction step. It would also be possible to write preliminary data-quality status information directly into the output formats designated for physics analyses.

Monitoring of missing transverse energy is inserted in the data-quality infrastructure. Besides being necessary to ensure reliable physics analyses, the constant control of E_T^{miss} variables, because of their sensitivity to instrumental failures, may also help to promptly address large scale detector problems.

Histograms of interesting variables are filled during the reconstruction process. Basic and simple distributions should be available for non-expert control during data taking. More detailed plots should be accessible in case suspicious results are found. For missing transverse energy, the following kinematic variables are monitored: E_T^{miss}, E_x^{miss}, E_y^{miss}, $\phi_{E_T^{\text{miss}}}$ and the total scalar sum of calorimeter cell transverse energies. Each of these variables is sampled not only for the final E_T^{miss}, but also for the different terms in Equation 4.6 and, in addition, for the calorimetric missing transverse energy before cell calibration. Similarly, missing transverse energy terms built from single calorimeter subsystems (electromagnetic barrel and end-caps, tiles, HEC and FCAL) are also considered. To further enhance the sensitivity, the E_T^{miss} correlation with jet directions, as those presented in Section 5.3, is also monitored.

5.5 Sensitivity tests of the E_T^{miss} monitoring system

In order to test the capability of the monitoring system in detecting E_T^{miss} problems, a special sample of QCD di-jets (J6) has been simulated within a problematic ATLAS configuration. The response of a few calorimeter cells is turned off, causing a complete loss of the energy deposited inside them. The amount of silent cells corresponds to about 0.1% of LAr electromagnetic high-voltage lines and two LAr and two tile front-end electronic units. The pattern of the introduced failures is reported in Figure 5.5. The monitoring algorithms are executed on about 1500 events. This statistics corresponds to a couple of minutes of data taking, assuming a trigger rate of order 10 Hz on single energetic jets. The resulting histograms are compared to reference distributions from ideal detector simulations.

The x and y components of missing energy show (Figure 5.6) peaks slightly shifted from the expected zero value. The discrepancy from the reference sample becomes striking for E_T^{miss} angular distribution, shown in Figure 5.7 (left). The E_T^{miss} component parallel to the leading jet direction shows a similar behaviour (Figure 5.7, right): since

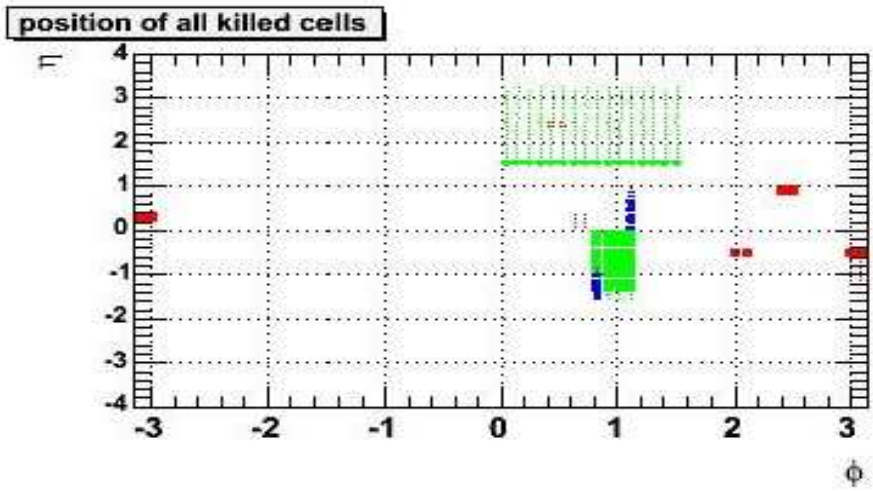

Figure 5.5: Pattern of the introduced calorimeter failures. Red regions correspond to dead LAr high-voltage lines, while green and blue indicate respectively LAr and tile silent cells because of electronic problems.

a jet falling inside the critical region is often lost or has badly underestimated energy, the second jet in the event, that now experimentally becomes the leading jet, points toward the direction opposite to E_T^{miss}.

Informations on the nature of the underlying problems may come from summary plot of the means of the E_T^{miss} variables for different E_T^{miss} terms and calorimeter subsystems, such as those in Figure 5.8. The E_y^{miss} mean for cryostat and muon terms are compatible with distributions centered on zero, but calorimeter cell terms are significantly away from $\langle E_y^{\text{miss}} \rangle = 0$, independently on the calibration. Thus, the failure seems to be related to calorimeters. Similarly, we can argue that electromagnetic barrel and hadronic end-caps may be problematic, since E_y^{miss} is more asymmetric if the missing energy calculation is restricted to these subsystems. An interaction with deeper calorimeter investigations is necessary to determine the exact cause and the interventions needed.

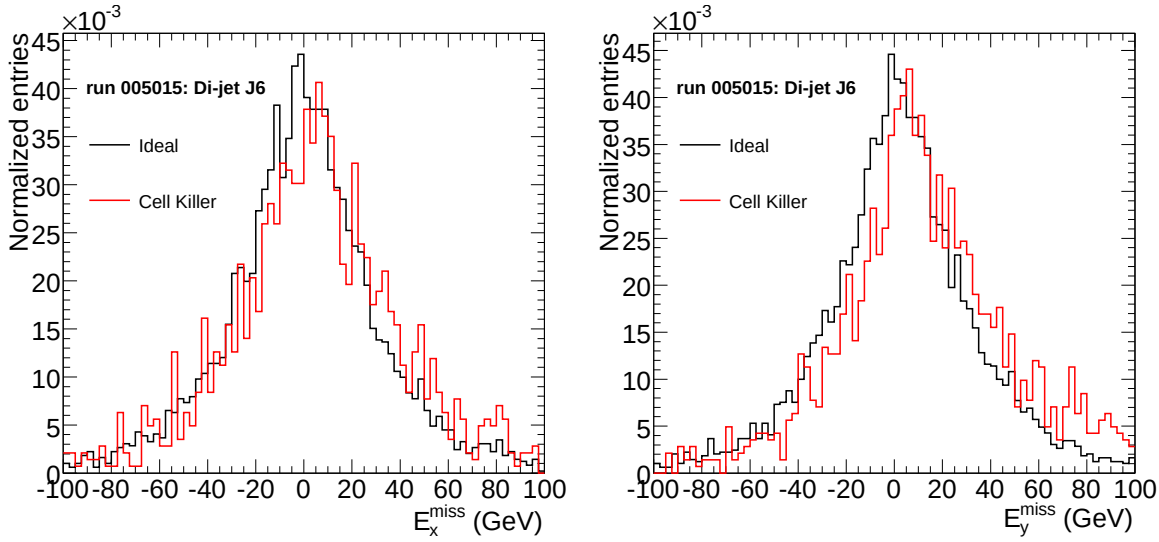

Figure 5.6: Distributions of x and y missing energy components, for ideal detector response (black line) and for detector simulation with calorimeter failures (red line).

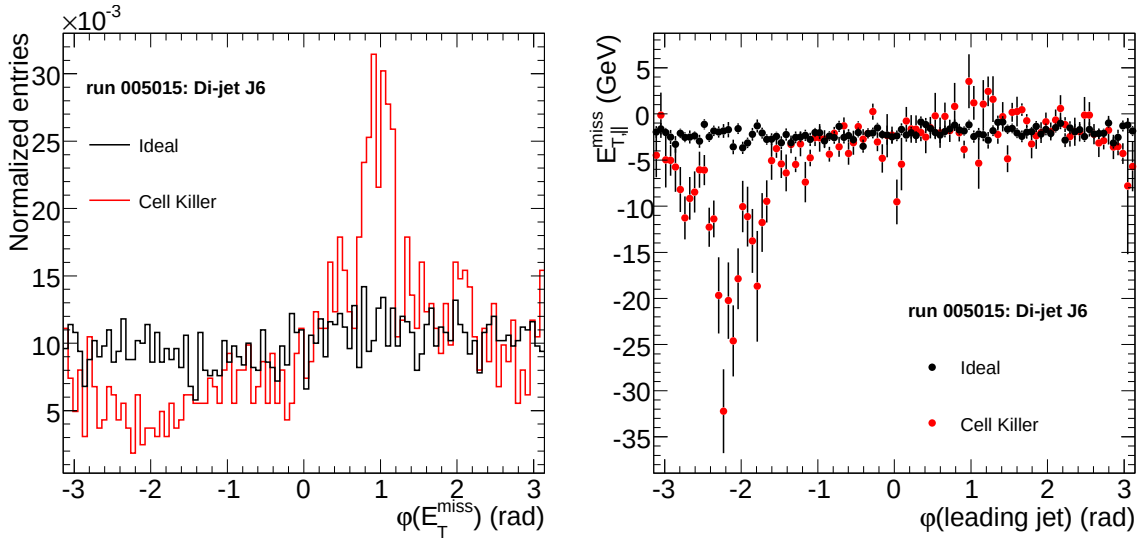

Figure 5.7: Angular distribution of E_T^{miss} (left) and E_T^{miss} component parallel to the leading jet direction as a function of azimuthal jet angle. Black line corresponds to ideal detector response and red line to detector simulation with calorimeter failures.

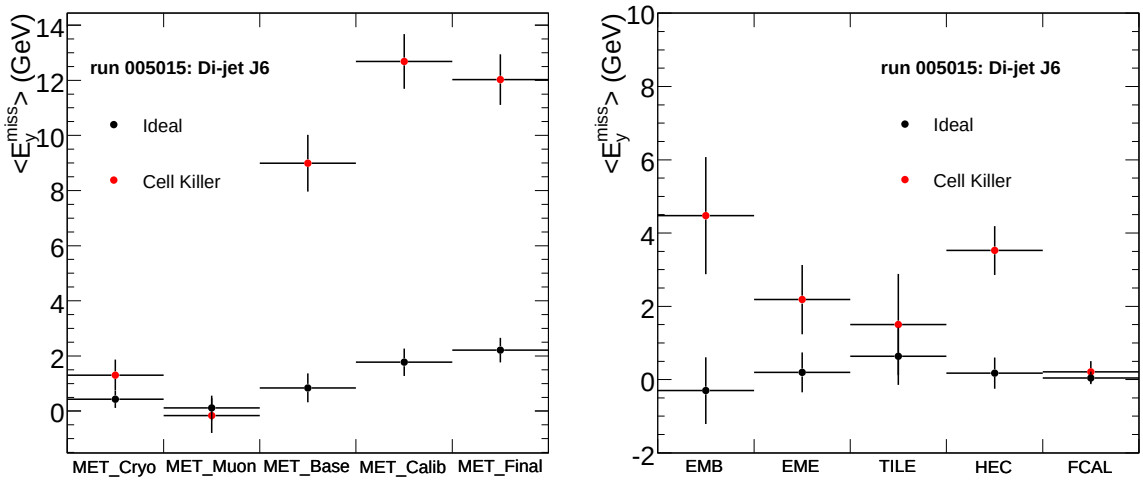

Figure 5.8: Summary plot of the means of the E_y^{miss} distributions for different E_T^{miss} terms and calorimeter subsystems. The E_T^{miss} terms are, from left to right, the energy lost in cryostats (Equation 4.5), the muon contribution, the total energy deposited in the calorimeters before and after calibration (Equation 4.4) and the final calculation of E_T^{miss} (Equation 4.6). All these are defined in Section 4.1.6. The calorimeter subsystems are, from left to right, the electromagnetic barrel and end-caps, the tiles, the hadronic end-caps and the forward calorimeter, detailed in Section 3.4.

6

HIGGS SEARCHES IN CASCADE DECAYS OF SUSY PARTICLES

6.1 Motivations and phenomenology

In the context of the Minimal Supersymmetric Standard Model, the lightest CP-even Higgs boson h can be produced in proton collisions either through direct interaction of SM particles, such as gluon-gluon fusion, or through cascades of SUSY particles. In the present work we will consider the possibility of observing the h boson via the second mechanism with the ATLAS detector. In this case, in association with the Higgs boson, a missing transverse energy signature, typical of R-parity conserving SUSY scenarios, can be reconstructed and exploited to reduce the background, making it possible to study the dominant decay channel $h \to b\bar{b}$, otherwise covered by the enormous QCD continuum.

Figure 6.1 shows a display of the signals deposited in the ATLAS detector by a simulated SUSY event containing a Higgs boson decaying into two b-quarks. Two strongly interacting SUSY particles, in the present case a $\tilde{q}_R$ and a $\tilde{q}_L$, are produced in the pp interaction. The former decays directly into a stable $\tilde{\chi}_1^0$ and a quark, while the left squark generates a Higgs boson through a two-step cascade:

$$\tilde{q}_L \to \tilde{\chi}_2^0 q \to \tilde{\chi}_1^0 h q. \tag{6.1}$$

In the event display, the four bundles of collimated tracks, starting at the detector centre and ending with large energy deposits in the calorimeters, are caused by four

hadronic jets, two of which are the Higgs disintegration products while the two others come from the decay of the squarks. Their total transverse energy is balanced by the dashed line crossing the whole detector, representing the reconstructed missing transverse energy.

The possibility of observing such events has already been addressed in an ATLAS Technical Design Report (TDR) analysis [66, 67]. However, since then, the experimental limits on the Higgs mass coming from direct searches at LEP have been considerably tightened, excluding a large region of the mSUGRA parameter space, in particular for values of $\tan\beta \lesssim 5$ [89] where TDR analyses are performed. Above this value, the left and right third generation squark mixing may lead to a significant splitting between the mass eigenstates. This results in lighter stop and sbottom squarks with respect to the other generations, enhancing the fraction of gluinos producing b-quarks during the cascade process and increasing the background for Higgs searches in the $b\bar{b}$ channel. The scenarios chosen for this analysis will reflect this situation.

Once phenomena beyond the Standard Model are discovered, it is important to determine the masses and couplings of the newly observed particles. At the LHC, mass information is provided by thresholds and edges in the invariant mass plots of jets and leptons from SUSY cascades. For the purpose of these SUSY measurements, one of the most promising channels has the clear di-leptonic signature given by the cascade

$$\tilde{\chi}_2^0 \to \tilde{\ell}^{\pm}\ell^{\mp} \to \tilde{\chi}_1^0\ell^{\pm}\ell^{\mp}. \tag{6.2}$$

On the other hand, to have a copious Higgs production, as needed in the case under study, this channel must be closed, leaving room for the $\tilde{\chi}_2^0$ decay modes

$$\tilde{\chi}_2^0 \to \tilde{\chi}_1^0 h \text{ and } \tilde{\chi}_2^0 \to \tilde{\chi}_1^0 Z, \tag{6.3}$$

which are otherwise very suppressed. In the present work, we show that, even in this case, information about the SUSY spectrum can be recovered, starting from the Higgs and reconstructing back its production chain.

The chapter is structured as follows. The next section describes the event generation and detector simulation used. Then a scan of the mSUGRA parameter space is performed and two benchmark points inside this model are chosen. The analysis of the experimental signatures is developed using a fast-simulation description of the

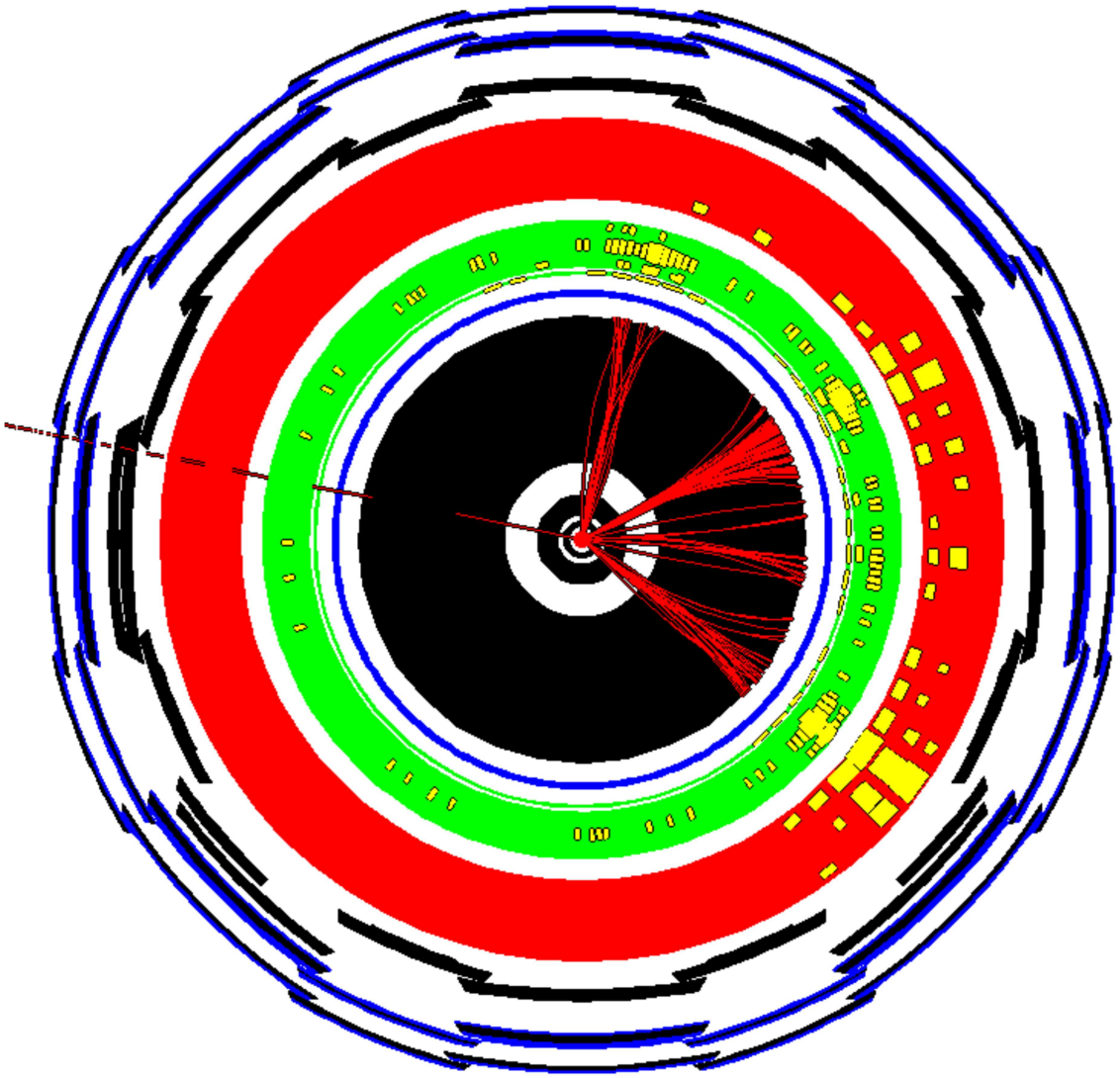

Figure 6.1: Display of the ATLAS detector signals produced by a simulated SUSY event containing a Higgs boson decaying into two b-quarks. The four bundles of collimated tracks, starting at the detector centre and ending with large energy deposits in the calorimeters, are caused by four hadronic jets, two of which are the Higgs disintegration products while the two others come from the decay of strongly interacting SUSY particles. Their total transverse energy is balanced by the dashed line crossing the whole detector, representing the reconstructed missing transverse energy.

ATLAS detector: Section 6.4 details the $h \to b\bar{b}$ analysis, Sections 6.5 and 6.6 address the problem of SUSY mass measurement and, finally, the possibility of observing the Higgs decaying into two photons is explored in Section 6.7. In the last section, the fast-simulation technique is tested against the performances of a fully simulated ATLAS detector; the Higgs search analysis is completely repeated with fully simulated samples. Moreover, some details on the trigger decision of interest for the relevant channels are given.

6.2 Event generation and detector simulation

The present analysis is performed inside the Minimal SUGRA model, whose input parameters are defined at the unification energy scale. The mass spectrum and couplings of the supersymmetric particles relevant for the LHC experiment are obtained by solving the renormalization group equations at the electroweak energy scale. The `Isajet 7.74` [90] code is used for this purpose. The top mass is fixed at 175 GeV. This convention will be kept throughout the whole chapter.

The generation of SUSY events is performed with the combination of the fixed-order Monte Carlo `Herwig 6.510` [91, 92] and `Jimmy 4.31` [93], which simulates multiple parton scattering.

For the Standard Model background samples another generation technique is chosen. Fixed-order Monte Carlo generators only give a good description of the hadronic activity of the event in the soft-collinear approximation, so they usually underestimate the rate of events with a high number of energetic jets. This makes them unsuitable for SUSY analyses. Instead, `Alpgen 2.11` [94], a so-called matrix element generator, calculates the exact kinematics of N-parton events. It is then interfaced to `Herwig` and `Jimmy`, to complete the parton evolution and the underlying event. The MLM matching prescriptions [95] are adopted to avoid double counting.

In Sections 6.4, 6.5, 6.6 and 6.7 the detector simulation for both SUSY and SM events is performed with the `Atlfast` package [96]. In particular, we set it to provide a 60% b-jet identification efficiency, with a mistagging rate equal to 1/10 against jets coming from c partons and equal to 1/100 for all the other jets, as full-simulation studies predict for the ATLAS detector (Section 4.1). Lepton and photon identification are

fixed at 100% effiency and purity, but for $h \to \gamma\gamma$ studies, an additional correction has been added in order to reproduce the expected 80% identification efficiency on each photon and the (pessimistic) probability of 1/500 for reconstructing a jet as a photon.

This fast-simulation analysis, thanks to the large statistics of signal and background events, allows for a complete exploration of the measurements possible in the considered scenarios, even at very high luminosity. However, in order to obtain a more realistic estimate of the results of low-luminosity analyses, the study is repeated in Section 6.8 performing a complete simulation of the detector geometry. The full ATLAS simulation and event reconstruction are based on the ATLAS software `Athena 12`.

6.3 Scan of Minimal SUGRA parameter space

In order to set the benchmark points, we perform a scan of the Minimal SUGRA parameter space. The interesting points must have a $BR(\tilde{\chi}_2^0 \to \tilde{\chi}_1^0 h) \gtrsim 0.5$, to ensure a sufficient Higgs production, and be compatible with the exclusion limits from direct searches for SUSY particles and Higgs bosons [28, 35, 89].

Moreover, since a connection between cosmological cold dark matter and particle physics beyond the Standard Model is expected and well motivated, one can also require the stable lightest supersymmetric particle to be the dark matter constituent. In this case its cosmological relic density should be inside the 2σ range measured by the WMAP experiment [38]:

$$0.088 < \Omega_{\rm cdm} h^2 < 0.123. \tag{6.4}$$

For the present scan, the LSP relic density has been computed with `MicrOMEGAs 2.0` [97, 98, 99].

In Figure 6.2, the second lightest neutralino decay rate to Higgs is shown as a function of the mSUGRA input parameters M_0 and $M_{1/2}$, with A, $\tan\beta$, and sgnμ fixed to (200 GeV, 20, +) and (0 GeV, 54, +) for the left and right plots respectively. The white regions are excluded either experimentally or because spontaneous electroweak symmetry breaking does not occur. Inside the grey region the LSP is the stau, while everywhere else it is the lightest neutralino. The black line parallel to the M_0 axis is the limit above which the lightest Higgs is heavier than 114 GeV, according to the 95%

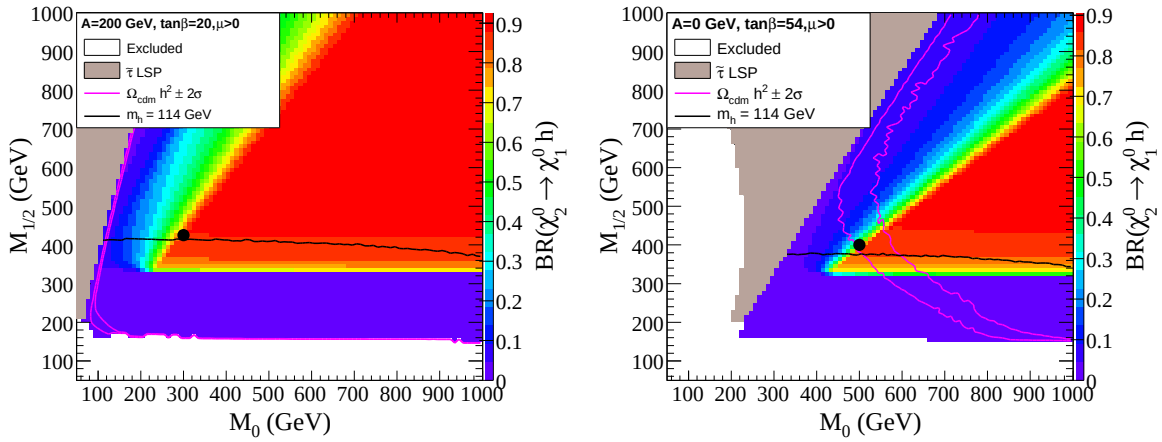

Figure 6.2: The second lightest neutralino decay rate to Higgs as a function of the mSUGRA input parameters M_0 and $M_{1/2}$, for two values of (A, $\tan\beta$, sgnμ). The narrow region between the pink contours is where the LSP relic density is 2σ compatible with the cosmological cold dark matter density measured by the WMAP experiment. The two chosen benchmarks are indicated by the black dots.

confidence level LEP exclusion limit. The pink contours set the region of compatibility with WMAP observations.

The region satisfying $BR(\tilde{\chi}_2^0 \to \tilde{\chi}_1^0 h) \gtrsim 0.5$ is a triangle bounded from above by the opening of the $\tilde{\chi}_2^0 \to \tilde{\ell}^{\pm}\ell^{\mp}/\tilde{\nu}_\ell\bar{\nu}_\ell$ decay channel and from below because $m_{\tilde{\chi}_2^0} - m_{\tilde{\chi}_1^0} < m_h$. Notice that, if open, the decay to Higgs always dominates the $\tilde{\chi}_2^0 \to \tilde{\chi}_1^0 Z$ mode, because in mSUGRA models the two lightest neutralinos are mostly gauginos, so that the higgsino-gaugino-Higgs vertex is enhanced with respect to the higgsino-higgsino-gauge one.

At intermediate $\tan\beta$, we fix a benchmark at

$$M_0 = 300 \text{ GeV},\ M_{1/2} = 425 \text{ GeV},\ A = 200 \text{ GeV},\ \tan\beta = 20,\ \mu > 0, \qquad \text{(Point 1)}$$

outside the WMAP constraints. This point is chosen because it will have a low $b\bar{b}$ background and hence a clear $h \to b\bar{b}$ signal. To have a benchmark inside the region preferred by WMAP, we have to increase $\tan\beta$, finding

$$M_0 = 500 \text{ GeV},\ M_{1/2} = 400 \text{ GeV},\ A = 0 \text{ GeV},\ \tan\beta = 54,\ \mu > 0. \qquad \text{(Point 2)}$$

The increase in $\tan\beta$ greatly enhances the production of b's coming from gluino decays, increasing the background for $h \to b\bar{b}$, as explained in Section 6.1. For instance, for Point 2 the branching ratio of gluino to heavy flavours is around 90%, about two times greater than for Point 1. Moreover, while at Point 1 the first and second generations of squark are lighter than the gluino, at Point 2 this is not true and 20% of squarks decay to gluinos. These characteristics cause Point 2 to be a very challenging scenario to test the ATLAS discovery potential of Higgs produced in SUSY events.

In other regions of mSUGRA, or general MSSM, the background for Higgs analysis may be potentially increased by two facts:

- larger branching ratio of $\tilde{u}$, $\tilde{d}$, $\tilde{c}$ and $\tilde{s}$ to gluino, due for instance to a larger available phase space;

- SUSY particle production dominated by $pp \to \tilde{g}\tilde{g}$ process, instead of $pp \to \tilde{q}\tilde{g}$ as it is for Points 1 and 2.

For points at which one or both these items are true and at which the gluino still decays mainly to heavy flavours, an early Higgs discovery would be difficult to attain even in case of copious Higgs production. However, since good signal significance can be achieved for the two benchmark points with 10 fb^{-1} (see Section 6.4), with higher luminosity it might be possible to observe the $h \to b\bar{b}$ even in such unfavorable situations.

6.4 Searches for $h \to b\bar{b}$ signature

Even though $b\bar{b}$ is the dominant decay mode of a light Higgs ($m_h \lesssim 140$ GeV), the observation of this channel at the LHC is very challenging because of the enormous QCD background. In the context of the Standard Model, the background is reduced by requiring the Higgs to be produced in association with a pair of top quarks or a weak gauge boson. In SUSY cascades, Higgs bosons are always produced in association with neutral weakly interacting particles, whose passage through the ATLAS detector can be revealed as a non-zero balance in the transverse component of the total measured energy. This additional signature considerably suppresses the background and makes

it possible to reconstruct the resonance of the b-tagged jet pairs with invariant mass peaking around the Higgs mass.

Standard Model events with similar signatures, which are backgrounds for this analysis, are events with neutrino production, causing a genuine E_T^{miss} signal, and QCD events with fake E_T^{miss} generated by instrumental effects. Between them, the most critical are electronic and pile-up noise and poor jet energy reconstruction, for example due to cracks or dead regions in the calorimeter system. Thus, a good understanding of the detector to minimize such defects is needed to control the QCD background. Also SUSY events themselves can constitute a background, as they contain many b-jet candidates, both true and mistagged. They can be divided in two categories: SUSY cascades without and with production of a Higgs decaying to $b\bar{b}$. In the latter case, the potential signal event becomes a noise because the selected b pair is not the one coming from the Higgs. In the following we will refer to the first type simply as *SUSY background* and to the second as *combinatorial background*.

The following selection cuts are applied:

1. $E_T^{\text{miss}} > 300$ GeV;

2. two light-flavoured jets with $p_T > 100$ GeV;

3. two b-jets with $p_T > 50$ GeV;

4. no electrons nor muons with $p_T > 10$ GeV.

The first two cuts are typical of SUSY searches in ATLAS, while cut 4 helps to suppress $t\bar{t}$ and W backgrounds. The distributions of E_T^{miss}, transverse momentum of the two leading light-flavoured jets, number of tagged b-jets and transverse momentum of the two leading b-jets are shown in Figures 6.3 and 6.4. Distributions for signal, SUSY background and $t\bar{t}$ background are shown. While $t\bar{t}$ events are strikingly different, distributions for signal and SUSY background are, not surprisingly, much more similar.

In cases where three or more b-jets with transverse momentum greater than 50 GeV are found in a single event, we have to choose which pair is coming from the Higgs decay. We decide to keep the second and third leading b-jets. This is because an important source of b-jets is the decay of a sbottom squark to $\tilde{\chi}_2^0$ and b and since

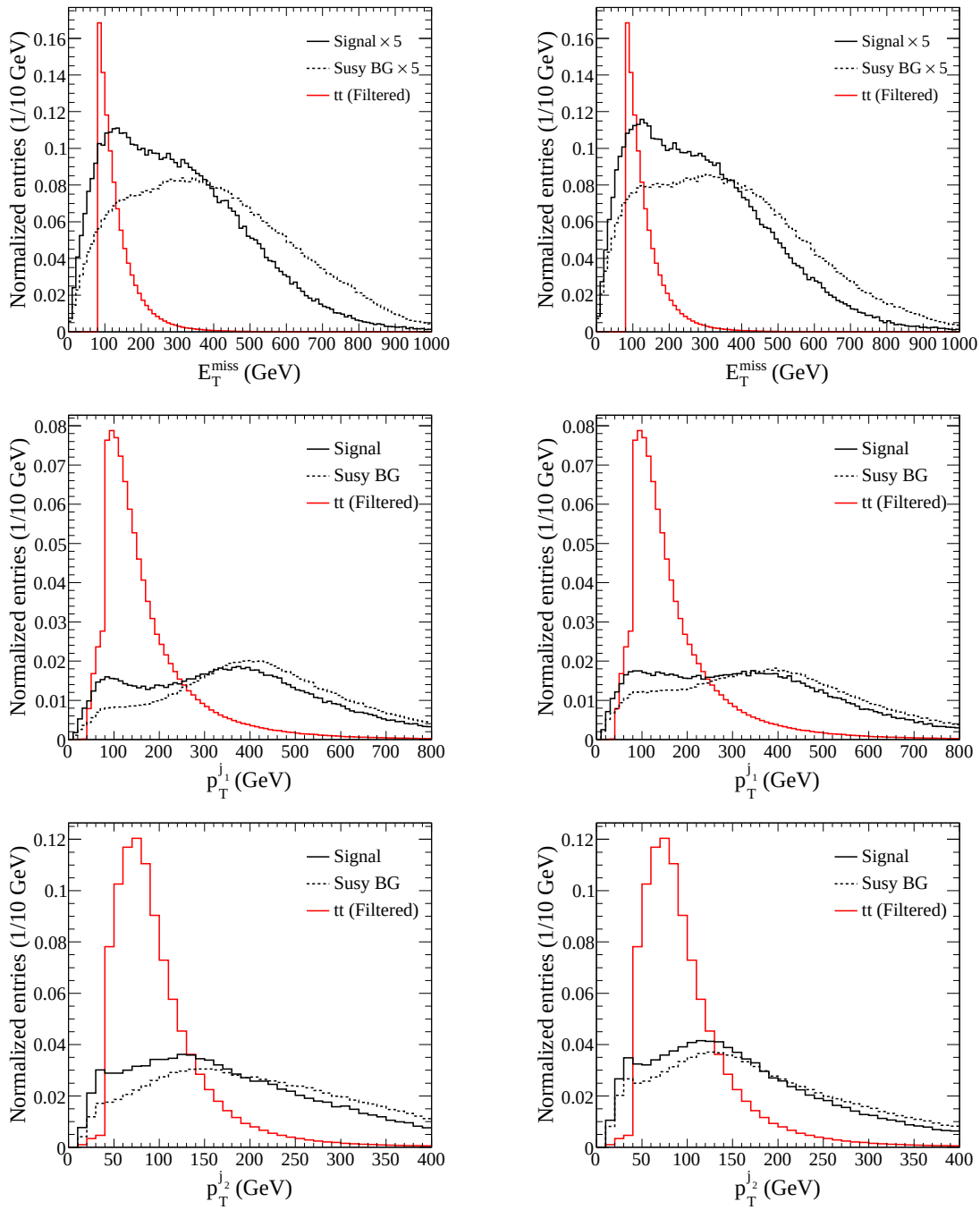

Figure 6.3: Distributions of E_T^{miss} and of the transverse momenta of the two leading light-flavoured jets for signal, SUSY background and a $t\bar{t}$ sample filtered by asking $E_T^{\text{miss}} > 80$ GeV and at least two jets (either light- or b-flavoured) with $p_T > 80$ GeV and 40 GeV respectively. Both mSUGRA Point 1 (left) and 2 (right) are shown.

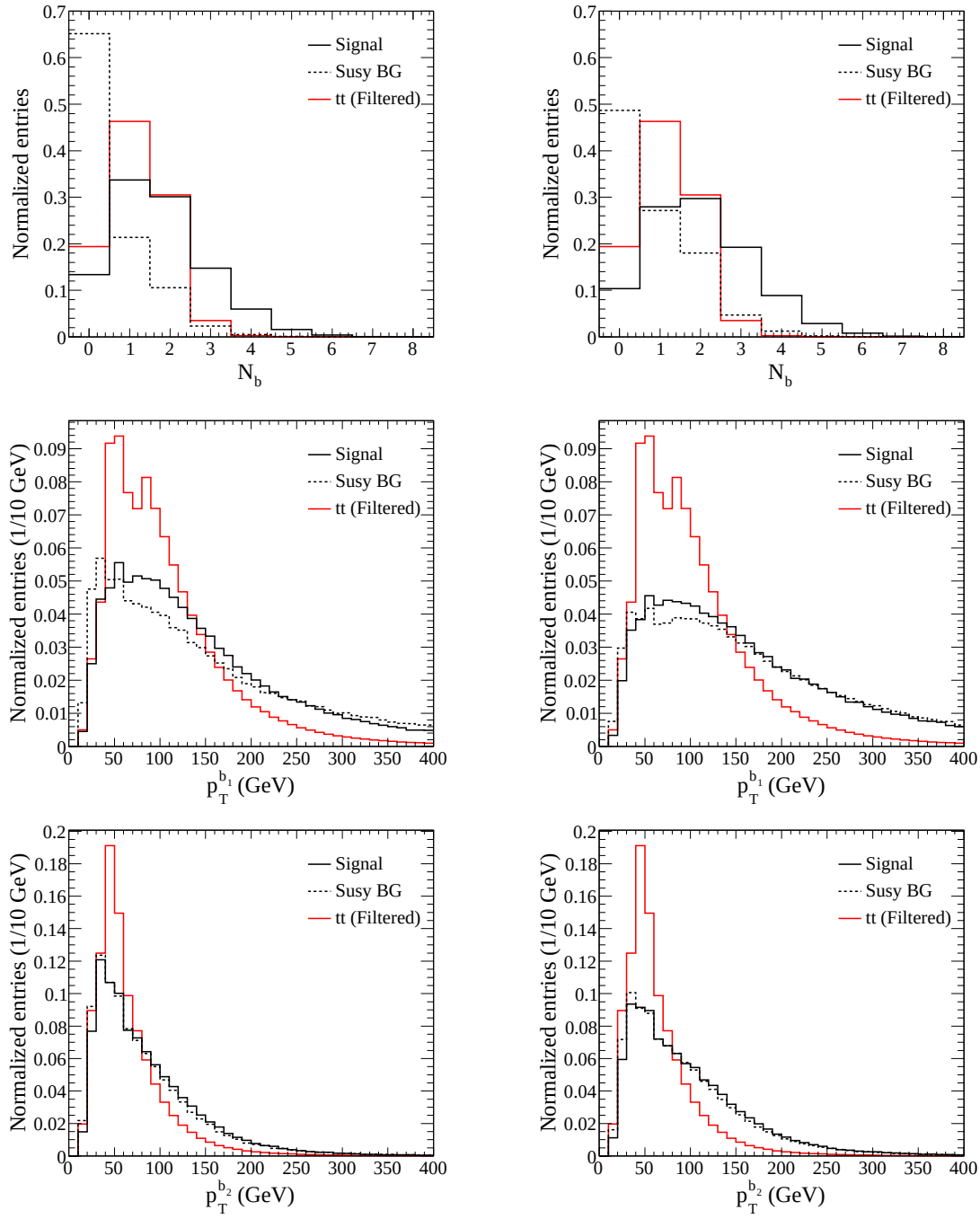

Figure 6.4: Distributions of the number of tagged b-jets and of the transverse momenta of the two leading b-jets for signal, SUSY background and a $t\bar{t}$ sample filtered by asking $E_T^{\text{miss}} > 80$ GeV and at least two jets (either light- or b-flavoured) with $p_T > 80$ GeV and 40 GeV respectively. Both mSUGRA Point 1 (left) and 2 (right) are shown.

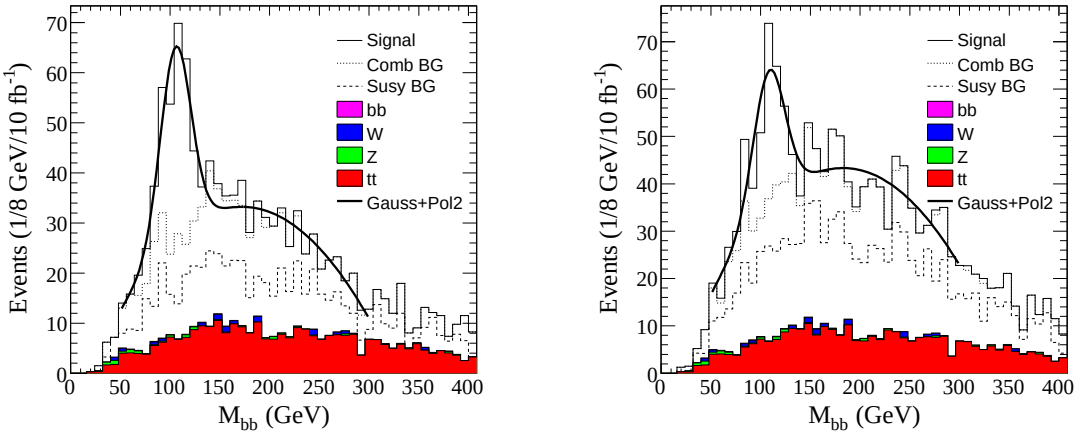

Figure 6.5: The invariant mass of the selected b-jet pairs is shown for 10 fb^{-1} for mSUGRA Point 1 (left) and Point 2 (right).

$m_{\tilde{b}} - m_{\tilde{\chi}_2^0} \sim 500$ GeV $> m_h$ the sbottom daughters get more allowed phase space than the Higgs daughters and thus, in general, higher p_T.

In Figure 6.5 the invariant mass of the selected b-jet pairs is shown for mSUGRA Points 1 and 2, assuming 10 fb^{-1} of collected luminosity. The coloured histograms correspond to different SM backgrounds, the dashed and dotted lines are the SUSY and combinatorial backgrounds respectively. These last two, together with the $t\bar{t}$ production, are the most important backgrounds. The black curve is the result of a least squares fit to a Gaussian function, representing the Higgs resonance, superimposed on a second degree polynomial background. The estimated number of signal and background events is obtained by counting the b pairs with invariant mass inside a ± 25 GeV range around the fitted peak centre. The achieved signal significance, computed in the Gaussian approximation as the number of signal events over the root of the background, is 12 and 8 for the two scenarios.

Table 6.1 summarizes the expected event rates after the application of the selection cuts 1 to 4 and after the additional mass window request.

It should be noticed that the two scenarios we are considering lie in the so-called decoupling region, since $m_A^2 \gg m_Z^2$. In this case the lightest neutral Higgs boson h behaves much like the SM Higgs boson and the quoted significances can be directly compared with the SM analyses. None of the most promising analyses (i.e. inclusive

Point 1	Signal	Comb BG	Susy BG
No cuts		7700	15300
Cut 1, 2, 3	237	528	582
Cut 4	192	382	367
± 25 GeV mass window	166	63	72
$\Delta\phi(h, E_T^{\text{miss}}) < 1$	149	49	46

Point 2	Signal	Comb BG	Susy BG
No cuts		6400	16600
Cut 1, 2, 3	181	627	1132
Cut 4	143	472	695
± 25 GeV mass window	122	76	117
$\Delta\phi(h, E_T^{\text{miss}}) < 1$	91	56	71

Standard Model	$t\bar{t}$	Z	W	$b\bar{b}$
Cut 1, 2, 3	717	10	24	2
Cut 4	392	10	11	2
± 25 GeV mass window	45	2	1	1
$\Delta\phi(h, E_T^{\text{miss}}) < 1$	39	1	1	1

Table 6.1: Summary of the number of expected SUSY and SM events after the application of the different selection cuts, for 10 fb^{-1} of integrated luminosity. The last line of each table show the effect of an additional cut on the azimuthal angle between the reconstructed Higgs and the missing transverse energy, as detailed in the last paragraph of the section.

$h \to \gamma\gamma$, weak boson fusion $h \to \tau^+\tau^-$ and $t\bar{t}$-associated production of $h \to b\bar{b}$) has a higher estimated Higgs discovery potential.

To improve the signal significance even further, a cut on the angular separation between the two b partons was proposed in the TDR analysis [67] to reduce the $t\bar{t}$ contamination. Indeed, since the SUSY cascade is started by heavy particles (squarks and gluinos), the Higgs is highly boosted and its decay products are most likely to be nearby. Nevertheless, such a cut is correlated with the two-parton invariant mass, causing the background to be pushed to low mass values. Thus, even though the total number of background events could be reduced by such a cut on angular separation, the number of background events falling inside the Higgs peak mass window would increase. The same argument applies to lowering thresholds on the transverse momenta of the b's. On the contrary, by raising these cuts, we would obtain the opposite effect, since the background would be moved to high-mass values, but at the same time we would lose signal events. Thus, the choice of the 50 GeV threshold is a sensible compromise between the two effects.

Another cut found in the literature is a veto on additional b-tagged jets, in order to suppress the combinatorial background. A SUSY cascade with a Higgs decaying to $b\bar{b}$ contains on average two b-quarks more than the other cascades, as can be deduced from Figure 6.4, and thus the benefit of this veto depends on the number of b's in SUSY events. For instance, the effect of this veto on the signal significance is opposite for the two benchmarks. Because of this scenario dependence we do not apply this cut.

A cut on the angular separation between the Higgs and the lightest neutralino produced in association may be more useful. Indeed, for both points considered, the mass difference between the neutralino mass eigenstates 1 and 2 is of order of m_h, so the h and the $\tilde{\chi}_1^0$ will be emitted roughly collinearly. Experimentally, the $\tilde{\chi}_1^0$ direction cannot be measured. The only observable is the missing energy direction in the transverse plane, which corresponds to the azimuthal angle of the vector sum of all the escaping particles produced in the event, typically the two LSP. A small increase in the signal to background ratio is seen if $\Delta\phi(h, E_T^{\text{miss}})$ is required to be less than 1 radian, as reported in the last line of Table 6.1. Figure 6.6 shows the distribution of this variable for different samples. We nevertheless prefer not to apply this selection, because it is of course a model-dependent cut and may not work if the mass splitting between $\tilde{\chi}_1^0$

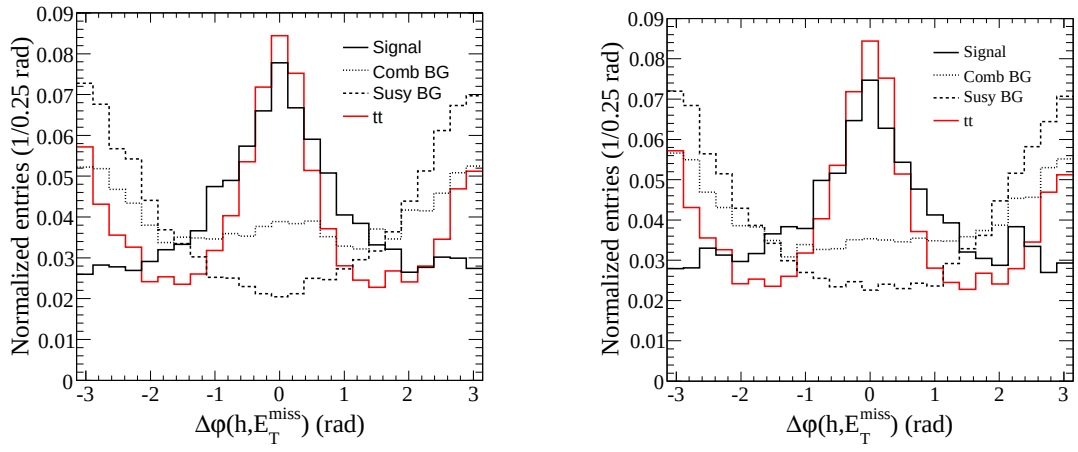

Figure 6.6: Azimuthal angle difference between the missing transverse energy and the reconstructed lightest Higgs. The SUSY sample used is Point 1 in the left plot and Point 2 in the right plot.

and $\tilde{\chi}_2^0$ is higher than at the points presented.

6.5 More complex signatures involving b pairs

Since the cascade chain of SUSY particles always ends up with an LSP that escapes detection, no invariant mass peak of supersymmetric particles can be reconstructed at the LHC. Invariant masses of two or more particles coming from the same cascade may, however, show structures, such as thresholds and edges, that can provide information about the mass spectrum of the new model.

In the case under study, once the Higgs has been discovered, extensive high-luminosity analyses can be performed in order to reconstruct the full decay chains of SUSY particles contributing to its production. In particular, the Higgs is mainly produced through the cascade:

$$\tilde{q}_L \rightarrow \tilde{\chi}_2^0 q \rightarrow \tilde{\chi}_1^0 h q. \tag{6.5}$$

As a consequence of two-body kinematics, the invariant mass of the Higgs-quark system shows both a threshold and an edge value, related to different combinations of the

masses of the SUSY particles involved:

$$M^2_{hq,\text{threshold}} = \frac{m^2_{\tilde{q}_L} - m^2_{\tilde{\chi}^0_2}}{2m^2_{\tilde{\chi}^0_2}} \left[m^2_{\tilde{\chi}^0_2} + m^2_h - m^2_{\tilde{\chi}^0_1} - \sqrt{\delta} \right] + m^2_h, \tag{6.6}$$

$$M^2_{hq,\text{edge}} = \frac{m^2_{\tilde{q}_L} - m^2_{\tilde{\chi}^0_2}}{2m^2_{\tilde{\chi}^0_2}} \left[m^2_{\tilde{\chi}^0_2} + m^2_h - m^2_{\tilde{\chi}^0_1} + \sqrt{\delta} \right] + m^2_h, \tag{6.7}$$

$$\delta = (m^2_{\tilde{\chi}^0_2} - m^2_h - m^2_{\tilde{\chi}^0_1})^2 - 4m^2_h m^2_{\tilde{\chi}^0_1}. \tag{6.8}$$

The events passing the selection cuts listed in the previous section, including the mass window cut, are also required to have at least one b-jet with $p_T > 100$ GeV. Furthermore, a veto is imposed on additional b-tagged jets with $p_T > 50$ GeV. This will result in fewer signal events, but also in a reduced background contamination, as reported in Table 6.2. The advantage is understandable, since we are no longer interested in reaching the maximal significance, but rather in having a clear distribution shape.

Point 1	Signal	Comb BG	Susy BG
Cut 1-4 and ±25 GeV mass window	5306	1828	2008
At least one b-jet with $p_T > 100$ GeV	4023	935	1432
No additional b-jets with $p_T > 50$ GeV	3319	390	1159

Point 2	Signal	Comb BG	Susy BG
Cut 1-4 and ±25 GeV mass window	3298	2339	2908
At least one b-jet with $p_T > 100$ GeV	2508	1349	2149
No additional b-jets with $p_T > 50$ GeV	1766	452	1666

Standard Model	$t\bar{t}$	Z	W	$b\bar{b}$
Cut 1-4 and ±25 GeV mass window	1364	55	32	37
At least one b-jet with $p_T > 100$ GeV	775	45	16	21
No additional b-jets with $p_T > 50$ GeV	662	33	16	19

Table 6.2: Summary of the number of expected SUSY and SM events after the application of different selection cuts, for 300 fb^{-1} of integrated luminosity.

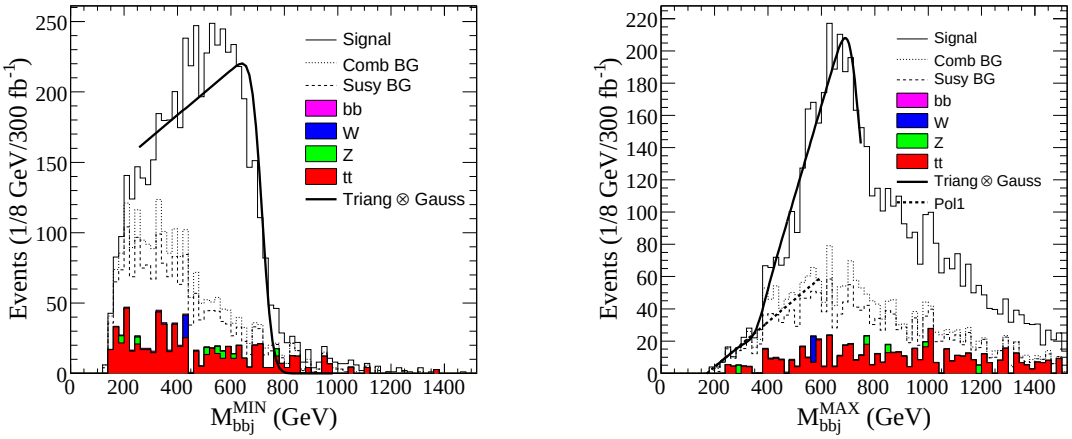

Figure 6.7: Invariant mass of the Higgs plus jet system for Point 1. In the left (right) plot the jet minimising (maximising) M_{hq} has been used.

Since SUSY events are rich in hard jets, the choice for the right jet to associate with the Higgs is not obvious. Anyway, it is expected to be one of the two most energetic jets, because it comes from the decay of a heavy squark. The other is the one coming from the squark or gluino that generates the second cascade. The strategy is the following. The two jets with the highest p_T are identified and two different M_{hq} distributions are reconstructed, respectively with the jet minimising and maximising the M_{hq} value.

Since the background events will tend to concentrate toward low mass values, the distribution obtained using the jet minimising M_{hq} will be used to determine the mass upper limit $M_{hq,\mathrm{edge}}$. The $M_{hq,\mathrm{threshold}}$ value will be determined from the other mass plot.

Figures 6.7 and 6.8 show the two mass plots for both benchmarks.

The two mass edge values can be obtained by fitting a convolution of a triangular shape and a Gaussian. The statistical uncertainty is the error on the fitted parameter, while the systematic error comes from the parameter dependence on the fitting boundaries. An additional 1% systematic error is expected on the jet energy scale (JES) [68].

The mass threshold evaluation is more challenging. For Point 1 a straight-line fit provides a satisfactory model of the background events in the 200-400 GeV mass range.

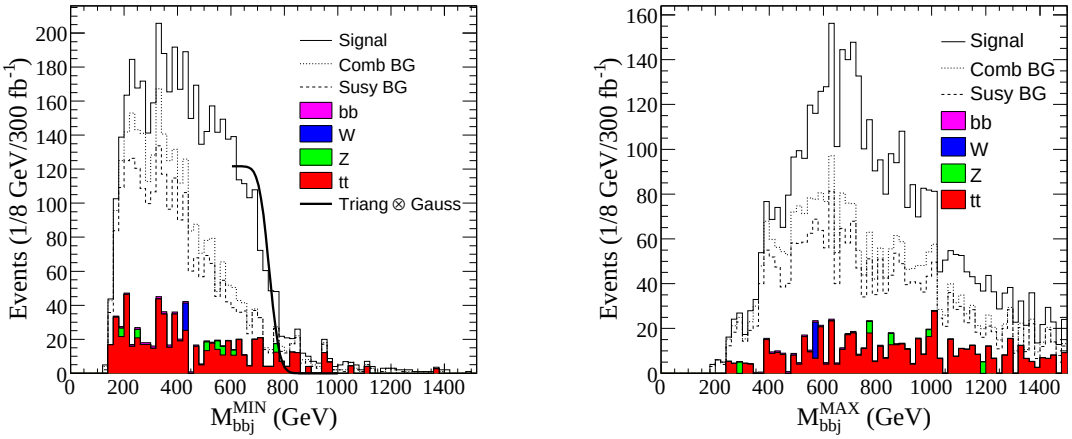

Figure 6.8: Invariant mass of the Higgs plus jet system for Point 2. In the left (right) plot the jet minimising (maximising) M_{hq} has been used.

		Measured (GeV)	True (GeV)
Point 1	$M_{hq,\text{edge}}$	721 ± 3 (stat) ± 5 (syst) ± 7 (JES)	732
Point 1	$M_{hq,\text{threshold}}$	374 ± 15 (stat) ± 10 (syst) ± 4 (JES)	410
Point 2	$M_{hq,\text{edge}}$	749 ± 5 (stat) ± 5 (syst) ± 7 (JES)	762
Point 2	$M_{hq,\text{threshold}}$	–	435

Table 6.3: Measured and true values of M_{hq} edge and threshold for Points 1 and 2, after 300 fb^{-1} of integrated luminosity.

For the other benchmark point the mass distribution is too confused to fit.

All the measurements are summarized in Table 6.3. It can be noticed that all the central values show a shift of at least 10 GeV toward low masses. This can be explained by a b-jet energy scale underestimate in the simulation: no corrections are applied to recover the fraction of energy carried by the neutrino coming from semi-leptonic bottom hadron decay.

6.6 Di-leptonic signatures

We can also look for mass edges in other mass distributions. The cleaner, thus more powerful, typology is the two lepton plus missing energy signature. Unfortunately, as pointed out in Section 6.1, the di-lepton decay of the $\tilde{\chi}_2^0$ must be kinematically forbidden in order for Higgs production to be significant, so the resulting mass distribution does not exhibit any evidence for edges or thresholds, but only the peak of resonant Z production. No mass spectrum information can be directly extracted.

In principle, endpoints can be found in the M_{Zq} distribution, as we have done in the previous section adding the four-momenta of the Higgs boson and a jet. But while the Higgs is produced almost exclusively by the $\tilde{\chi}_2^0$, the Z comes, more or less in equal parts, from the decay of $\tilde{\chi}_2^0$, $\tilde{\chi}_3^0$ and $\tilde{\chi}_2^\pm$, giving rise to three different mass distributions. The isolation of one chain is technically difficult and the resulting number of events would be statistically limited.

We do have some indirect clues. Qualitatively, for example, we can say that, assuming mSUGRA, the $\tilde{\chi}_2^0$ to $\tilde{\chi}_1^0$ splitting must be smaller than the slepton mass but larger than m_Z. More generally, cascades like $A \to B^{(*)}\ell^\mp \to C\ell^\pm\ell^\mp$ must be suppressed with respect to cascades containing a $Z \to \ell^+\ell^-$. Moreover, Z and light Higgs productions can also be compared. A measurement of the ratio of their cross-sections in SUSY cascades constrains the Higgs and Z couplings to neutralinos and thus constrains the gaugino-higgsino mixing in neutralino mass eigenstates. These observations help to restrict the range of possible models.

In order to give an estimate of the ratio of Z and h production, a di-lepton and a di-b-jet sample must be isolated by identical sets of selection cuts, provided that b's are replaced with leptons:

1. $E_T^{\text{miss}} > 300$ GeV;

2. two light-flavoured jets with $p_T > 100$ GeV;

3. two leptons (e or μ) or two b-jets with $p_T > 25$ GeV.

With respect to the cuts of the previous sections, the transverse momentum threshold for leptons and b's is softer. This is because the daughters of Z and h have, in general,

different p_T spectra. Thus, the threshold must be kept as low as possible in order to reduce the bias that favours the most massive particle.

In addition, the two leptons are required to be of the opposite sign and same flavour. Between the selected pairs of leptons, some are not flavour-connected, for example when they come from separate cascades; this is also the case of the SM $t\bar{t}$ events. These pairs of leptons constitute a smooth continuum background. To get rid of it, a parallel set of cuts can be applied, keeping only the opposite-sign and opposite-flavour pairs. They will have the same distribution as the uncorrelated same flavour pairs. Thus, after subtracting the two obtained histograms, the remaining distribution will represent a pure flavour-connected lepton sample, containing the signal we are looking for. The di-leptonic invariant masses before and after opposite-flavour subtraction are shown in Figure 6.9 for both mSUGRA points studied.

A limit on di-lepton production other than via Z decay can be set by integrating the number of events in the opposite-flavour-subtracted mass histogram over the mass range 0 to 85 GeV, $N_{\ell^+\ell^-}$, and dividing by N_Z, the number of entries under the Z resonance.

The resulting ratio is statistically compatible with zero for Points 1 and 2:

$$\frac{N_{\ell^+\ell^-}}{N_Z} = \frac{N^{SF}_{\ell^+\ell^-} - N^{OF}_{\ell^+\ell^-}}{N^{SF}_Z - N^{OF}_Z} = \frac{3826 - 3745}{1222 - 413} \pm \sigma_{\text{stat}} = 0.10 \pm 0.11,$$

$$\frac{N_{\ell^+\ell^-}}{N_Z} = \frac{N^{SF}_{\ell^+\ell^-} - N^{OF}_{\ell^+\ell^-}}{N^{SF}_Z - N^{OF}_Z} = \frac{4410 - 4531}{1522 - 546} \pm \sigma_{\text{stat}} = -0.12 \pm 0.10.$$

The main systematic uncertainty comes from the kinematic cuts on the leptons. It is estimated by varying the p_T cut from 25 GeV to 20 GeV and 30 GeV, the resulting differences being set to a one sigma discrepancy. This source contributes an additional 10% uncertainty on the central value of the ratio. The resulting upper bounds at 95% of confidence level are given by 1.65 times the total uncertainty, that is

$$\frac{\sigma((\text{Any}) \to \ell^+\ell^-)}{\sigma(Z \to \ell^+\ell^-)} < \frac{N_{\ell^+\ell^-}}{N_Z} + 1.65\sigma = 0.10 + 1.65(0.11\ (\text{stat}) \oplus 0.01\ (\text{syst})) = 0.29$$

for Point 1 and

$$\frac{\sigma((\text{Any}) \to \ell^+\ell^-)}{\sigma(Z \to \ell^+\ell^-)} < \frac{N_{\ell^+\ell^-}}{N_Z} + 1.65\sigma = -0.12 + 1.65(0.10\ (\text{stat}) \oplus 0.01\ (\text{syst})) = 0.05$$

for Point 2.

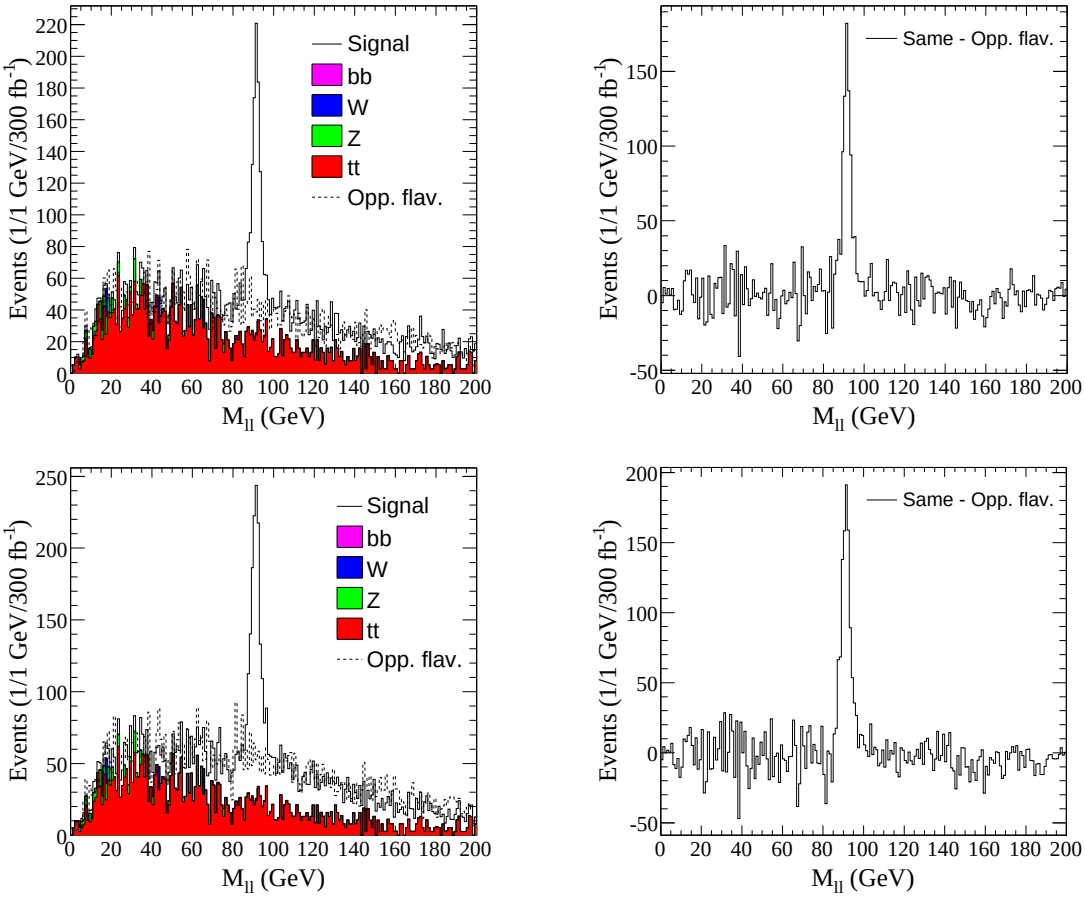

Figure 6.9: Di-leptonic invariant masses before (left) and after (right) opposite flavour subtraction. The two top plots correspond to Point 1, the bottom two to Point 2.

The measurement of the ratio of h to Z production rates is more difficult. The following differences must be taken into account:

- different reconstruction efficiency and mass resolutions;
- presence of important, non-negligible combinatorial background in $h \to b\bar{b}$ analysis.

The first item is not really a problem, because the detector efficiencies and resolutions will be well known after 300 fb^{-1} of collected data, as supposed here; nevertheless a 5% uncertainty on the b-tagging efficiency has to be considered as a systematic effect

[100, 101]. The second point is the real difficulty. While very few Z events will be lost because of combinatorial background, the fraction of such events lost for the h case is extremely high and cannot be estimated. So, we are obliged to set only a lower limit at 95% of confidence level. For benchmark Points 1 and 2, these are:

$$\begin{aligned}\frac{\sigma(h \to b\bar{b})}{\sigma(Z \to \ell^+\ell^-)} &> \frac{N_h}{N_Z}\frac{\epsilon_\ell^2}{\epsilon_b^2} - 1.65\sigma = \\ &= \frac{9931}{1222-431}\frac{1}{0.36} - 1.65(2.0\ (\text{stat}) \oplus 1.7\ (\text{syst}) \oplus 3.4\ (\text{b-tag})) = 28,\end{aligned}$$

$$\begin{aligned}\frac{\sigma(h \to b\bar{b})}{\sigma(Z \to \ell^+\ell^-)} &> \frac{N_h}{N_Z}\frac{\epsilon_\ell^2}{\epsilon_b^2} - 1.65\sigma = \\ &= \frac{5566}{1522-546}\frac{1}{0.36} - 1.65(1.0\ (\text{stat}) \oplus 0.8\ (\text{syst}) \oplus 1.6\ (\text{b-tag})) = 13.\end{aligned}$$

The efficiencies for lepton and b identification are marked as ϵ_ℓ and ϵ_b. The statistical errors will be of order 6%. Two more systematic effects have to be taken into account. The kinematic cut uncertainty is estimated as in the previous case by varying by 5 GeV the p_T cut on leptons and b-jets, giving an error of order 5%. In addition, the different topologies of Z and h events may also generate a difference in the trigger efficiency. Fortunately, a unique trigger menu based on jet and missing energy signatures will accommodate both type of events, resulting in an efficiency difference of order less than 0.5%. More details on how we determine this error are reported in Section 6.8.3. The two lower limits can be compared with the true values of $\sigma(h \to b\bar{b})/\sigma(Z \to \ell^+\ell^-) = 40$ for Point 1 and $\sigma(h \to b\bar{b})/\sigma(Z \to \ell^+\ell^-) = 28$ for Point 2.

6.7 Searches for $h \to \gamma\gamma$ signature

Due to its very large branching ratio, the $b\bar{b}$ decay is not only the most promising Higgs discovery channel in these scenarios, but it is also the only statistically accessible channel for the additional measurements of the SUSY mass spectrum. We have already shown, however, that it is affected by a very large background coming from the copious production of b-quarks during the cascades.

In this section, we explore the possibility of observing other decay modes. In descending order of branching probability we find $c\bar{c}$, $\tau^+\tau^-$, gg and $\gamma\gamma$. The $c\bar{c}$ and gg are

excluded because they are indistinguishable from light jets and thus it would be impossible to recognize the two jets coming from the Higgs from the rest of the hadronic activity of the event. Instead, τ-jets can be tagged by the ATLAS detector, but, on the other hand, a fraction of the τ energy is given to a neutrino and irremediably lost, so the resonance peak cannot be reconstructed. The remaining $\gamma\gamma$ suffers from a very poor branching ratio.

Despite this, the $\gamma\gamma$ channel has very low background. Indeed, very few hard photons are emitted either in SUSY events or in Standard Model processes with genuine missing energy.

In order not to lose the few signal events, very loose cuts are needed:

1. $E_T^{\text{miss}} > 100$ GeV;
2. two hard jets with $p_T > 100$ GeV;
3. two photons with $p_T > 20$ GeV.

The invariant mass distribution of the two reconstructed photons for the selected events is shown in Figure 6.10, assuming an integrated luminosity of 30 fb^{-1}. Due to the small number of expected events, reported for signal and background in Table 6.4, the signal significance is estimated using the Poisson statistics and it is about 3.5. A 5σ discovery would be possible after about 70 fb^{-1}.

	Point 1	Point 2	$t\bar{t}$	Z	W	QCD	$\gamma\gamma$	γ+jet
Cut 1, 2, 3	11	10	94	13	46	14	0	0
± 2 GeV mass window	10	8	1.9	0.1	0.6	0.1	0	0

Table 6.4: Summary of the number of expected SUSY and SM events after the application of different selection cuts, for 30 fb^{-1} of integrated luminosity.

6.8 Full simulation studies

This section is mainly devoted to validate and confirm the fast-simulation results discussed in the previous sections.

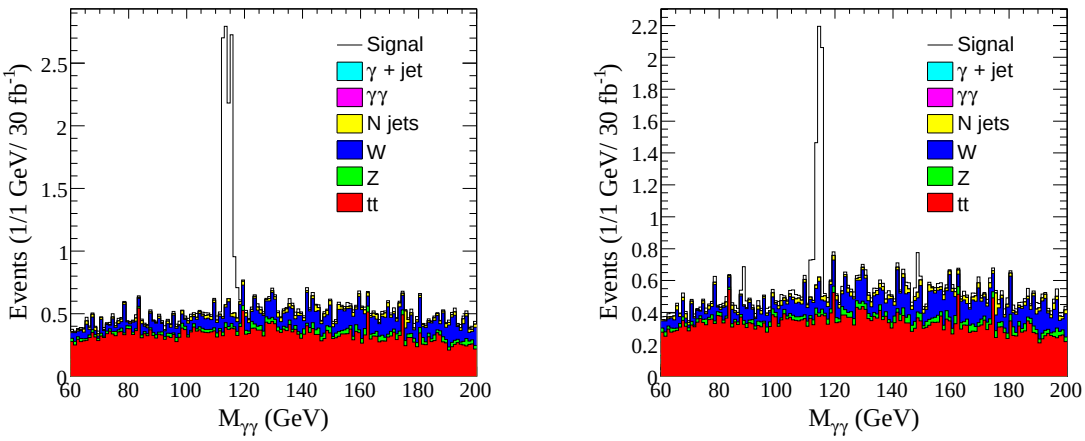

Figure 6.10: Two photon invariant mass distribution for events passing the selection cuts listed in Section 6.7 of the text. Left: Point 1. Right: Point 2.

In a first step, we compare with the two techniques the detector performances in reconstructing the b-jets and the missing transverse energy, the two main signatures in the analysis. Then, the $h \to b\bar{b}$ analysis is entirely repeated using fully simulated SUSY and SM events.

Finally, since the trigger system is not present in fast simulations, we consider the trigger signatures relevant for the physics channel under examination and we will argue whether their foreseen performances provide the required signal efficiency.

6.8.1 Detector simulation comparison

Figure 6.11 shows a comparison between fast and full ATLAS simulation performances. The left plot compares the reconstruction and tagging efficiency of b-parton initiated jets as a function of their pseudorapidity. The b-tagging parametrization in fast-simulation is satisfactory, while small differences occur for jet reconstruction in the central detector region. Further investigations reveal that such inefficiency affects mainly high-p_T b-jets, i.e. with $p_T \gtrsim 100$ GeV. An additional check confirms that the fast-simulated b-pair invariant mass resolution, which is found to be 20 GeV, agrees with the fully simulated reconstruction. The right plot shows the reconstructed missing energy resolution along a transverse axis. The root mean square changes from 20 to 25

GeV switching from fast to full detector description. The difference is due to the fact that no calorimeter crack regions are simulated in the fast simulation. However, since for the present analysis we require $E_T^{\text{miss}} > 300$ GeV, such slight degradation should not affect our results.

The sample used for these comparisons is the mSUGRA Point 1 defined in Section 6.3.

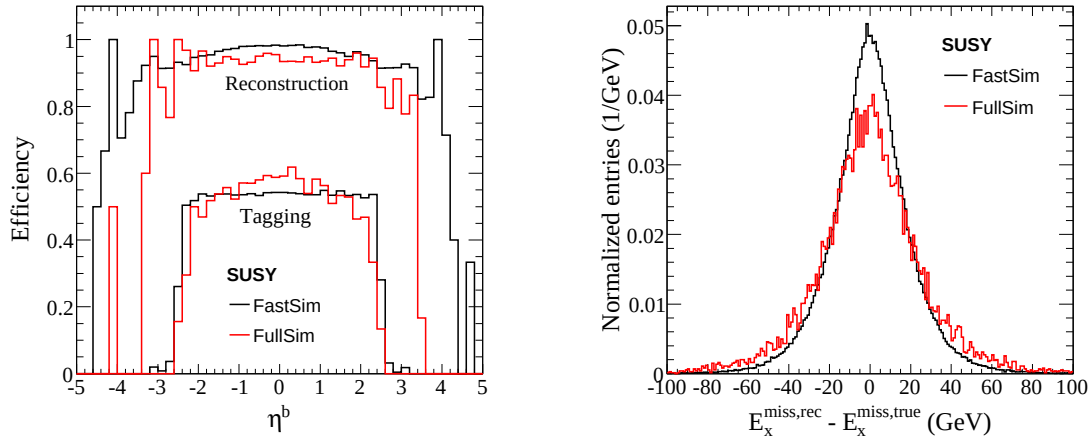

Figure 6.11: Comparison between fast (black) and full (red) ATLAS simulation performances: (left) reconstruction and tagging efficiency of b-jets as a function of η; (right) reconstructed missing energy resolution along the x axis. The sample used is the mSUGRA Point 1 defined in Section 6.3.

6.8.2 Reconstruction of $h \to b\bar{b}$ signal

The analysis scheme illustrated in Section 6.4 and 6.5 is applied to sets of fully simulated signal and background samples, each consisting of a number of events equivalent to an integrated luminosity comprised between 5 and 10 fb^{-1}. The final distributions are then rescaled to obtain predictions for 10 fb^{-1} of collected data. The signal events are generated in the scenario of the mSUGRA benchmark Point 1.

The resulting invariant mass plots for the two b-quark system and the Higgs-quark system are shown in Figure 6.12. Table 6.5 summarizes the expected SUSY and SM events contributing to the M_{bb} distribution.

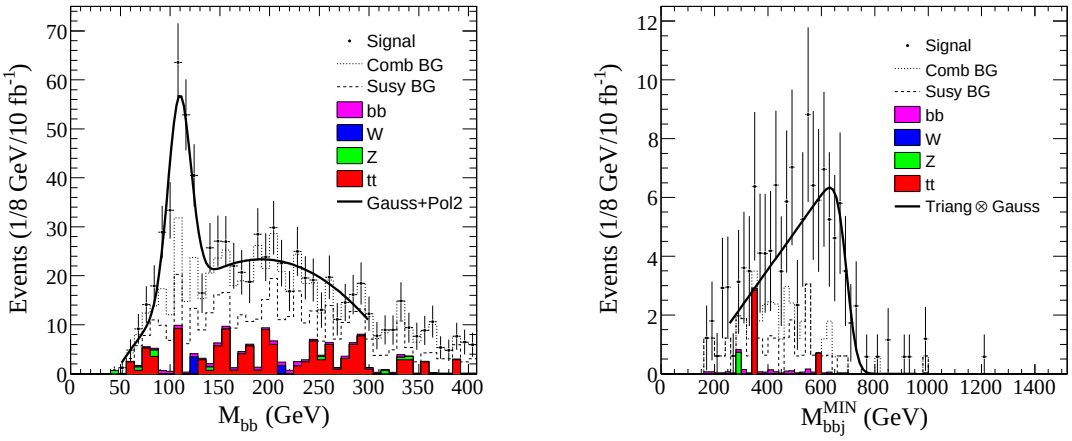

Figure 6.12: Invariant mass of the selected b-jet pairs (left) and invariant mass of the system Higgs plus the jet minimising m_{hq} (right) after 10 fb^{-1} of integrated luminosity. The selection cuts are listed in Sections 6.4 and 6.5.

Point 1	Signal	Comb BG	Susy BG
No cuts		7700	15300
Cut 1, 2, 3	248	659	633
Cut 4	160	313	302
±25 GeV mass window	125	53	53

Standard Model	$t\bar{t}$	Z	W	$b\bar{b}$
Cut 1, 2, 3	525	12	22	43
Cut 4	281	8	10	21
±25 GeV mass window	23	2	4	4

Table 6.5: Summary of the number of expected SUSY and Standard Model events after the application of the different selection cuts, listed in Section 6.4, for 10 fb^{-1} of integrated luminosity.

As it can be seen, the Higgs discovery significance is confirmed to be above 10, consistent with the evaluation with the fast-simulation method.

However, few differences should be remarked. The signal, the combinatorial and SUSY backgrounds and the $t\bar{t}$ background are reduced by about 10% with respect to the fast-simulation expectations. We believe that the explanation for this deficiency is the previously shown drop in the b-jet reconstruction efficiency at high transverse momenta. Such b-jets are, indeed, more likely to contain energetic leptons, coming from semi-leptonic decay of heavy-flavoured hadrons. The lepton identification criteria have been decided in common with all the ATLAS SUSY analyses and are defined to be loose, in order to maximize the electron and muon reconstruction. Such selection, however, causes a high rate of b-jet misidentification with leptons and is not optimal for the present analysis. A tighter lepton selection might be more favourable for $h \to b\bar{b}$ searches. A second difference is the increase in the QCD $b\bar{b}$. For this sample, the effect of b-jet losses is overwhelmed by the enhanced quantity of fake $E_T^{\rm miss}$, due to the more accurate description of the calorimeter inefficiencies.

A particularly interesting result is the possibility to measure the value of $M_{hq,\rm edge}$ even with low-luminosity running. Nevertheless, the uncertainties should be revised. The statistic error obviously increases to about 15 GeV. Moreover, a jet energy scale uncertainty of 1% can be too optimistic for this case; its value should be, however, below the level of 5%. The resulting measurement is

$$m_{hq,\rm edge} = 695 \pm 15\ (\rm stat) \pm 5\ (\rm syst) \pm 35\ (\rm JES),$$

to be compared with the true value of 732 GeV.

6.8.3 Trigger issues

In ATLAS, SUSY events are triggered by electromagnetic clusters in the calorimeter, isolated tracks in the muon spectrometer or by high energy jets and missing energy signatures. The former has been extensively studied and will probably be the main trigger for the $h \to \gamma\gamma$ studies of Section 6.7. For SM Higgs to two photon events it has been shown that it is 98% efficient at first level trigger and 94% efficient after the event filter [102]. Instead, the $h \to b\bar{b}$ analysis is expected to be triggered by jets and $E_T^{\rm miss}$. Here, we want to give a preliminary estimate of the efficiency of such trigger

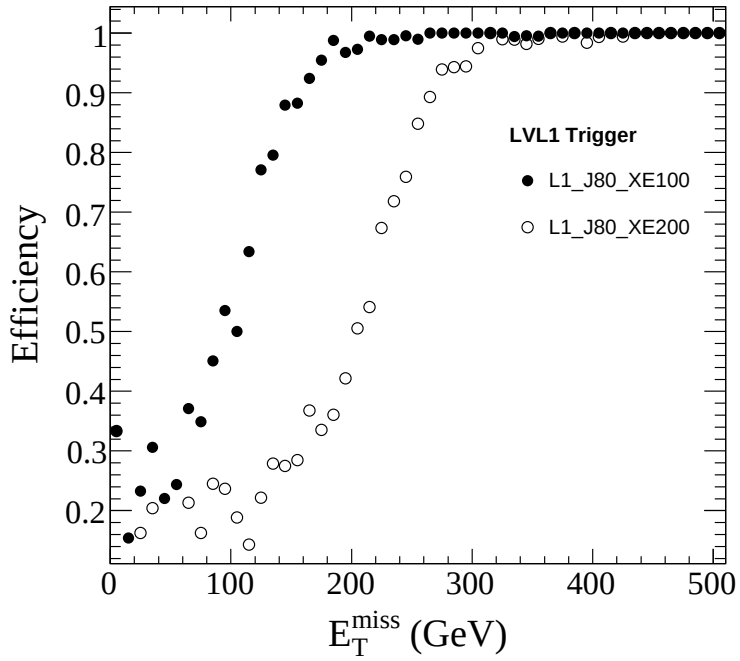

Figure 6.13: First level *L1_J80_XE100* and *L1_J80_XE200* trigger menu efficiencies for mSUGRA Point 1 events.

signatures.

According to the ATLAS High Level Trigger Technical Design Report [75], the trigger menus for high luminosity 2×10^{33} cm^{-2} s^{-1} running will include a one jet plus E_T^{miss} trigger with thresholds set to about 70 GeV of transverse energy for both. The corresponding first level trigger has thresholds lowered to $\sim$ 30 GeV (Table 4.1).

At present, the ATLAS trigger full simulation for high-luminosity running has not been finalized (ATLAS software `Athena 12`). Only the first level decision menus are accessible for E_T^{miss} signatures and their E_T thresholds are higher than for the expected final version:

- *L1_J80_XE100*: $E_T^{\text{jet}} > 80$ GeV and $E_T^{\text{miss}} > 100$ GeV;
- *L1_J80_XE200*: $E_T^{\text{jet}} > 80$ GeV and $E_T^{\text{miss}} > 200$ GeV.

In Figure 6.13 the trigger efficiency of mSUGRA Point 1 events preselected with two jets of $p_T > 100$ GeV is plotted against the offline reconstructed missing transverse

energy for both menus. At the nominal E_T^{miss} values, the efficiency is about 40% for both signatures and the turn-on curves grow up very slowly before reaching to the full 100% efficiency. However, in the region interesting for the $h \to b\bar{b}$ analysis, i.e. for events with $E_T^{\text{miss}} > 300$ GeV, the overall trigger efficiency is more than 99.5% for both *L1_J80_XE100* and *L1_J80_XE200*.

This trigger analysis is also used to estimate the systematic uncertainty on the trigger efficiency difference between $h \to b\bar{b}$ and $Z \to \ell^+\ell^-$ event selections, which affects the measurement of the production ratio of the Higgs and Z bosons (Section 6.6). The first level trigger algorithms are run on events passing the two sets of selection cuts and the resulting efficiencies differ by less than 0.5%.

7

EXTRAPOLATION OF SUSY PARAMETERS

7.1 Global fits of LHC measurements

Physics beyond the Standard Model is expected to appear at the TeV energy scale. Its presence is well motivated by both experimental and theoretical hints, already discussed in Section 1.5. Among the main goals of the LHC experiments is, of course, to find evidence of such new physics. If this happens, particular attention will be turned to determine, or at least constrain, the nature of the underlying theory of the observed phenomena.

However, new physics scenarios are described in terms of some newly introduced parameters, still unknown and typically only weakly constrained by present measurements. For many of the proposed models, such free parameters amount to a large number. Moreover, the processes predicted to be visible at the LHC often have complex signatures. For instance, R-parity conserving supersymmetry does not predict any new clear resonance, but rather a variety of different decay cascades of superparticles. The characteristics of each cascade, i.e. its production rate and the shape of the invariant mass distributions of the final states arising from it, depend on the free parameters of the model. For all these reasons, the exclusion of possible interpretations of the LHC signatures or the extraction of the model parameters that best describe data might be rather complicate tasks.

Besides the LHC measurements, the model of new physics should also agree with

many low-energy measurements, such as the anomalous magnetic moment of the muon, and be allowed by the present experimental limits from flavour physics (see Section 1.3). Ultimately, if a particular theory is believed to provide a solution of the existence of cosmological dark matter, the predicted relic density of the dark matter candidate must match cosmological observations. This severely restricts the mass and coupling not only of the candidate itself, but also of the other particles involved in the annihilation processes occurring between the dark matter particles in the early universe.

A general approach is to combine all the measured quantities and construct a likelihood map in the full parameter space for a given model, where the likelihood function is intended to gauge the agreement between data and predictions. The best-fitting point corresponds to the set of parameters with highest likelihood value. Secondary local maxima can eventually exist. Models giving poor fit results for any set of parameters can be excluded.

The purpose of this chapter is to apply this approach to the specific SUSY scenarios with copious production of light Higgs bosons analysed in Chapter 6. Starting from the measured quantities and the appropriate uncertainties for the benchmark Points 1 and 2, we extract the compatible regions of the Minimal SUGRA space. The intention is to prove the validity of the method and, at the same time, to illustrate a sample treatment to adopt when real LHC data will be available.

The restriction to mSUGRA is forced by the small amount of signatures detectable in the considered scenarios. Nevertheless, if new physics is observed at the TeV scale, the reconstruction of the underlying theory should not be biased by high-scale assumptions, like SUSY breaking mechanisms. Therefore, when possible, the analysis has to be performed in a completely low-scale framework. Unfortunately, with the few constrains derived in our benchmark points, a fit in the 20-dimensional MSSM space is not realistic. Previous studies have shown that such a high-dimensional problem can be solved in SUSY points with a phenomenology more favourable for LHC [103]. For less promising cases, comprising the one under investigation, a future international e^+e^- linear collider (ILC) could provide the complementary measurements needed for a complete MSSM analysis [104].

The structure of the chapter is as follows. In the next section we briefly present the `SFitter` tool, used to construct the likelihood maps. We then describe the statistical

technique employed; we report the form of the likelihood functions, the procedure for the extraction of confidence intervals on the unknown parameters and the definition of excluded models. Our scan of the mSUGRA parameter space is based on a Markov-chain Monte Carlo technique, which we recall in Section 7.4. Finally, in Sections 7.5 and 7.6, we report the results for the benchmark Points 1 and 2.

7.2 The SFitter tool

The SFitter tool [105, 106, 103] is designed to map large samples of measurements onto high-dimensional parameter spaces. The strategy adopted is completely general: model parameters as well as measurements are input to the tool as external files, independent of the main code. For a given set of parameters, SFitter collects the theoretical predictions, compares them to the corresponding measurements and calculates the value of the likelihood function. The operation is reiterated over the parameter space by specific algorithms, included in SFitter, in charge of finding the best-fitting points.

We briefly summarize here the chosen SFitter setup at each of the mentioned steps, i.e. prediction calculations, likelihood function definition and fitting algorithm.

SFitter uses the conventions of the Les Houches accord [107, 108] to interface to different programs which return the theoretical predictions. For the present analysis the renormalization group code Isajet 7.74 [90] is used to obtain the supersymmetric particle masses at the electroweak energy scale as well as their decay modes and branching ratios; the next-to-leading order cross-sections for sparticle production at hadron colliders are computed by Prospino 2 [109, 110, 111, 112]; the relic density of the lightest supersymmetric particle, regarded as the dark matter candidate, is evaluated by MicrOMEGAs 2.0 [97, 98, 99]. In addition, since for the new physics scenarios under consideration we are interested in the production rate of the Higgs and Z bosons, we implement a new tool, intended to reconstruct all the possible decay chains from which a particle originates. Starting from the desired final particle X, its mothers are searched for in a list of the open decay channels. The total production cross-section for X is then

$$\sigma(X) = \sigma(pp \to X) + \sum_{M=\text{mothers}} \sigma(M) \times BR(M \to X). \tag{7.1}$$

The first term is retrieved from `Prospino 2`, while, for each mother M, $\sigma(M)$ is computed by a recursive call to the main algorithm, which will search for decays with a particle M in the final state and compute Equation 7.1 for $X = M$. The recursion proceeds until a particle has no mothers and its total cross-section is equal to the direct production cross-section in proton interactions. The production rate of the desired particle is then fully determined.

Many definitions of the likelihood function are available depending on the type of measurement and its error. Both central values with double-sided error bands and upper and lower limits are correctly handled by `SFitter`. Proper treatments for statistical, systematic and theoretical uncertainties are included. Moreover, the determination of the likelihood takes into account a general correlation matrix between measurements. The prescriptions adopted in this chapter are detailed in the next section.

The fitting procedure can be realized either through the maximization of the likelihood function, by the algorithms in the `Minuit` package [113], or through a mapping of the parameter space. In this second case, the likelihood can be evaluated at the crossing points of a multi-dimensional grid with fixed step size or in a subset of points selected with a Markov-chain Monte Carlo method. Due to the large number of parameters involved in our analysis, a fixed-step grid scan is prohibitive. Therefore, we opted for a Markov-chain Monte Carlo, that behaves much more efficiently, as described in Section 7.4. The results are cross-checked by a maximization algorithm based on the calculation of the gradient of the likelihood function (`Migrad`).

7.3 Statistical approach

We consider a problem involving a set of N measured quantities denoted by $x = (x_1, \ldots, x_N)$. The corresponding theoretical predictions $\bar{x} = (\bar{x}_1, \ldots, \bar{x}_N)$ are functions of a set of n parameters, called $\theta = (\theta_1, \ldots, \theta_n)$, whose values are unknown.

We are interested in three different goals:

- to determine the values of the parameters θ that best describe the measurements x;
- to define intervals around the parameter best values, which reflect the statistical precision of the measurements;

- to quantify the global agreement between data and the theory under test.

The statistical approach to achieve these goals relies on the likelihood function. The dissertation in this section refers mainly to [28, 114, 115].

7.3.1 Likelihood function

The likelihood function describes the agreement between the data obtained in the experiment, x, and the predicted value, $\bar{x}$, assuming the validity of the underlying theory.

For the i^{th} Gaussian measurement with standard deviation σ_i, the likelihood is

$$\mathscr{L}_i = \exp\left[-\frac{1}{2}\left(\frac{x_i - \bar{x}_i}{\sigma_i}\right)^2\right]. \tag{7.2}$$

Completely independent measurements are combined by simple multiplication of the single likelihoods. However, the measurements we are dealing with are affected by the same systematic uncertainties on the electromagnetic (LES) and hadronic energy scales (JES). Therefore, the likelihood generalizes to

$$\mathscr{L} = \prod_{i,j} \exp\left[-\frac{1}{2}\left(\chi_i C_{ij}^{-1} \chi_j\right)\right], \tag{7.3}$$

where $\chi_i = (x_i - \bar{x}_i)/\sigma_i$ and C^{-1} is the inverse of the correlation matrix:

$$C_{ii} = 1 \qquad C_{ij} = 2\frac{\sigma_{\text{LES},i}\sigma_{\text{LES},j} + \sigma_{\text{JES},i}\sigma_{\text{JES},j}}{\sigma_i^2 + \sigma_j^2} \qquad (i \neq j). \tag{7.4}$$

The variance σ_i^2 has been decomposed in three contributions, $\sigma_{\text{LES},i}^2$ and $\sigma_{\text{JES},i}^2$ being the energy scale systematics, which are fully correlated between two measurements, and the remaining comprising the statistical error and the uncorrelated systematic errors.

Experimental upper and lower limits are included in the likelihood by the further factors

$$\mathscr{L}_k^{\text{limit}} = \begin{cases} 1 & \text{for } \bar{x}_k \text{ inside the confidence interval} \\ \exp\left[-\text{erfi}^2(\text{CL})\right] & \text{for } \bar{x}_k \text{ outside the confidence interval,} \end{cases} \tag{7.5}$$

where erfi is the inverse of the error function and CL is the confidence level of the measurement. With such convention an experimental bound incompatible at 95% CL

with the model has the same likelihood value as a Gaussian measurement 1.96σ away from the prediction.

We will refer to the complete likelihood as

$$\mathscr{L}(\theta) = \prod_{i,j} \exp\left[-\frac{1}{2}\left(\chi_i C_{ij}^{-1} \chi_j\right)\right] \prod_k \mathscr{L}_k^{\text{limit}} \tag{7.6}$$

and denote $\chi^2(\theta) = -2\ln(\mathscr{L}(\theta))$. Note that $\mathscr{L}(\theta)$ is viewed as a function of the parameters, but is not a probability function for the parameters.

The values of the parameters that best describe data are taken to be those maximizing $\mathscr{L}(\theta)$.

7.3.2 Confidence intervals

The parameter estimates, extracted by maximization of the likelihood, should be accompanied by a region, constructed to have a well defined probabilistic interpretation.

We follow the construction of confidence intervals due to Neyman [116], with the subsequent interpretation. Suppose we repeat an experiment a large number of times. The intervals, constructed for every experiment following this procedure, will include the true value of the parameters with a probability equal or greater than the specified confidence level (CL).

In the simplest case of purely Gaussian measurements that are estimators for the parameters θ, i.e. $\bar{x} = \theta$, the $\chi^2(\theta)$ distribution is parabola-shaped and the confidence region is determined by the contours of constant χ^2 around the minimum:

$$\chi^2(\theta) \leq \chi^2_{\text{min}} + \Delta\chi^2. \tag{7.7}$$

In particular, for χ^2 depending on a single parameter, a 68% confidence level corresponds to $\Delta\chi^2 = 1$.

7.3.3 Probing new physics

To assess the validity of a given model we have to quantify how well theory describes the actual data. This information is contained in χ^2_{min}, which is a test statistic of the best possible agreement between data and the model under assumption.

The $\chi^2_{\rm min}$ can be turned into a so-called p-value through the expression

$$p = \int_{\chi^2_{\rm min}}^{\infty} f(\chi^2, N_{\rm dof}) d\chi^2, \tag{7.8}$$

where f is the χ^2 probability density function:

$$f(\chi^2, N_{\rm dof}) = \frac{e^{-\chi^2/2}(\chi^2)^{N_{\rm dof}/2-1}}{\sqrt{2^{N_{\rm dof}}}\Gamma(N_{\rm dof}/2)}. \tag{7.9}$$

The number of degrees of freedom, $N_{\rm dof}$, is equal to the number of experimental constrains minus the number of free parameters.

It is worth remarking that the p-value is not the probability for the hypothesis to be true. Rather, the p-value is the probability of obtaining data at least as incompatible with the hypothesis as the data actually observed, under the assumption of the hypothesis.

7.4 Markov-chain Monte Carlo methods

Markov-chain Monte Carlo (MCMC) methods are a class of algorithms that construct a sequence of points (a Markov chain) in a n-dimensional space based on their probability distribution. For fits of LHC measurements, the probability distribution is the likelihood viewed as function of the parameters $\mathscr{L}(\theta)$. The points contained in the resulting Markov chain are representative of the likelihood, being more dense in regions with higher probability, and can be used as a sample of the explored space. The quality of the sample improves as function of the number of extracted points.

With respect to a standard fixed-step grid method, the MCMC allows a more efficient way to scan a high-dimensional parameter space. Indeed, MCMC's provide:

- a finer resolution of the likelihood function around local maxima;
- a better capability of revealing local maximum regions, given that the number of extracted points is sufficiently high.

On the other hand, the absolute value of the $\chi^2_{\rm min}$ is more precisely evaluated by a maximization algorithm than by a MCMC method. However, the result of the MCMC is a

map of the likelihood in the full high-dimensional parameter space that can be eventually reduced to 1- or 2-dimensional projection afterwards. In contrast, maximization algorithms must be combined with a fixed-step grid for each of the projections needed. In any case the MCMC is more likely to evidence secondary maxima.

The implementation of MCMC's in `SFitter` is based on the Metropolis-Hastings algorithm [117, 118]. It starts from an input point of the space, θ, and proposes a new point θ' to add to the Markov chain. The point is kept or rejected depending on its likelihood and the one of the current point: if $\mathscr{L}(\theta') > \mathscr{L}(\theta)$ the point is accepted, otherwise it is kept with probability $\mathscr{L}(\theta')/\mathscr{L}(\theta)$. The procedure iterates restarting from the last accepted value of θ.

The algorithm uses a density function $Q(\theta, \theta')$ to randomly draw the new proposed set of parameters. The resolving power as well as the computing efficiency of the MCMC depend on the shape of $Q(\theta, \theta')$. For example, a Gaussian distribution centred in θ tends to concentrate the Markov-chain sample around the point with maximum likelihood giving very good resolution, but the price to pay is a less efficient coverage of the space because of the small probability to generate points far from θ. A flat distribution, instead, spreads the proposals over a too wide area. A Breit-Wigner distribution is a sensible alternative, since its large tails allow a broad sampling over the full space, conserving a preference for the current value of θ. For our analyses, the Breit-Wigner distribution is employed. The rate for proposed points to be accepted as part of the Markov chain is comprised between 30% and 50%.

7.5 Results for benchmark Point 1

Table 7.1 summarizes the different observables available for the benchmark Point 1, assuming 300 fb^{-1} of luminosity delivered by the LHC to both ATLAS and CMS experiments. In addition to the two measurements and the two limits derived in Chapter 6 from supersymmetry searches, the mass of the top quark and of the lightest Higgs boson are taken into account. Their error estimates come from [104]. In particular, since the lightest Higgs is SM-like in this scenario, its mass is expected to be measurable very precisely from the di-photon decay channel with standard gluon-gluon fusion Higgs production.

Measurement		**Value**	**Stat+Syst**	**LES**	**JES**
m_t	(GeV)	175	0.01		1
m_h	(GeV)	114.3	0.01	0.25	
M_{hq}^{edge}	(GeV)	732	6		7
$M_{hq}^{\text{threshold}}$	(GeV)	410	18		4
$\sigma(h \to b\bar{b})/\sigma(Z \to \ell^+\ell^-)$		> 28			@ 95% CL
$\sigma(\text{Any} \to \ell^+\ell^-)/\sigma(Z \to \ell^+\ell^-)$		< 0.29			@ 95% CL
m_{H^0}	(GeV)	629	60		6
$BR(h \to \gamma\gamma)/BR(h \to b\bar{b})$	($\times 10^{-3}$)	2	1		
$BR(h \to \tau^+\tau^-)/BR(h \to WW)$		1.2	0.6		

Table 7.1: Summary of the different LHC observables available for the benchmark Point 1. The second column reports the true values of the measured quantities. The last three columns list respectively the quadratic sum of the statistical and uncorrelated systematic errors, the electromagnetic energy scale (LES) and hadronic energy scale uncertainties (JES).

The last three lines in Table 7.1 are additional measurements that should be achieved at the LHC, even though considered very challenging. The heavy neutral CP-even Higgs boson has mass above 600 GeV and, since $\tan\beta = 20$, is at the limit of the discovery reach of ATLAS. However, we assume here that the significance necessary for the discovery claim can be achieved by the combination of ATLAS and CMS experiments, as showed in [119], and m_{H^0} measured from the $H^0 \to \tau^+\tau^-$ channel with the worst possible statistical error (10%) [67]. The $BR(h \to \gamma\gamma)/BR(h \to b\bar{b})$ ratio comes from the analysis of $t\bar{t}h$ associated production, with subsequent Higgs decay either into photons or b-jets [67]. Similarly, $BR(h \to \tau^+\tau^-)/BR(h \to WW)$ exploits the weak vector boson fusion channels [84].

The true values of the measured quantities are smeared according to the estimated uncertainties, in order to build a set of fictitious data. Given this data set, the likelihood is then mapped over the entire parameter space of mSUGRA, comprising the extra parameter m_t, which, because of the sizable error on it, must be part of the fit. Since it is difficult to deal with discrete parameters, two different analyses are performed,

one for each sign of the μ parameter.

The resulting `SFitter` output is a complete 5-dimensional map of the likelihood function. In order to reduce the likelihood to a lower-dimensional function, we use the profile likelihood technique: for each fixed bin in the $(n-1)$-dimensional space, the likelihood is explored along the n^{th} dimension and only its highest value is kept.

The profile χ^2 (log-likelihood) distributions for positive μ are reported in Figures 7.1 and 7.2.

The best-fitting point is clearly distinct in the profile χ^2 as function of M_0 and $M_{1/2}$. The region with minimum χ^2 is particularly narrow in the $M_{1/2}$ dimension. This is the most constrained parameter of the fit, since the lightest Higgs mass strongly depends on it through radiative corrections. A secondary local minimum appears in the region $M_{1/2} \sim 100$ GeV, where the Higgs mass is kept high by large negative values of A.

The 1-dimensional profile χ^2 distributions (full dots) are, in very good approximation, parabolic. Non-Gaussian contribution to the likelihood only comes from factors like Equation 7.5, needed for including upper and lower limits. Because of the non-trivial relation between observables and parameters, the parabola widths might be asymmetric with respect to the minimum, as for the M_0 parameter.

The blue-bands in the 1-dimensional profile χ^2 distributions indicate regions where χ^2 variates of less than one unit with respect to its minimum. Therefore, the parameter interval for which the parabola stays inside the blue-band are the 68% confidence intervals:

$$\begin{array}{rcccl} 290 & < & M_0 \text{ (GeV)} & < & 450 \\ 385 & < & M_{1/2} \text{ (GeV)} & < & 420 \\ -250 & < & A \text{ (GeV)} & < & 150 \\ 13 & < & \tan\beta & < & 34 \\ 173.2 & < & m_t \text{ (GeV)} & < & 175.2. \end{array}$$

To cross-check the Markov-chain Monte Carlo method, the 1-dimensional χ^2 functions for M_0, $M_{1/2}$, A and $\tan\beta$ are also calculated with `Migrad` (empty dots). The two methods show a very good agreement. The better resolution of `Migrad` cause a slight global shift to lower χ^2 values, which, however, does not affect the $\Delta\chi^2$ relative to the minimum and, thus, the confidence intervals. Differences at small M_0 arise because there we approach to the bounds of the Higgs and Z production rate measurements. While `Migrad` runs at fixed M_0, the MCMC is free to move inside the bin width where

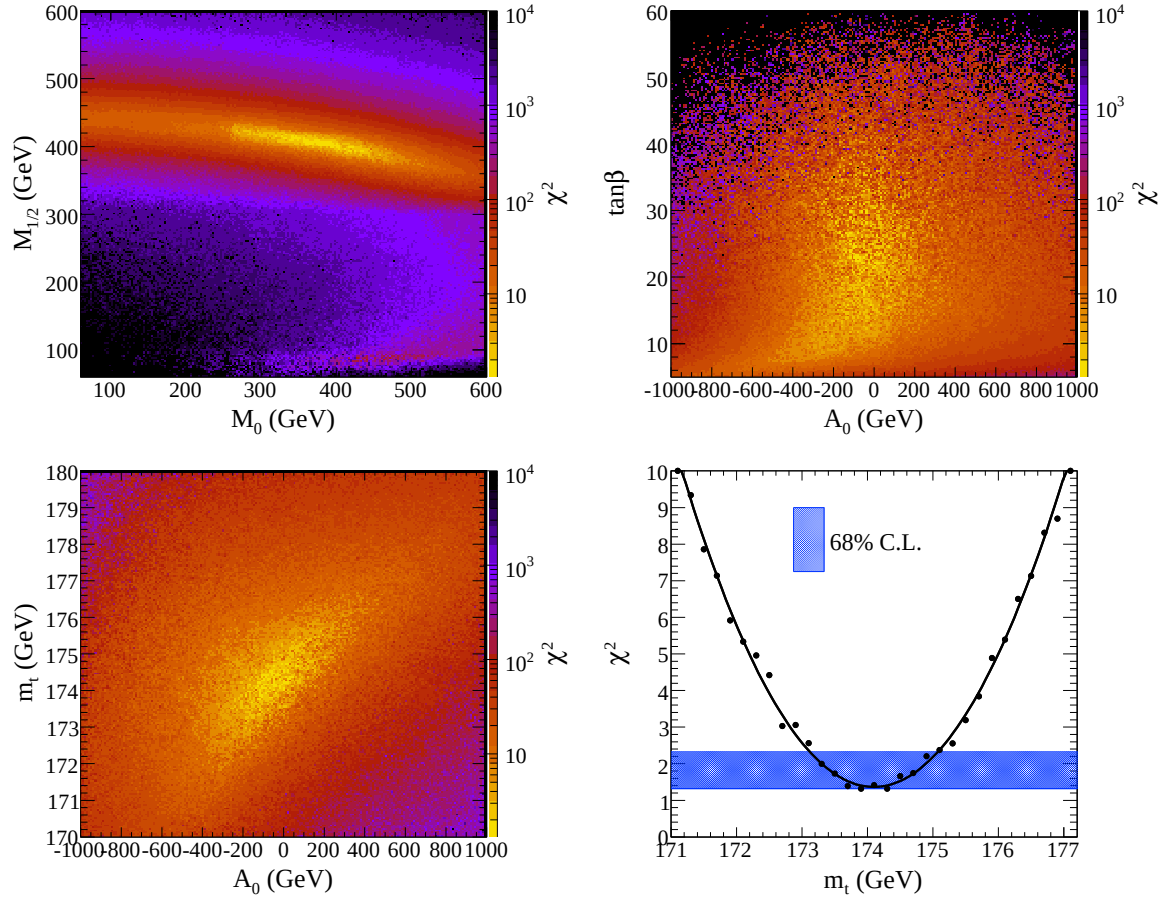

Figure 7.1: Profile χ^2 in the mSUGRA space with positive μ. The input is a data set smeared according to Table 7.1.

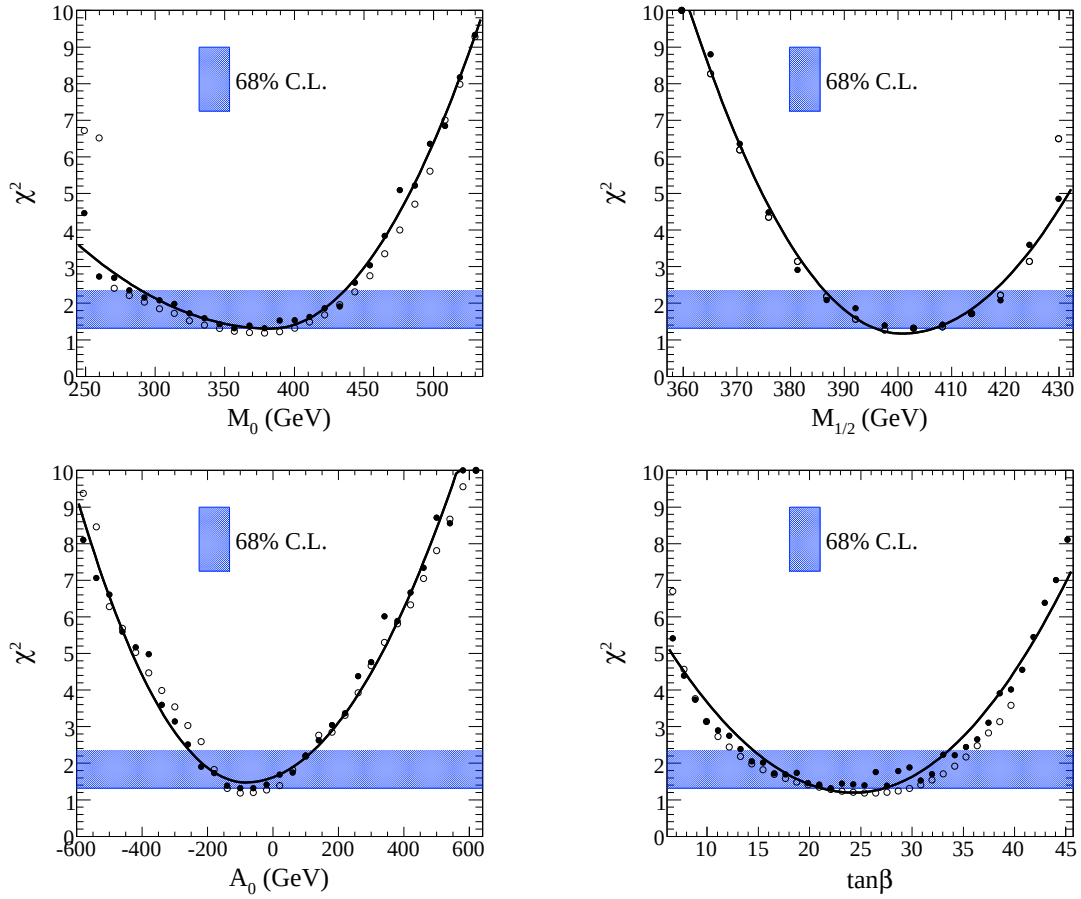

Figure 7.2: Profile χ^2 in the mSUGRA space with positive μ. The input is a data set smeared according to Table 7.1. The full dots derived with a Markov-chain Monte Carlo method can be compared to the empty dots computed by the `Migrad` algorithm.

	M_0	$M_{1/2}$	A	$\tan\beta$	m_t
M_0	1	-0.93	-0.64	$+0.39$	-0.23
$M_{1/2}$		1	$+0.83$	-0.44	$+0.51$
A			1	-0.41	$+0.83$
$\tan\beta$				1	-0.33
m_t					1

Table 7.2: Correlation matrix of the mSUGRA parameters in the fit with fixed positive μ. The input is a data set smeared according to Table 7.1.

it can find sufficiently high values of M_0 to satisfy one or both bounds.

Using the `Migrad` algorithm, we can also obtain the correlation matrix of the five parameters, reported in Table 7.2.

The likelihood mapping is performed again with negative μ. Figure 7.3 shows the main results.

All the local χ^2-minima in the mSUGRA space found by `SFitter`, both with positive and negative μ, are listed in Table 7.3. Even though the χ^2 is better for $\mu > 0$ than for $\mu < 0$, the wrong sign hypothesis cannot be discarded on the basis of its p-value. A helpful information to select the right μ sign is the experimental value of the anomalous magnetic moment of the muon [120]. Indeed, the correction from SUSY particle virtual loops is proportional to the sign of μ, causing the SUSY prediction to approach the measured value for positive μ and to increase the discordance for negative μ. For instance, for the two leading points, the SUSY contribution to the $(g/2)_\mu$ SM prediction is respectively 1.83×10^{-9} and -1.58×10^{-9}, to be compared with the actual measurement 2.75×10^{-9} (Section 1.3): the minimum with negative μ is excluded at about 5σ level.

To further stress the analysis, we consider the pessimistic case where the observations of m_{H^0}, $BR(h\to\gamma\gamma)/BR(h\to b\bar{b})$ and $BR(h\to\tau^+\tau^-)/BR(h\to WW)$ are not

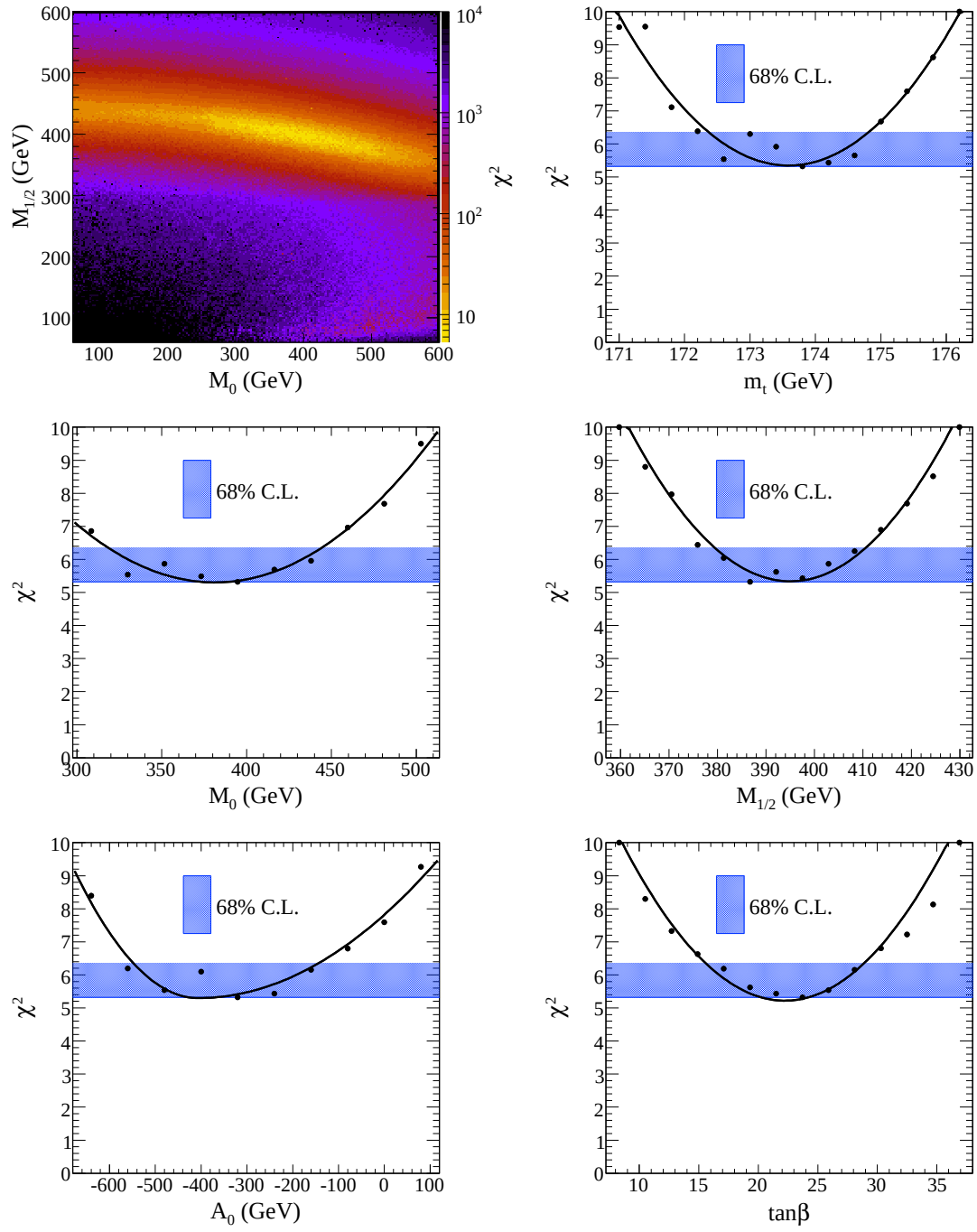

Figure 7.3: Profile χ^2 in the mSUGRA space with negative μ. The input is a data set smeared according to Table 7.1.

M_0 (GeV)	$M_{1/2}$ (GeV)	A (GeV)	$\tan\beta$	m_t (GeV)	sgnμ	χ^2/N_{dof}	p-value
300	**425**	**200**	**20**	**175.0**	**+**	**True values**	
387	407	−52	27	174.3	+	1.18/4	88%
423	394	−253	25	174.4	−	5.32/4	25%
509	92	−987	27	179.8	+	139/4	$< 10^{-16}$
506	87	−995	20	175.0	−	205/4	$< 10^{-16}$
			⋮				

Table 7.3: Local likelihood maxima in the mSUGRA fit. The input is a data set smeared according to Table 7.1. In the first line, the true values of the mSUGRA parameters are recalled.

accessible at the LHC. The derived confidence intervals for positive μ are:

$$\begin{aligned} 150 &< M_0 \text{ (GeV)} < 620 \\ 360 &< M_{1/2} \text{ (GeV)} < 450 \\ -300 &< A \text{ (GeV)} < 200 \\ &\tan\beta : \text{unconstrained} \\ 173.2 &< m_t \text{ (GeV)} < 175.2. \end{aligned}$$

The parameters strongly related to m_h, i.e. $M_{1/2}$ and A, are almost not affected. Also the top mass remains obviously unchanged, since it is controlled by its direct measurement. Instead, $\tan\beta$ is now completely unconstrained over the theoretically allowed region ($2 \lesssim \tan\beta \lesssim 60$), as the informations on it are carried by the measurements in the Higgs sector. Also the performance on the M_0 determination degrades, revealing that its precision is dominated by the heavy Higgs mass measurement.

7.6 Results for benchmark Point 2

The input data set for the benchmark Point 2 differs from Table 7.1 in two elements. Firstly, the threshold in the invariant mass of the system Higgs plus jet is not available because of the large $b\bar{b}$ background, as discussed in Section 6.5, thus it is removed from the fit. Secondly, this point has been chosen to have a lightest neutralino compatible with the relic density of cosmological cold dark matter observed by the WMAP

Measurement		Value	Stat+Syst	LES	JES
Ωh^2		0.88	0.009		
m_t	(GeV)	175	0.01		1
m_h	(GeV)	114.5	0.01	0.25	
M_{hq}^{edge}	(GeV)	762	7		7
$\sigma(h \to b\bar{b})/\sigma(Z \to \ell^+\ell^-)$		> 13			@ 95% CL
$\sigma(\text{Any} \to \ell^+\ell^-)/\sigma(Z \to \ell^+\ell^-)$		< 0.05			@ 95% CL
m_{H^0}	(GeV)	411	40		4
$BR(h \to \gamma\gamma)/BR(h \to b\bar{b})$	($\times 10^{-3}$)	2	1		
$BR(h \to \tau^+\tau^-)/BR(h \to WW)$		1.2	0.6		

Table 7.4: Summary of the different observables available for the benchmark Point 2. The LHC measurements are completed by the relic density of cosmological cold dark matter observed by the WMAP experiment. The second column reports the true values of the measured quantities. The last three columns list respectively the quadratic sum of the statistical and uncorrelated systematic errors, the electromagnetic energy scale (LES) and hadronic energy scale uncertainties (JES).

experiment. Consequently, it is interesting to insert the relic density of the lightest supersymmetric particle in the likelihood function and investigate its effect on the `SFitter` results.

Table 7.4 lists all the measurements included in the fit. The experimental value used for the LSP relic density is not a smearing of the true value, as done for the other measurements, but rather the current WMAP estimate, shown in Equation 6.4.

The profile χ^2 distributions for the mSUGRA parameter space, for fixed positive μ, are reported in Figure 7.4.

The scan properly identifies the region corresponding to the true mSUGRA parameters of the benchmark Point 2. The absolute value of the minimum is $\chi^2_{\text{min}} = 1.90$, with $N_{\text{dof}} = 4$. Outside this region, two more local minima are present. We find a minimum at $M_{1/2} \sim 100$ GeV, as in the scan for the benchmark Point 1, and an additional spot around $(M_0, M_{1/2}) = (150\text{ GeV}, 450\text{ GeV})$, which can be better understood by looking at the correlation between $\tan\beta$ and M_0. These parameters are indeed

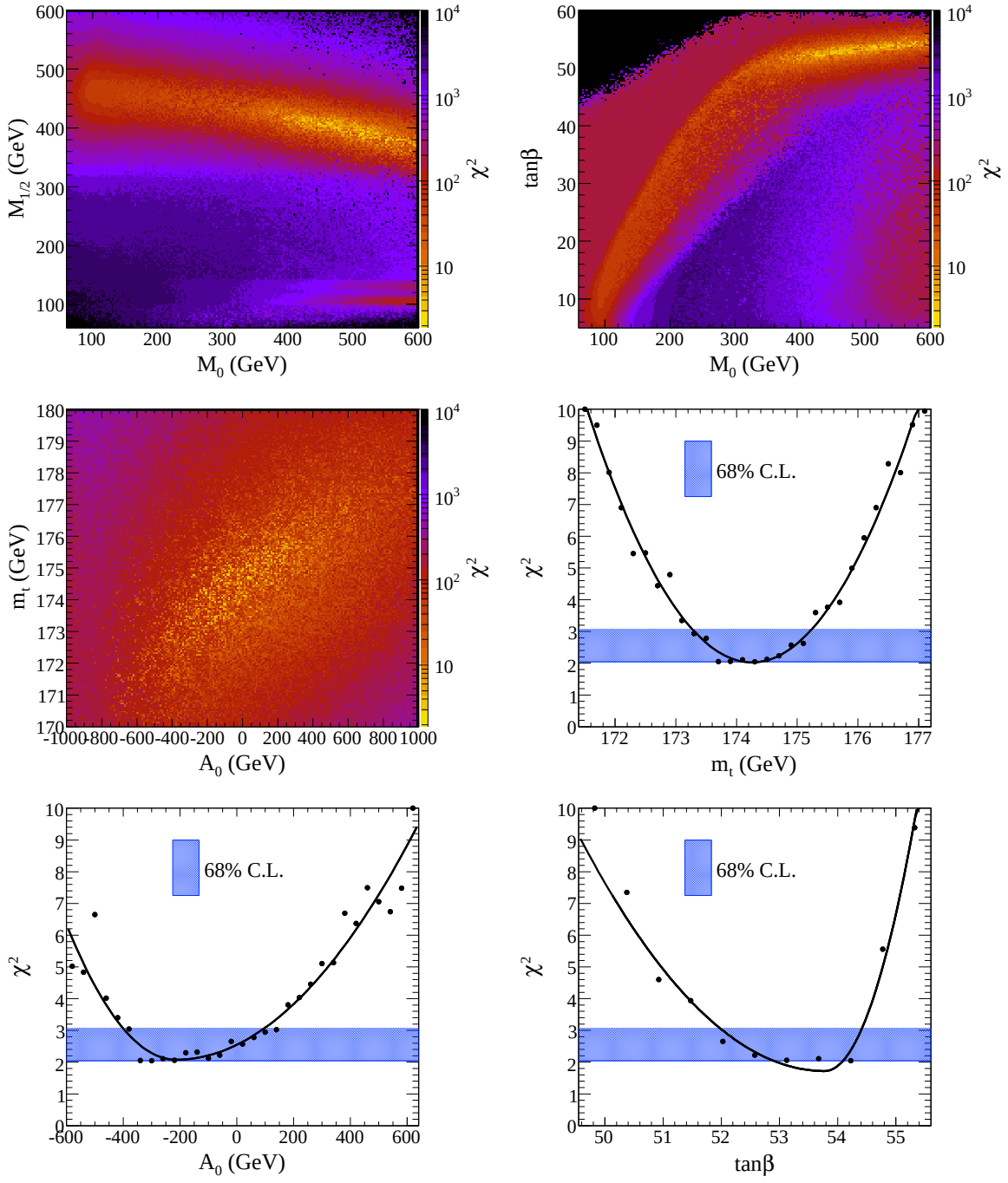

Figure 7.4: Profile χ^2 in the mSUGRA space with positive μ. The input is a data set smeared according to Table 7.4. The experimental value used for the LSP relic density is the current WMAP estimate, shown in Equation 6.4.

M_0 (GeV)	$M_{1/2}$ (GeV)	A (GeV)	$\tan\beta$	m_t (GeV)	sgnμ	χ^2/N_{dof}	p-value
500	**400**	**0**	**54**	**175.0**	**+**	**True values**	
545	387	−91	54	174.8	+	1.90/4	75%
171	452	131	30	173.3	+	32.5/4	$\sim 10^{-6}$
592	107	−995	27	174.2	+	85.3/4	$< 10^{-16}$
			⋮				

Table 7.5: Local likelihood maxima in the mSUGRA fit. The input is a data set smeared according to Table 7.4. The experimental value used for the LSP relic density is the current WMAP estimate, shown in Equation 6.4. In the first line, the true values of the mSUGRA parameters are recalled.

strongly correlated through the constrain on the dark matter relic density. The red and yellow strip, crossing the $(M_0, \tan\beta)$-plane approximatively from bottom-left to top-right, is favoured by the WMAP experiment. Moving from this strip towards lower M_0, the $\tilde{\tau}_1$ becomes lighter than the $\tilde{\chi}_1^0$, provoking a sudden jump in Ωh^2 followed by a relatively flat area. Moving in the opposite direction, the relic density of the lightest neutralino increases less rapidly but to less likely values. The local minimum at low M_0 in the $(M_0, M_{1/2})$-plane is the projection of the WMAP-preferred band.

The best-χ^2 local minima are listed in Table 7.5

From the 1-dimensional profile χ^2 distributions, we deduce the 68% confidence intervals:

$$\begin{aligned} 400 &< M_0 \text{ (GeV)} < 560 \\ 365 &< M_{1/2} \text{ (GeV)} < 405 \\ -300 &< A \text{ (GeV)} < 100 \\ 52.2 &< \tan\beta < 54.4 \\ 173.2 &< m_t \text{ (GeV)} < 175.2. \end{aligned}$$

With respect to results for mSUGRA Point 1, the major difference is in $\tan\beta$ determination. The stringent requirement on the LSP relic density strongly constrains its confidence interval.

8

CONCLUSIONS

Despite its success and the many experimental measurements that confirm its validity at the energy scales currently explored, the Standard Model of particle physics remains incomplete. Observations such as neutrino masses, the presence of dark matter in the universe and the asymmetry between baryon and anti-baryon, as well as problems of consistency of the theory suggest the existence of new phenomena, not yet discovered.

Supersymmetric extensions of the Standard model are among the best motivated models of new physics and predict a large spectrum of new, so far unobserved particles with mass at the TeV scale, which are therefore expected to be produced at the LHC. The search for evidence of supersymmetry will be a primary goal of the ATLAS experiment at the time of the first proton-proton collisions, foreseen for September 2008.

In the context of supersymmetric models, the lightest Higgs boson can be produced via cascade decays of supersymmetric particles. The distinctive signature of this process is composed of the pair of particles from Higgs disintegration, typically two bottom quarks, and of missing energy, due to the production of supersymmetric particles escaping the detection. We develop, through detailed simulation studies, a complete analysis designed to

- ensure a solid and reliable missing energy reconstruction with the ATLAS detector;
- evaluate the ATLAS potential in discovering the Higgs produced through this mechanism;

- investigate the possibility to derive the fundamental masses and couplings of the underlying model, once its discovery is confirmed.

The work initially focuses on the performance of the missing energy measurement, with particular interest in the reduction of instrumental effects, such as electronic noise and poor determination of hadronic jet energy. Furthermore, we establish, inside the detector monitoring framework, a system that constantly controls during data acquisition operations the reconstruction of missing energy. The capability of the monitoring system in revealing problems is tested against detector failures, showing promising results in terms of sensitivity and detection promptness.

Subsequently, the discovery potential of the lightest neutral Higgs boson is studied in detail in two supersymmetric scenarios with different phenomenological features. We show that 5σ evidence of a Higgs resonance in the two-b-jet invariant mass distribution can be obtained with less than 10 fb^{-1} of collected data. The possibility of observing a Higgs peak in the $\gamma\gamma$ channel is also investigated. Moreover, various measurements, useful to determine the nature of the new particles involved in the Higgs boson production, are proposed and their uncertainties are estimated assuming a luminosity of 300 fb^{-1}. In particular, we consider the determination of threshold and edge points in the invariant mass of the Higgs plus jet system and the production rates of Higgs and Z bosons.

In the last part of the dissertation, we describe a statistical method to extract the parameters of a supersymmetric model, starting from a set of LHC measurements. The method is applied to the particular case of the previously presented supersymmetric scenarios, proving the validity of the method, even in exploring models with high-dimensional parameter spaces.

A

CALCULATION OF CASCADE KINEMATICS

We illustrate a sample calculation of thresholds and edges in invariant mass distributions of the final states arising in decay cascades.

We derive below Equations 6.6 and 6.7, respectively the threshold and edge of the invariant mass distribution of the system Higgs plus quark coming from the cascade:

$$\tilde{q}_L \rightarrow \tilde{\chi}_2^0 q \rightarrow \tilde{\chi}_1^0 h q. \tag{A.1}$$

Since the only condition we assume here is $m_q = 0$, the procedure is valid for any cascade with the same pattern, provided that the initiating particle decays to at least one massless state.

The schema of the calculation is represented in Figure A.1. We start computing the energies and momenta of the quark and the second lightest neutralino in the frame of reference where the $\tilde{q}_L$ is at rest. Then, we boost the quark to the frame of reference where the $\tilde{\chi}_2^0$ is at rest. In this frame, we also calculate the energy and momentum of the Higgs. Finally, the four-momenta of the quark and the Higgs are summed together and the resulting total four-momentum is squared to give M_{hq}^2.

In the frame of reference with the $\tilde{q}_L$ at rest, we must solve the system

$$\begin{cases} m_{\tilde{q}} &= E_{\tilde{\chi}_2^0} &+ E_q \\ 0 &= \vec{p}_{\tilde{\chi}_2^0} &+ \vec{p}_q. \end{cases} \tag{A.2}$$

From the first equation and imposing the mass-shell conditions, we find

$$E_{\tilde{\chi}_2^0}^2 = m_{\tilde{\chi}_2^0}^2 + |\vec{p}_{\tilde{\chi}_2^0}|^2 = (m_{\tilde{q}} - |\vec{p}_q|)^2, \tag{A.3}$$

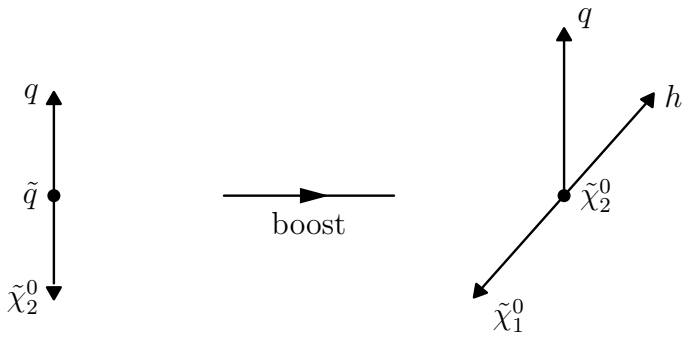

Figure A.1: Schema of the calculation of $M_{hq,\text{threshold}}$ and $M_{hq,\text{edge}}$.

that can be developed and simplified by using $|\vec{p}_q| = |\vec{p}_{\tilde{\chi}_2^0}|$:

$$m_{\tilde{\chi}_2^0}^2 + |\vec{p}_{\tilde{\chi}_2^0}|^2 = m_{\tilde{q}}^2 - 2m_{\tilde{q}}|\vec{p}_{\tilde{\chi}_2^0}| + |\vec{p}_{\tilde{\chi}_2^0}|^2. \tag{A.4}$$

It follows that

$$|\vec{p}_{\tilde{\chi}_2^0}| = |\vec{p}_q| = E_q = \frac{m_{\tilde{q}}^2 - m_{\tilde{\chi}_2^0}^2}{2m_{\tilde{q}}}. \tag{A.5}$$

The four-momentum of the quark in the frame of reference where the $\tilde{\chi}_2^0$ is at rest can be derived by applying a boost opposite to the $\tilde{\chi}_2^0$ direction. That is

$$\begin{pmatrix} E'_q \\ |\vec{p}'_q| \end{pmatrix} = \begin{pmatrix} \gamma & +\beta\gamma \\ +\beta\gamma & \gamma \end{pmatrix} \begin{pmatrix} E_q \\ |\vec{p}_q| \end{pmatrix}, \tag{A.6}$$

where $\gamma = E_{\tilde{\chi}_2^0}/m_{\tilde{\chi}_2^0}$ and $\beta = |p_{\tilde{\chi}_2^0}|/E_{\tilde{\chi}_2^0}$. The positive sign in the Lorentz transformation indicates that the boost is opposite to $\vec{p}_{\tilde{\chi}_2^0}$. With a bit of algebra we calculate γ and $\beta\gamma$, then we replace their expressions in Equation A.6 in order to find E'_q:

$$\gamma^2 = \frac{m_{\tilde{\chi}_2^0}^2 + |\vec{p}_{\tilde{\chi}_2^0}|^2}{m_{\tilde{\chi}_2^0}^2} = 1 + \frac{(m_{\tilde{q}}^2 - m_{\tilde{\chi}_2^0}^2)^2}{4m_{\tilde{q}}^2 m_{\tilde{\chi}_2^0}^2} = \frac{(m_{\tilde{q}}^2 + m_{\tilde{\chi}_2^0}^2)^2}{4m_{\tilde{q}}^2 m_{\tilde{\chi}_2^0}^2}; \tag{A.7}$$

$$(\beta\gamma)^2 = \frac{|\vec{p}_{\tilde{\chi}_2^0}|^2}{m_{\tilde{\chi}_2^0}^2} = \frac{(m_{\tilde{q}}^2 - m_{\tilde{\chi}_2^0}^2)^2}{4m_{\tilde{q}}^2 m_{\tilde{\chi}_2^0}^2}; \tag{A.8}$$

$$E'_q = |\vec{p}'_q| = (\gamma + \beta\gamma)E_q = \frac{2m_{\tilde{q}}^2}{2m_{\tilde{q}}m_{\tilde{\chi}_2^0}}E_q = \frac{m_{\tilde{q}}}{m_{\tilde{\chi}_2^0}}E_q = \frac{m_{\tilde{q}}^2 - m_{\tilde{\chi}_2^0}^2}{2m_{\tilde{\chi}_2^0}}. \tag{A.9}$$

Now, we have to compute the Higgs energy and momentum in the frame of reference with the $\tilde{\chi}_2^0$ at rest. From

$$\begin{cases} m_{\tilde{\chi}_2^0} &= E_{\tilde{\chi}_1^0} &+ E_h \\ 0 &= \vec{p}_{\tilde{\chi}_1^0} &+ \vec{p}_h, \end{cases} \tag{A.10}$$

it follows that

$$E_h = m_{\tilde{\chi}_2^0} - E_{\tilde{\chi}_1^0}, \tag{A.11}$$

$$E_h^2 = (m_{\tilde{\chi}_2^0} - E_{\tilde{\chi}_1^0})^2, \tag{A.12}$$

$$m_h^2 + |\vec{p}_h|^2 = m_{\tilde{\chi}_2^0}^2 - 2m_{\tilde{\chi}_2^0}\sqrt{m_{\tilde{\chi}_1^0}^2 + |\vec{p}_{\tilde{\chi}_1^0}|^2} + m_{\tilde{\chi}_1^0}^2 + |\vec{p}_{\tilde{\chi}_1^0}|^2, \tag{A.13}$$

$$m_h^2 = m_{\tilde{\chi}_2^0}^2 - 2m_{\tilde{\chi}_2^0}\sqrt{m_{\tilde{\chi}_1^0}^2 + |\vec{p}_{\tilde{\chi}_1^0}|^2} + m_{\tilde{\chi}_1^0}^2. \tag{A.14}$$

After bringing $m_{\tilde{\chi}_2^0}^2$ and $m_{\tilde{\chi}_1^0}^2$ to the left side of Equation A.14, we square and get

$$(m_h^2 - m_{\tilde{\chi}_2^0}^2 - m_{\tilde{\chi}_1^0}^2)^2 = 4m_{\tilde{\chi}_2^0}^2(m_{\tilde{\chi}_1^0}^2 + |\vec{p}_{\tilde{\chi}_1^0}|^2). \tag{A.15}$$

Therefore,

$$|\vec{p}_{\tilde{\chi}_1^0}| = |\vec{p}_h| = \frac{\sqrt{(m_h^2 - m_{\tilde{\chi}_2^0}^2 - m_{\tilde{\chi}_1^0}^2)^2 - 4m_{\tilde{\chi}_2^0}^2 m_{\tilde{\chi}_1^0}^2}}{2m_{\tilde{\chi}_2^0}} \tag{A.16}$$

and

$$|E_h| = \frac{m_h^2 + m_{\tilde{\chi}_2^0}^2 - m_{\tilde{\chi}_1^0}^2}{2m_{\tilde{\chi}_2^0}}. \tag{A.17}$$

As last step of the calculation, we must sum and square the four-momenta of the quark and the Higgs. Aligning the coordinate system to the quark direction and naming α the angle between them, we set:

$$p_q' = (E_q', 0, 0, E_q') \tag{A.18}$$

and

$$p_h = (E_h, 0, |\vec{p}_h|\sin\alpha, |\vec{p}_h|\cos\alpha). \tag{A.19}$$

Their squared invariant mass is then

$$\begin{aligned} M_{hq}^2 = (p_h + p_q')^2 &= (E_h + E_q')^2 - |\vec{p}_h|^2\sin^2\alpha - (|\vec{p}_h|\cos\alpha + E_q')^2 = \\ &= E_h^2 + E_q'^2 + 2E_hE_q' - |\vec{p}_h|^2 - E_q'^2 - 2E_q'|\vec{p}_h|\cos\alpha = \\ &= m_h^2 + 2E_q'(E_h - |\vec{p}_h|\cos\alpha). \end{aligned} \tag{A.20}$$

The function has a minimum and a maximum for $\cos\alpha = \pm 1$, for which we recover the expressions reported in Chapter 6

$$M^2_{hq,\text{threshold}} = \frac{m^2_{\tilde{q}_L} - m^2_{\tilde{\chi}^0_2}}{2m^2_{\tilde{\chi}^0_2}} \left[m^2_{\tilde{\chi}^0_2} + m^2_h - m^2_{\tilde{\chi}^0_1} - \sqrt{\delta} \right] + m^2_h, \tag{A.21}$$

$$M^2_{hq,\text{edge}} = \frac{m^2_{\tilde{q}_L} - m^2_{\tilde{\chi}^0_2}}{2m^2_{\tilde{\chi}^0_2}} \left[m^2_{\tilde{\chi}^0_2} + m^2_h - m^2_{\tilde{\chi}^0_1} + \sqrt{\delta} \right] + m^2_h, \tag{A.22}$$

$$\delta = (m^2_{\tilde{\chi}^0_2} - m^2_h - m^2_{\tilde{\chi}^0_1})^2 - 4m^2_h m^2_{\tilde{\chi}^0_1}. \tag{A.23}$$

ACKNOWLEDGMENTS

This work has been made possible by the constant support from the LAPP, which I sincerely thank for the welcome received.

I am grateful to my supervisors Rémi Lafaye and Lucia Di Ciaccio for sharing their knowledge with me and for the constant interest held in my research activities. My acknowledgements also address to the members of the ATLAS group at LAPP, for the many discussions and important suggestions.

I acknowledge the referees of this manuscript, Pascal Gay and Michel Lefebvre, and the examining committee members, Margarete Muehlleitner, Giacomo Polesello and Mossadek Talby, for the time spent in reading this work and for their useful comments and advices.

RÉSUMÉ

Sommaire

En septembre 2008 le LHC livrera ses premières collisions proton-proton. Auprès du LHC, l'expérience ATLAS est conçue pour explorer un large éventail de phénomènes et traquer les signes de nouvelle physique, qui pourraient se manifester lors de ces interactions. Ainsi, dans le cadre des extensions supersymétriques du Modèle Standard, le boson de Higgs le plus léger pourrait être produit dans les cascades de désintégrations de particules supersymétriques. Nous étudions la possibilité d'observer de tels événements avec le détecteur ATLAS. Tout d'abord, nous examinons la capacité d'ATLAS à mesurer l'énergie manquante due au passage des particules supersymétriques qui échappent à la détection. Ensuite, nous montrons que, pour certaines régions de l'espace des paramètres du modèle de Supergravité Minimale, compatibles avec les dernières recherches au LEP, le plus léger boson de Higgs peut être découvert avec moins de 10 fb^{-1}. Ces résultats sont compétitifs avec les canaux standard de production du Higgs. Nous étudions aussi la possibilité de mesurer des quantités liées aux masses et aux couplages des particules supersymétriques impliquées dans ce processus. Enfin, à partir de ces mesures, nous utilisons l'outil `SFitter` pour réaliser un ajustement global des paramètres du modèle supersymétrique sous-jacent, en montrant ainsi la validité de cette procédure pour contraindre les interprétations théoriques des futures données du LHC.

Le Modèle Standard

Le Modèle Standard (SM) est à l'heure actuelle la meilleure description des interactions entre particules ; sa validité a été testée et confirmée à un niveau de précision

extraordinairement élevé.

Le Modèle Standard comprend tous les constituants fondamentaux de la matière, ayant tous un spin 1/2 : trois leptons chargés (e, μ, τ), trois leptons neutres $(\nu_e, \nu_\mu, \nu_\tau)$ et trois familles de quarks (u, d), (c, s) et (t, b). Les interactions entre ceux-ci sont décrites par l'échange de boson vecteurs. Ainsi, le photon est responsable de l'interaction électromagnétique entre les particules chargés. Les bosons $W^\pm$ et Z^0 sont associés à l'interaction faible, dont la plus connue des manifestations est la désintégration β du neutron. Enfin, huit gluons sont responsables des interactions fortes, qui lient les quarks à l'intérieur des protons et des neutrons.

Ce cadre décrit complètement toutes les forces fondamentales connues dans la nature, à l'exception de la gravité. En fait, dans le contexte de la physique des particules, la gravitation est extrêmement faible et donc négligeable, du moins à toutes les énergies auxquelles nous serons intéressés. Pour donner une idée de son ampleur, l'attraction gravitationnelle entre deux protons dans un noyau est $\sim 10^{-36}$ fois plus faibles que leur répulsion électromagnétique. La force gravitationnelle devient comparable aux autres forces fondamentales pour des énergies à l'échelle de Planck, $\Lambda_{\text{Planck}} \sim 10^{19}$ GeV, c'est-à-dire plus de dix ordres de grandeur au dessus de la valeur expérimentale atteinte actuellement.

La base du Modèle Standard est le principe de symétrie de jauge, qui consiste dans l'invariance de la théorie sous des transformations locales, donc dépendantes de l'espace-temps, appelées transformations de jauge. Les interactions entre particules et les bosons médiateurs associés sont complètement définis par le choix de ces transformations.

La symétrie de jauge du Modèle Standard est décrite par le groupe unitaire $SU(3)_C \times SU(2)_L \times U(1)_Y$. Le groupe $SU(3)_C$ est associés à l'interaction forte et ses huit gluons. Le restant $SU(2)_L \times U(1)_Y$ engendre les quatre bosons médiateurs des interactions électromagnétiques et faibles (ou électrofaibles). Tous les bosons de jauge ainsi obtenus sont sans masse. Toutefois, les mesures de la désintégration du neutron indiquent que les intermédiaires sont plutôt des bosons massifs. Mais l'introduction des termes de masse pour les bosons vecteurs supprime l'invariance de jauge et produit une inconsistance dans la théorie.

En outre, la symétrie $SU(2)_L$ interdit également les masses des fermions. Le mécanisme

de brisure spontanée de symétrie (Brout, Engler, Higgs [11, 12, 13, 14]) offre une solution à ce problème. Son application au groupe $SU(2)_L \times U(1)_Y$, proposée par Glashow, Salam et Weinberg [15, 16], apporte des masses aux fermions et aux bosons sans affecter l'invariance de jauge de la théorie. Le prix à payer est la présence d'une nouvelle particule scalaire non encore découverte, le boson de Higgs.

Même si la présence d'un boson de Higgs était confirmée expérimentalement, il est couramment admis que le Modèle Standard n'est pas la théorie ultime de la physique des particules. Des observations comme la masse des neutrinos [41, 42, 43, 44, 28, 45], la présence de matière noire dans l'univers [37, 38, 39, 40, 28] et l'asymétrie entre baryon et anti-baryon [38, 39, 28] suggèrent l'existence de nouveaux phénomènes. En outre, lorsqu'on introduit le champ scalaire de Higgs, il se présente un problème de naturalité. Les corrections radiatives à la masse du boson de Higgs sont proportionnelles à la plus élevée des échelles d'énergie où le Modèle Standard est valide, Λ_{UV}. Donc pour avoir la masse du boson de Higgs à son échelle naturelle, c'est-à-dire l'échelle des forces électrofaibles, Λ_{UV} doit être du même ordre d'énergie, $\Lambda_{\mathrm{UV}} \sim 1$ TeV, ce qui implique la présence de nouvelles particules et interactions à des énergies accessibles par le LHC.

Le Modèle Standard Supersymétrique Minimal

Les modèles supersymétriques (SUSY) sont parmi les extensions les mieux motivées du Modèle Standard. Ils fournissent une solution au problème de naturalité, grâce à l'introduction d'une symétrie entre bosons et fermions. Toutes les corrections radiatives à la masse du Higgs proportionnelles à Λ_{UV} sont ainsi exactement annulées. La masse du boson de Higgs est alors préservée à son échelle naturelle et la validité du modèle peut, en principe, s'étendre jusqu'aux énergies de Planck.

La version avec contenu de particules minimale est appelée Modèle Standard Supersymétrique Minimal (MSSM) [52, 55]. À chaque fermion (boson) du Modèle Standard est associé un partenaire supersymétrique bosonique (fermionique), de masse de l'ordre du TeV. Il est à noter que, pour éviter des inconsistances dans la théorie, le secteur du Higgs est composé de trois scalaires neutres (dont h et H^0 pairs sous CP et A^0 impair) et un chargé ($H^{\pm}$) plus leur correspondants supersymétriques.

Dans ce modèle, le temps de désintégration du proton prédit est largement incom-

patible avec les données expérimentales et la voie la plus évidente pour éliminer cette discordance est d'introduire la R-parité, définie comme $R = (-1)^{B+L+2s}$, où B, L et s sont respectivement le nombre quantique baryonique, leptonique et le spin. La conservation de cette quantité implique la présence, à chaque vertex d'interaction, d'un nombre pair de particules supersymétriques. Par conséquence la particule supersymétrique la plus légère (LSP) est stable et, si neutre, elle représente une candidate pour constituer la matière noire.

Du point de vue phénoménologique, des particules supersymétriques fortement interagissant peuvent être produites au LHC, ensuite chacune d'elles commence une cascade de désintégrations consécutives, qui se termine par la production de la LSP. Étant stable et neutre, celle-ci échappe à la détection et l'événement se caractérise par une grande quantité d'énergie manquante.

L'expérience ATLAS

La mise en évidence de phénomènes au-delà du Modèle Standard, en particulier liés à la supersymétrie, est un objectif principal du programme de physique de l'expérience ATLAS [66, 67, 68].

Elle a été conçue pour étudier les collisions proton-proton, délivrées par le LHC à l'énergie du centre de masse de 14 TeV et avec une luminosité nominale de 10^{34} $\mathrm{cm}^{-2}\mathrm{s}^{-1}$.

La conception du détecteur est déterminée par son programme de physique et par les conditions expérimentales très difficiles. En effet, la section efficace totale des interactions inélastiques proton-proton est d'environ 80 mb, correspondants à la production de 10^9 événements par seconde à la luminosité nominale. La grande majorité de ces événements contient des particules de faible impulsion transverse et a peu d'intérêt physique. Tout de même, puisque les faisceaux des protons se croisent toutes les 25 ns, lorsqu'un événement d'intérêt physique a lieu, il est superposé d'environ 25 de ces événements de basse impulsion. Ce phénomène est appelé bruit d'empilement.

Les principales exigences pour le détecteur sont résumées ici :

- Une réponse rapide du détecteur et une granularité fine sont nécessaires afin de minimiser la contamination par le bruit d'empilement.

- En raison de l'énorme flux de particules provenant des collisions proton-proton, tous les composants du détecteur doivent garantir une résistance élevée au rayonnement.
- Le système de déclenchement est une question cruciale pour les expériences au LHC. Le taux d'interaction de 10^9 événements par seconde doit être réduit jusqu'à environ 200 événements enregistrés par seconde, à cause des limites du système de stockage.
- Une couverture entièrement hermétique permet une large acceptance des signaux de physique les plus rares, ainsi que la possibilité de mesurer l'énergie manquante, causée par le passage de particules qui échappent à la détection.
- Une excellente résolution en énergie et en impulsion est nécessaire pour les photons, les électrons et les muons. Ils doivent être mesurés sur une gamme d'impulsions transverses qui varie de quelques GeV jusqu'à quelques TeV.
- D'excellentes performances sur l'identification des photons, électrons, muons, jets de τ et jets de b sont demandées pour distinguer les processus rares des événements QCD, dont le taux de production est bien plus élevé.

La Figure 3.2 montre une vue d'ensemble du détecteur ATLAS. Il comprend de nombreux sous-détecteurs assurant différentes fonctions. Le détecteur interne est le plus près du point d'interaction et il est immergé dans un champ magnétique solénoïdal de 2 T. Il permet de mesurer la dynamique des particules chargées et de reconstruire les vertex d'interaction primaires et secondaires. Le détecteur interne est entouré par le calorimètre, qui se décompose en partie électromagnétique et partie hadronique. La tache principale du calorimètre électromagétique est de reconstruire l'énergie des photons et des électrons. La mesure de l'énergie des jets de particules hadroniques est due essentiellement au calorimètre hadronique. Enfin, un aimant toroïdal entourant les calorimètres fournit le champ magnétique requis pour dévier les muons, qui peuvent être identifiés et mesurés par des détecteurs de traces.

Études sur l'énergie transverse manquante

Au LHC, les deux partons interagissant lors d'une collision proton-proton ont, en première approximation, une impulsion transverse égale à zéro. Ainsi, une impulsion

totale non compensée dans le plan orthogonal à l'axe des faisceaux révèle le passage d'une où plusieurs particules qui ont échappé à la détection. Dans ATLAS, l'énergie transverse manquante (E_T^{miss}) est un vecteur à deux composantes, calculé comme la somme vectorielle de l'énergie transverse déposée dans les calorimètres et l'impulsion transverse des muons identifiés, puis multiplié par un factor -1.

La reconstruction de l'énergie transverse manquante joue un rôle important dans le programme de physique de ATLAS.

Une mesure précise de E_T^{miss} en termes d'échelle et de résolution est importante pour les analyses de physique où la masse d'une particule se désintégrant en neutrinos doit être reconstruite. C'est le cas, par exemple, de la mesure de la masse du quark top dans le canal $t \to b\ell^+\nu_\ell$, mais aussi de la recherche d'un boson de Higgs se désintégrant dans une paire de leptons τ.

Une autre condition importante sur la reconstruction de l'énergie transverse manquante est la réduction des événements qui ont une grande quantité de fausse E_T^{miss}, due à la présence de défauts dans l'instrumentation. Un grand taux de ces événements pourrait augmenter de manière significative le bruit de fond pour des éventuels signaux de nouvelle physique, comme la supersymétrie. La large couverture des calorimètres, qui s'étend jusqu'à $|\eta| = 4.9$, réduit au minimum l'impact de particules produites à grandes pseudorapidités. Toutefois, la présence de régions de transition entre les différents systèmes calorimétriques peut occasionnellement causer une surestimation de l'énergie manquante. D'autres effets, notamment les fluctuations de l'énergie déposée par les jets de particules hadroniques, des cellules ou régions des calorimètres morts ou bruyants peuvent dégrader la mesure de E_T^{miss}.

Dans cette section, nous discutons de la façon de traiter l'énergie manquante instrumentale. Nous avons d'abord explorer la possibilité de mettre en évidence des effets instrumentaux à travers l'étude des corrélations entre les jets et E_T^{miss}. Ensuite, nous discutons de l'importance de surveiller constamment, pendant les opérations de prise de données, des variables significatives liés à E_T^{miss}. Enfin, nous décrivons la mise en place et la vérification d'un système de surveillance de ces variables dans ATLAS.

Corrélation entre énergie manquante et jets hadroniques

Dans les événement QCD, où l'énergie transportée par les neutrinos est généralement négligeable, l'énergie manquante instrumentale sera la principale composante de E_T^{miss}. Des fluctuations et des pertes dans la mesure de l'énergie des jets hadroniques causent l'alignement du vecteur E_T^{miss} à la direction des jets.

Ce n'est généralement pas le cas pour des événements avec un manque d'énergie transverse véritable. Ainsi, dans les recherches d'événements avec production de particules neutres et faiblement interagissantes, telles que les recherches de la supersymétrie, un critère d'isolement basé sur la différence angulaire entre la direction de E_T^{miss} et des jets peut aider à sélectionner le signal et rejeter le bruit de fond.

Un tel isolement de E_T^{miss} nécessite une reconstruction précise de sa direction. La Figure 5.1 montre la résolution de la direction azimutale $\phi_{E_T^{\text{miss}}}$ pour trois différents échantillons, $t\bar{t}$, $Z \to \tau^+\tau^-$ et $W \to e^{\pm}\nu_e$. Pour des valeurs de E_T^{miss} supérieures à 80 GeV, la résolution angulaire est d'environ 0.15 radians, donc plus petite que la taille typique d'un jet.

Ainsi, si on attend un signal caractérisé par des particules neutres et faiblement interagissantes, produites loin des jets, un critère d'isolation peut réduire la contribution du bruit de fond des événement QCD avec énergie manquante instrumentale, sans pourtant affecter significativement l'acceptation du signal. Par exemple, la Figure 5.3, à gauche, montre la distribution normalisée de la différence angulaire entre E_T^{miss} et le jet le plus énergétique de l'événement, $\Delta\phi(E_T^{\text{miss}}, \text{jet}) = \phi_{E_T^{\text{miss}}} - \phi_{\text{jet}}$, pour des échantillons de processus SUSY et QCD. Comme on peut le constater à partir de la Figure 5.3, à droite, une autre variable de discrimination potentiellement intéressante est la différence angulaire entre E_T^{miss} et le jet le plus proche, $|\Delta\phi_{\text{min}}(E_T^{\text{miss}}, \text{tout jet})|$. Le jet le plus proche est choisi parmi les jets avec impulsion transverse supérieure à 15 GeV.

Surveillance de l'énergie manquante

Étant construite par la totalité du système calorimétrique et du spectromètre à muons d'ATLAS, l'énergie transverse manquante est une variable globale de l'événement. En raison de cette nature, les résultats de la reconstruction de E_T^{miss} sont très sensibles

aux inefficacités et aux défaillances du détecteur. En particulier, ils peuvent être affectés par un étalonnage inexact des calorimètres.

Pour ces raisons, les analyses de physique requérant E_T^{miss} diffèrent de zéro comptent sur une bonne connaissance des systèmes de détection et des éventuels effets instrumentaux qui pourraient contribuer à modifier le bilan énergétique de l'événement.

L'identification et la correction des problèmes expérimentaux peuvent être effectuées au cours de l'analyse de physique sur les données recueillies. Toutefois, cette procédure n'est que partiellement satisfaisante, car une grande partie des événement recueillis pourrait alors devenir inutilisable, réduisant la luminosité intégrée disponible pour les enquêtes de physique. La majorité des défauts expérimentaux devrait être identifiés au cours de la prise de données, ou immédiatement après, permettant une intervention rapide et, par conséquence, réduisant au minimum la perte de données.

La fiabilité des données d'ATLAS est assurée par les activités de surveillance de la qualité des données. Le but est de constamment contrôler l'état des différents systèmes impliqués dans les prises de données, tels que le système de déclenchement, les sous-détecteurs, les objets physiques reconstruits, et de définir des niveaux de qualité optimals des conditions de fonctionnement du détecteur. Le résultat de l'examen est enregistré et rendu accessible pour les analyses de physique.

La surveillance de l'énergie transverse manquante est insérée dans l'infrastructure de contrôle de la qualité des données d'ATLAS. En plus d'être nécessaire pour assurer la fiabilité des analyses physiques et en raison de sa sensibilité aux échecs expérimentaux, un contrôle constant de E_T^{miss}, contribue également à mettre en évidence rapidement les problème à grande échelle du détecteur.

Des histogrammes des variables intéressantes sont remplis au cours du processus de reconstruction, où les signaux bruts des détecteurs sont transformés en objets physiques utilisables par les analyses. Les variables choisies doivent être significatives, mais en même temps élémentaires et simples à interpréter par les non experts présents au cours des prises de données. Des distributions plus détaillées doivent être disponibles au cas où des résultats suspects seraient trouvés.

Afin de tester la capacité du système de surveillance à détecter des problèmes dans E_T^{miss}, un échantillon d'événements QCD a été simulé dans une configuration problématique d'ATLAS. La réponse de certaines cellules du calorimètre est désactivée,

ce qui provoque une perte totale de l'énergie déposée dans ces récepteurs. Le schéma des cellules problématiques est présenté en Figure 5.5. Les algorithmes de surveillance sont exécutés sur environ 1500 événements. Cette statistique correspond à une ou deux minutes de prise de données, en supposant un taux de déclenchement de l'ordre de 10 Hz sur des jets énergétiques. Les histogrammes résultants sont comparés à des distributions de référence obtenues en simulant un détecteur idéal.

Les deux composantes du vecteur d'énergie manquante sont montrés en Figure 5.6. La présence de défauts expérimentaux se révèle dans le déplacement des pics par rapport à la valeur nulle attendue. L'écart de l'échantillon de référence est évident dans la distribution angulaire de E_T^{miss}, illustré en Figure 5.7.

Des informations sur la nature des problèmes sous-jacents sont extraites en comparant les différents contributions à l'énergie manquante. La valeur de E_T^{miss} est différente de zéro pour tout terme provenant des calorimètres, indépendamment de l'étalonnage (Figure 5.8, gauche). Une interaction plus profonde avec le système de surveillance des calorimètres est nécessaire pour déterminer la cause exacte du problème et les interventions à effectuer.

Recherche d'un boson de Higgs dans les cascades de désintégration de particules supersymétriques

Dans le cadre du Modèle Supersymétrique Standard Minimal, le plus léger boson de Higgs, h, peut être produit dans les collisions proton-proton soit par interaction directe de particules du Modèle Standard, tels que la fusion de deux gluons, ou lors de la désintégration en cascade de particules supersymétriques.

Dans le présent travail nous examinons la possibilité d'observer le boson de Higgs par ce deuxième mécanisme avec le détecteur ATLAS. Dans ce cas, en association avec le Higgs, une signature caractéristique d'énergie manquante, typique des scénarios SUSY avec conservation de la R-parité, peut être reconstruite et exploitée pour réduire le bruit de fond. Ceci rend possible l'étudie du canal de désintégration dominant $h \to b\bar{b}$, autrement couvert par l'énorme taux d'événements QCD.

La Figure 6.1 montre un affichage simulé des signaux déposés dans le détecteur ATLAS par un événement SUSY contenant un boson de Higgs qui se décompose en

deux quark b. Deux particules fortement interagissant, dans l'espace $\tilde{q}_R$ et $\tilde{l}_L$, sont produites lors de l'interaction proton-proton. Le $\tilde{q}_R$ se désintègre directement dans un $\tilde{\chi}_1^0$ stable et un quark, tandis que le $\tilde{q}_L$ génère un boson de Higgs en deux étapes :

$$\tilde{q}_L \rightarrow \tilde{\chi}_2^0 q \rightarrow \tilde{\chi}_1^0 h q.$$

Dans ce schéma, les quatre gerbes de traces collimatées, qui partent du centre du détecteur et se terminent par des dépôts d'énergie importants dans les calorimètres, sont causées par quatre jets hadroniques, dont deux sont les produits de désintégrations du Higgs et les deux autres viennent de la désintégration de squarks. Leur impulsion transverse totale est équilibrée par la ligne pointillée traversant l'ensemble du détecteur, qui représente l'énergie transverse manquante.

La possibilité d'observer de tels événements a déjà été abordée dans [66, 67]. Toutefois, depuis lors, les limites expérimentales inférieures sur la masse du boson de Higgs, provenant des recherches directe au LEP [35], ont été considérablement renforcés. Par conséquence, une grande région de l'espace des paramètres du modèle de Supergravité Minimale (mSUGRA) [57] a été exclue, en particulier pour des valeurs de $\tan\beta \lesssim 5$ [89] où l'analyse avait été effectuée. Au-delà de cette valeur, le mélange entre squarks gauche et droit de troisième génération devient important et conduit à une grande séparation entre les états propres de masse. Il en résulte un stop et un sbottom plus légers que les autres squarks. La fraction d'événement SUSY contenant ce type de squarks subit donc, une forte augmentation, et cause du bruit de fond pour les recherches du Higgs dans les canal $b\bar{b}$. Les scénarios choisis pour l'analyse ici présentée, reflètent cette situation. Leurs définitions en terme de paramètres de mSUGRA se trouvent page 88, référencés sous les noms de Point 1 et Point 2. Les deux points se différencient par leur valeur de $\tan\beta$, le premier étant à $\tan\beta = 20$ et le deuxième à $\tan\beta = 54$, qui donc aura un niveau de bruit de fond $b\bar{b}$ encore plus élevé.

Dans la suite nous évaluons le potentiel de découverte du Higgs dans ces deux scénarios. En plus, nous considérons la possibilité de déterminer les masses et les couplages des particules SUSY participant à la cascade étudiée.

La réponse du détecteur ATLAS est reproduite par une simulation rapide. La validité de cette technique est vérifiée par une comparaison avec les performances obtenues par une simulation complète du détecteur. En particulier, l'analyse de recherche du Higgs est complètement répétée avec des échantillons générés par simulation complète.

Les résultats et les détails de cette étude de comparaison sont discutés dans la Section 6.8.

Recherche de $h \to b\bar{b}$

Les bruits de fond pour cette analyse sont constitués par :

- les événements SUSY sans Higgs, mais avec une paire de jets de b produite ;
- les événements SUSY avec un Higgs, pour lesquels les jets de b choisis pour reconstruire la masse du Higgs ne viennent pas de cette particule (bruit combinatoire) ;
- les événements du Modèle Standard avec émission de neutrinos ;
- les événements de QCD, avec de la fausse énergie manquante.

Pour réduire ces bruits de fond et sélectionner les événements du signal, nous demandons :

1. $E_T^{\text{miss}} > 300$ GeV ;
2. 2 jets issus de quarks légers avec $p_T > 100$ GeV ;
3. 2 jets de b avec $p_T > 50$ GeV ;
4. pas de leptons avec $p_T > 10$ GeV.

Les deux premières coupures sont typiques des recherches des événement SUSY à ATLAS, tandis que la troisième sélectionne les jets de b provenant du Higgs. Déjà avec ces coupures le pic de résonance du Higgs est visible sur le bruit de fond continu. La quatrième sélection permet une suppression supplémentaire des processus comme $pp \to W$ et $pp \to t\bar{t}$.

La Figure 6.5 montre la masse invariante des paires de jets de b sélectionnées pour les Points 1 et 2, en supposant 10 fb^{-1} de luminosité recueillie. Le nombre estimé d'événements du signal et du bruit de fond est obtenu en comptant les paires de b ayant une masse invariante à l'intérieur d'une fenêtre de ± 25 GeV autour du centre du pic de résonance. La signification statistique, calculée par le rapport du nombre d'événements du signal sur la racine carré du bruit de fond, est respectivement de 12 et 8 pour les deux scénarios considérés.

Le Tableau 6.1 résume les taux d'événements prévus après l'application des coupures de 1 à 4 et après la requête sur la fenêtre de masse.

Comme déjà souligné, l'analyse du Higgs dans les cascades SUSY peut être un point de départ pour la reconstruction des masses d'autres nouvelles particules. On considère la cascade dominante pour la production du Higgs

$$\tilde{q}_L \to \tilde{\chi}_2^0 q \to \tilde{\chi}_1^0 h q.$$

La masse invariante du système $h + q$, M_{hq}, présente une valeur de seuil et une valeur maximale, qui dépendent des masses inconnues $m_{\tilde{\chi}_1^0}$, $m_{\tilde{\chi}_2^0}$, $m_{\tilde{q}_L}$.

Les graphiques de masse invariante dans les Figures 6.7 (Point 1) et 6.8 (Point 2) sont obtenus en ajoutant aux paires de jets de b, sélectionnés, un jet issue d'un quark léger. Pour réduire le bruit de fond combinatoire, nous demandons qu'au moins un jet de b satisfasse $p_T > 100$ GeV et qu'aucun jet de b supplémentaire avec $p_T > 50$ GeV soit trouvé dans l'événement.

Les événements SUSY étant riches en jets, le choix du jet provenant du $\tilde{q}_L$ à associer au Higgs n'est pas évident. Notre stratégie est la suivante. Les deux jets avec les plus élevés p_T sont identifiés et deux distributions de masse invariante M_{hq} sont reconstruites, respectivement avec le jet qui minimise (graphiques de gauche) et le jet qui maximise la valeur de M_{hq} (graphiques de droite). Comme le bruit de fond aura tendance à se concentrer vers les valeurs de faible masse, la distribution obtenue en utilisant le jet qui minimise M_{hq} sera utilisée pour déterminer la limite supérieure de M_{hq}. La valeur de seuil de M_{hq} sera quant á elle déterminée à partir de l'autre distribution de masse.

Les mesures, extraites par un ajustement avec une fonction triangulaire convoluée avec une résolution gaussienne, sont résumées dans le Tableau 6.3. On remarque que la valeur de seuil pour le Point 2 n'a pas pu être évaluée à cause du bruit de fond trop important.

Signatures di-leptoniques

Pour récupérer des informations additionnelles sur les masses des nouvelles particules, nous pouvons chercher seuils et maximums dans d'autres distributions de masse invariante. La plus propre, donc plus puissante, vient de la typologie constituée par deux leptons plus de l'énergie manquante. Malheureusement, la désintégration du $\tilde{\chi}_2^0$ en paire de leptons doit être cinematiquement interdite pour que le canal $\tilde{\chi}_2^0 \to \tilde{\chi}_1^0 h$

soit ouvert. Ainsi la masse invariante de deux leptons ne présente ni un seuil ni un maximum, mais seulement le pic de résonance du boson Z, provenant du processus $\tilde{\chi}_2^0 \to \tilde{\chi}_1^0 Z$.

Toutefois, nous pouvons extraire quelques indices indirects sur la nature de la nouvelle physique. Les cascades $A \to B^{(*)}\ell^{\mp} \to C\ell^{\pm}\ell^{\mp}$, où A, B et C sont des particules génériques du modèle, doivent être supprimé par rapport aux cascades contenant un $Z \to \ell^+\ell^-$. En outre, les taux de production du Z et du Higgs h peuvent aussi être comparés. Ces observations aident à restreindre la gamme des modèles possibles.

Nous sélectionnons, donc, deux échantillons d'événements, un caractérisé par la présence de deux leptons, l'autre de deux jet de b, isolés par un ensemble identique de coupures de sélection :

1. $E_T^{\text{miss}} > 300$ GeV ;
2. 2 jets issus de quarks légers avec $p_T > 100$ GeV ;
3. 2 leptons (e or μ) où 2 b-jets avec $p_T > 25$ GeV.

De plus, pour se débarrasser du bruit de fond di-leptonique, nous soustrayons à la distribution de masse des deux leptons avec la même saveur, la distribution de masse construite de la même façon mais avec deux leptons de saveur différente. Les masses invariantes di-leptonique avant et après cette soustraction sont reportées dans la Figure 6.9 pour les deux points étudiés.

La limite supérieure sur la production de deux leptons, autre que par la désintégration du Z, peut être définie par le nombre d'événements de masse entre 0 et 85 GeV, $N_{\ell^+\ell^-}$, divisé par N_Z, le nombre d'entrées dans la fenêtre de résonance du Z. Le résultat à 95% de niveau de confiance est

$$\frac{\sigma((\text{Any}) \to \ell^+\ell^-)}{\sigma(Z \to \ell^+\ell^-)} < \frac{N_{\ell^+\ell^-}}{N_Z} + 1.65\sigma = 0.10 + 1.65(0.11\ (\text{stat}) \oplus 0.01\ (\text{syst})) = 0.29$$

pour le Point 1 et

$$\frac{\sigma((\text{Any}) \to \ell^+\ell^-)}{\sigma(Z \to \ell^+\ell^-)} < \frac{N_{\ell^+\ell^-}}{N_Z} + 1.65\sigma = -0.12 + 1.65(0.10\ (\text{stat}) \oplus 0.01\ (\text{syst})) = 0.05$$

pour le Point 2.

La mesure du rapport des taux de production du h et du Z est plus difficile. Les points suivants doivent être pris en compte :

- les différentes efficacités de reconstruction et la résolutions en masse pour les leptons et les jets de b ;
- la présence d'un bruit de fond combinatoire non négligeable dans l'analyse $h \to b\bar{b}$.

Le premier point n'est pas un problème, parce que les résolutions et les efficacités du détecteur seront bien connus après 300 fb^{-1} de données collectées, tels que supposés ici. Néanmoins un 5% d'incertitude sur l'efficacité d'etiquettage des jets de b doit être considéré comme un effet systématique [100, 101]. Le deuxième point est la vraie difficulté. Si d'un coté très peu d'événements de Z seront perdu à cause du fond combinatoire, la perte d'événements de h est extrêmement élevée et ne peut pas être estimée. Donc, nous sommes obligés de fixer seulement une limite inférieure à 95% de niveau de confiance. Pour les Points 1 et 2, les résultats sont les suivants :

$$\begin{aligned}\frac{\sigma(h \to b\bar{b})}{\sigma(Z \to \ell^+\ell^-)} &> \frac{N_h}{N_Z}\frac{\epsilon_\ell^2}{\epsilon_b^2} - 1.65\sigma = \\ &= \frac{9931}{1222-431}\frac{1}{0.36} - 1.65(2.0\ (\text{stat}) \oplus 1.7\ (\text{syst}) \oplus 3.4\ (\text{b-tag})) = 28,\end{aligned}$$

$$\begin{aligned}\frac{\sigma(h \to b\bar{b})}{\sigma(Z \to \ell^+\ell^-)} &> \frac{N_h}{N_Z}\frac{\epsilon_\ell^2}{\epsilon_b^2} - 1.65\sigma = \\ &= \frac{5566}{1522-546}\frac{1}{0.36} - 1.65(1.0\ (\text{stat}) \oplus 0.8\ (\text{syst}) \oplus 1.6\ (\text{b-tag})) = 13.\end{aligned}$$

Les efficacités d'identification des leptons et des jets de b sont marquées par ϵ_ℓ et ϵ_b. Les erreurs statistiques sont de l'ordre 6%. L'incertitude sur la coupure en p_T est estimée par une variation de 5 GeV sur la valeur utilisée, ce qui donne une erreur systématique de l'ordre du 5%.

Les deux limites inférieures peuvent être comparées avec les vraies valeurs de $\sigma(h \to b\bar{b})/\sigma(Z \to \ell^+\ell^-) = 40$ pour le Point 1 et $\sigma(h \to b\bar{b})/\sigma(Z \to \ell^+\ell^-) = 28$ pour le Point 2.

Recherche de $h \to \gamma\gamma$

Jusqu'ici, nous avons considéré seulement la désintégration $h \to b\bar{b}$ et nous avons vu comment la présence de jets de b dans les cascades SUSY rend difficile la mise en évidence de ce processus, spécialement à grand $\tan\beta$. La désintégration $h \to \gamma\gamma$ offre une alternative intéressante malgré sa très faible fraction d'embranchement. En effet, ce canal profite d'un faible bruit de fond : non seulement il n'y a presque pas de photons

produits dans les cascades SUSY, ce qui élimine le problème du fond combinatoire, mais aussi les événements du Modèle Standard qui présentent la typologie $\gamma\gamma + E_T^{miss}$ sont rares.

Au fin de ne pas perdre les rares événements du signal, des coupures de sélection très lâches sont nécessaires :

1. $E_T^{\text{miss}} > 100$ GeV ;
2. 2 jets issus de quarks légers avec $p_T > 100$ GeV ;
3. 2 photons avec $p_T > 20$ GeV.

La distribution de masse invariante des deux photons pour les événements sélectionnés est illustré en Figure 6.10, en supposant une luminosité intégrée de 30 fb^{-1}. En raison du petit nombre d'événements attendus, indiqué pour le signal et le bruit de fond dans le Tableau 6.4, la signification statistique du signal est estimée en utilisant la statistique de Poisson. Elle est aux alentours de 3.5. Une découverte à 5σ serait donc possible après environ 70 fb^{-1}.

Extrapolation des paramètres SUSY

Comme précédemment discuté, l'existence de physique au-delà du Modèle Standard accessible au LHC est bien motivée à la fois par des indices expérimentaux et par des finalités de caractère théorique. Parmi les principaux objectifs des expériences du LHC est, bien entendu, l'observation des processus causés par cette nouvelle physique. Si cela se produit, une attention particulière sera portée sur la détermination de la nature de la théorie sous-jacente des phénomènes observés, ou au moins sur les limites des possibles interprétations théoriques des données.

Toutefois, les scénarios de nouvelle physique sont décrits en termes de nouveaux paramètres, á présent inconnus et généralement très peu contraints par les mesures actuelles. Pour la plus part des modèles proposés, ces paramètres libres s'élèvent à un grand nombre. En outre, les processus pouvant être visibles au LHC sont souvent caractérises par des signatures complexes. Par exemple, les modèle supersymétriques ne prévoient pas de résonance claire, due à la désintégration d'une nouvelle particule, mais plutôt une variété de cascades de désintégration de particules supersymétriques. Les caractéristiques de chaque cascade, c'est-à-dire son taux de production et la forme des

distributions de masses invariantes des états qui en sortent, dépendent des paramètres libres du modèle. Pour toutes ces raisons, l'exclusion des interprétations possibles des événements produits au LHC ainsi que l'extraction des paramètres qui décrivent le mieux les données peuvent être des taches compliquées.

Outre les mesures effectuées par les expériences du LHC, un possible modèle de nouvelle physique devra également être en accord avec de nombreux mesures à basse énergie, comme par exemple le moment magnétique anormal du muon [22]. De plus, si la même théorie veut fournir une solution à l'existence de la matière noire, elle doit prédire une densité résiduelle, du candidat composant la matière noire, compatible avec les observations cosmologiques. Ceci limite sérieusement la masse et les couplages non seulement du candidat lui-même, mais aussi des autres particules impliquées dans le processus d'annihilation entre les particules de matière noire, lors des premiers instants de l'univers.

Une approche consiste à combiner toutes les quantités mesurées et de construire une carte de vraisemblance dans l'espace des paramètres pour un modèle donné, où la fonction de vraisemblance est destinée à évaluer l'accord entre les données et les prévisions théoriques. L'ensemble des paramètres qui décrit le mieux les résultat expérimentaux correspond au maximum de la fonction de vraisemblance dans l'espace des paramètres. Des maximums secondaires peuvent éventuellement exister. Les modèles ne donnant que des basses valeurs de vraisemblance sur tout l'espace des paramètres peuvent être exclus, jusqu'à un certain niveau de confiance.

Le but de cette analyse est d'appliquer cette approche aux spécificité des scénarios supersymétriques avec production du bosons de Higgs étudiés dans la section précédente. À partir des quantités mesurées et les incertitudes relatives pour les Points de référence 1 et 2, nous extrayons les régions compatibles de l'espace des paramètres du modèle mSUGRA. Pour cela, nous utilisons l'outil `SFitter` [105, 106, 103] ; en particulier nous appliquons la méthode des chaînes de Markov, contre-vérifié par l'algorithme de minimisation `Migrad` [113]. L'intention est de prouver la validité de la méthode et, en même temps, d'illustrer un exemple de traitement à adopter lorsque les véritables données du LHC seront disponibles.

Résultats pour le Point 1

Le Tableau 7.1 résume les différentes observables disponibles pour le Point 1, en supposant 300 fb^{-1} de luminosité recueillie par les expériences du LHC. En plus des deux mesures et des deux limites extraites dans la section précédente, la masse du quark top et du plus léger des bosons de Higgs sont prises en compte [104]. Les trois dernières lignes dans le Tableau 7.1 sont des mesures supplémentaires qui devraient être obtenus au LHC, même si considérées comme très difficiles [119, 67, 84].

D'abord nous créons un ensemble simulé de quantités mesurées à partir des valeurs vraies du scénario, qui sont en suite modifiées selon les incertitudes estimées. La fonction de vraisemblance est alors tracée sur l'espace des paramètres de mSUGRA plus le paramètre supplémentaire m_t. Comme il est difficile de traiter des paramètres discrets, deux différentes analyses sont effectuées, une pour chaque signe du paramètre μ.

L'outil `SFitter` produit une carte complète, en 5 dimensions, de la fonction de vraisemblance $\mathscr{L}$. Le profil de la fonction sur un espace de dimension inférieure est obtenue de cette façon : pour chaque point fixé dans l'espace à $(n-1)$ dimensions, la fonction est exploré au long de la $n^{\text{ème}}$ dimension et seulement sa valeur la plus élevée est conservée.

Les profils des distributions du $\chi^2 = -2\ln(\mathscr{L})$ pour les différents paramètres (et pour $\mu > 0$) sont reportes dans les Figures 7.1 et 7.2.

Le bandes bleues dans les profils du χ^2 à une dimension indiquent les régions où celui-ci varie de moins d'une unité par rapport à son minimum. Par conséquence, l'intervalle de valeurs pour lequel la fonction reste dans la bande bleue est l'intervalle compatible avec données pour un niveau de confiance de 68% :

$$\begin{array}{rcccl} 290 & < & M_0 \text{ (GeV)} & < & 450 \\ 385 & < & M_{1/2} \text{ (GeV)} & < & 420 \\ -250 & < & A \text{ (GeV)} & < & 150 \\ 13 & < & \tan\beta & < & 34 \\ 173.2 & < & m_t \text{ (GeV)} & < & 175.2. \end{array}$$

La fonction de vraisemblance est recalculée sur tout l'espace des paramètres pour le cas de μ négatif. La Figure 7.3 montre les résultats principaux.

Tous les minimums locaux du χ^2 trouvé par `SFitter`, pour des valeurs de μ à la fois positifs et négatifs, sont énumérés dans le Tableau 7.3. Même si la valeur absolue

du χ^2 est plus petite pour $\mu > 0$, l'hypothèse de μ négatif ne peut pas être rejetée. Une des informations utiles pour choisir le signe de μ est la valeur expérimentale du moment magnétique anormal du muon [120].

Afin de mettre à l'épreuve la méthode d'analyse, nous considérons ensuite le cas pessimiste où les mesures de m_{H^0}, $BR(h \to \gamma\gamma)/BR(h \to b\bar{b})$ et $BR(h \to \tau^+\tau^-)/BR(h \to WW)$ ne sont pas accessibles au LHC. Les intervalles de confiance, pour le cas μ positif, sont :

$$\begin{array}{rcccl} 150 & < & M_0 \text{ (GeV)} & < & 620 \\ 360 & < & M_{1/2} \text{ (GeV)} & < & 450 \\ -300 & < & A \text{ (GeV)} & < & 200 \\ & & \tan\beta : \text{libre} & & \\ 173.2 & < & m_t \text{ (GeV)} & < & 175.2. \end{array}$$

Les paramètres fortement liés à m_h, c'est-à-dire $M_{1/2}$ et A, ne sont presque pas affectés. En outre, la masse du quark top reste évidemment inchangée, car elle est contrôlée par sa mesure directe. Au contraire, $\tan\beta$ est maintenant complètement libre dans la région théoriquement accessible ($2 \lesssim \tan\beta \lesssim 60$), car les informations sur sa nature sont transportées par les mesures dans le secteur du Higgs. En outre, la performance sur la détermination de M_0 se dégrade, révélant que sa précision est dominée par la mesure de la masse du Higgs lourd.

Résultats pour le Point 2

Les mesures accessibles pour le Point 2 sont listées en Tableau 7.4. Elles différent du cas du Point 1 par deux éléments. Tout d'abord, le seuil dans la distribution de masse invariante du système du Higgs plus un jet n'est pas mesurable à cause du bruit de fond très élevé. Deuxièmement, ce point a été choisi pour être compatible avec la densité résiduelle de matière noire observée par l'expérience WMAP [38]. Par conséquence, il est intéressant d'insérer la densité résiduelle de la plus légère particule supersymétrique dans la fonction de vraisemblance et d'enquêter sur l'effet provoqué dans les résultats de `SFitter`.

Les profils de la distribution du χ^2 pour μ positif sont illustrés sur la Figure 7.4. L'analyse identifie bien la région correspondant aux véritables paramètres du point étudié. La valeur du minimum absolu est de $\chi^2_{\text{min}} = 1.90$, avec $N_{\text{dof}} = 4$. Les autres

minimums locaux sont énumérés dans le Tableau 7.5.

Des profils de la distribution du χ^2, nous déduisons les intervalles de confiance à 68% :

$$\begin{array}{rcccl} 400 & < & M_0 \text{ (GeV)} & < & 560 \\ 365 & < & M_{1/2} \text{ (GeV)} & < & 405 \\ -300 & < & A \text{ (GeV)} & < & 100 \\ 52.2 & < & \tan\beta & < & 54.4 \\ 173.2 & < & m_t \text{ (GeV)} & < & 175.2. \end{array}$$

Par rapport aux résultats obtenus pour le Point 1, la principale différence est la détermination précise de $\tan\beta$. En effet, la condition sur la densité résiduelle de la particule supersymétrique la plus légère limite fortement son intervalle de confiance.

Conclusions

Malgré ses succès et les nombreuses mesures expérimentales qui confirment sa validité aux échelles d'énergie actuellement explorées, le Modèle Standard de la physique de particules reste incomplet. Des observations comme la masse des neutrinos, la présence de matière noire dans l'univers et l'asymétrie entre baryon et anti-baryon, ainsi que des problèmes de consistance de la théorie, suggèrent l'existence de nouvelles particules et interactions, non encore découvertes à ce jour.

Parmi les extensions du Modèle Standard, les modèles supersymétriques prédisent l'existence d'un grand nombre de nouvelles particules de masse à l'échelle du TeV, qui donc peuvent être produites au LHC. La recherche de preuves de la supersymétrie sera un objectif principal de l'expérience ATLAS lors des premières collisions proton-proton, prévues pour septembre 2008.

Dans ces modèles, le plus léger boson de Higgs peut être produit au LHC dans les cascades de désintégrations de particules supersymétriques. La signature caractéristique de ces processus est composée par la paire de particules provenant de la désintégration du Higgs, typiquement deux quarks bottom, et par de l'énergie manquante, due à la production de particules supersymétriques qui échappent à la détection.

Nous avons développé, à travers des simulations détaillées, une analyse complète qui :

- assure la solidité et la fiabilité des mesures d'énergie manquante par le détecteur ATLAS ;
- évalue le potentiel de découverte d'ATLAS d'un Higgs produit dans les cascades de désintégration de particules supersymétriques ;
- étudie la possibilité de mesurer les masses et les couplages des nouvelles particules mises en jeux.

Le travail se concentre d'abord sur les performances de la mesure de l'énergie manquante, avec un intérêt particulier pour la réduction des effets instrumentaux. En outre, nous établissons un système qui contrôle constamment au cours des opérations de prise de données la reconstruction de l'énergie manquante.

Dans la suite, le potentiel de découverte du boson de Higgs neutre le plus léger est étudié en détail dans deux scénarios avec caractéristiques phénoménologiques différentes. Nous montrons que la résonance due a la désintégration du Higgs dans deux quarks bottom peut être mise en évidence avec moins de 10 fb^{-1} de données collectées.

Dans la dernière partie de l'exposé, nous décrivons une méthode statistique pour extraire les paramètres d'un modèle supersymétrique, à partir d'un ensemble de mesures au LHC. La méthode est appliquée au cas particulier des scénarios proposés, prouvant ainsi la validité de la méthode même pour l'exploration de modèles avec des espaces des paramètres à plusieurs dimensions.

BIBLIOGRAPHY

[1] F.J. Dyson, Phys. Rev. 85 (1952) 631.

[2] R.P. Feynman, Rev. Mod. Phys. 20 (1948) 367.

[3] R.P. Feynman, Phys. Rev. 74 (1948) 939.

[4] R.P. Feynman, Phys. Rev. 74 (1948) 1430.

[5] J.S. Schwinger, Phys. Rev. 73 (1948) 416.

[6] J.S. Schwinger, Phys. Rev. 74 (1948) 1439.

[7] S. Tomonaga, Prog. Theor. Phys. 1 (1946) 27.

[8] F. Mandl and G. Shaw, Wiley (1984).

[9] M.E. Peskin and D.V. Schroeder, Addison-Wesley (1995).

[10] C.N. Yang and R.L. Mills, Phys. Rev. 96 (1954) 191.

[11] F. Englert and R. Brout, Phys. Rev. Lett. 13 (1964) 321.

[12] P.W. Higgs, Phys. Lett. 12 (1964) 132.

[13] P.W. Higgs, Phys. Rev. Lett. 13 (1964) 508.

[14] P.W. Higgs, Phys. Rev. 145 (1966) 1156.

[15] S.L. Glashow and S. Weinberg, Phys. Rev. Lett. 20 (1968) 224.

[16] A. Salam and J.C. Ward, Phys. Lett. 13 (1964) 168.

[17] J.F. Gunion et al., SCIPP-89/13 (1989).

[18] B.C. Odom et al., Phys. Rev. Lett. 97 (2006) 030801.

[19] R.S. Van Dyck, P.B. Schwinberg and H.G. Dehmelt, Phys. Rev. Lett. 59 (1987) 26.

[20] P. Clade et al., Phys. Rev. Lett. 96 (2006) 033001.

[21] V. Gerginov et al., Phys. Rev. A73 (2006) 032504.

[22] Muon G-2 Collaboration, G.W. Bennett et al., Phys. Rev. D73 (2006) 072003, hep-ex/0602035.

[23] M. Davier, Nucl. Phys. Proc. Suppl. 169 (2007) 288, hep-ph/0701163.

[24] D. Stockinger, J. Phys. G34 (2007) R45, hep-ph/0609168.

[25] S. Heinemeyer, D. Stockinger and G. Weiglein, Nucl. Phys. B699 (2004) 103, hep-ph/0405255.

[26] S. Heinemeyer, D. Stockinger and G. Weiglein, Nucl. Phys. B690 (2004) 62, hep-ph/0312264.

[27] D.W. Hertzog et al., (2007), arXiv:0705.4617 [hep-ph].

[28] W.M. Yao et al., Journal of Physics G 33 (2006) 1.

[29] ALEPH, DELPHI, L3, OPAL Collaborations, the LEP Electroweak Working Group and the SLD Electroweak and Heavy Flavour Groups, Phys. Rept. 427 (2006) 257, hep-ex/0509008.

[30] LEP Electroweak Working Group, http://lepewwg.web.cern.ch/LEPEWWG (2008).

[31] ALEPH, DELPHI, L3, OPAL Collaborations and the LEP Electroweak Working Group, (2006), hep-ex/0612034.

[32] CDF Collaboration, T. Aaltonen et al., Phys. Rev. Lett. 99 (2007) 151801, arXiv:0707.0085 [hep-ex].

[33] D0 Collaboration, V.M. Abazov et al., Phys. Rev. D66 (2002) 012001, hep-ex/0204014.

[34] NuTeV Collaboration, G.P. Zeller et al., Phys. Rev. Lett. 88 (2002) 091802, hep-ex/0110059.

[35] LEP Working Group for Higgs boson searches, R. Barate et al., Phys. Lett. B565 (2003) 61, hep-ex/0306033.

[36] Tevatron New Phenomena & Higgs Working Group, CDF Note 8384, D0 Note 5227 (2007).

[37] F. Zwicky, Helv. Phys. Acta 6 (1933) 110.

[38] WMAP Collaboration, D.N. Spergel et al., Astrophys. J. Suppl. 170 (2007) 377, astro-ph/0603449.

[39] WMAP Collaboration, E. Komatsu et al., (2008), arXiv:0803.0547 [astro-ph].

[40] D. Clowe et al., Astrophys. J. 648 (2006) L109, astro-ph/0608407.

[41] Super-Kamiokande Collaboration, Y. Fukuda et al., Phys. Rev. Lett. 81 (1998) 1562, hep-ex/9807003.

[42] SNO Collaboration, Q.R. Ahmad et al., Phys. Rev. Lett. 89 (2002) 011301, nucl-ex/0204008.

[43] KamLAND Collaboration, K. Eguchi et al., Phys. Rev. Lett. 90 (2003) 021802, hep-ex/0212021.

[44] K2K Collaboration, E. Aliu et al., Phys. Rev. Lett. 94 (2005) 081802, hep-ex/0411038.

[45] S.M. Bilenky and S.T. Petcov, Rev. Mod. Phys. 59 (1987) 671.

[46] G. Bertone, D. Hooper and J. Silk, Phys. Rept. 405 (2005) 279, hep-ph/0404175.

[47] E.A. Baltz et al., Phys. Rev. D74 (2006) 103521, hep-ph/0602187.

[48] S. Dodelson, Academic Press (2003).

[49] R. Haag, J.T. Lopuszanski and M. Sohnius, Nucl. Phys. B88 (1975) 257.

[50] S.R. Coleman and J. Mandula, Phys. Rev. 159 (1967) 1251.

[51] H.P. Nilles, Phys. Rept. 110 (1984) 1.

[52] S.P. Martin, (1997), hep-ph/9709356.

[53] M.E. Peskin, (2008), arXiv:0801.1928 [hep-ph].

[54] M. Drees, (1996), hep-ph/9611409.

[55] H.E. Haber and G.L. Kane, Phys. Rept. 117 (1985) 75.

[56] S. Ferrara, L. Girardello and F. Palumbo, Phys. Rev. D20 (1979) 403.

[57] H.P. Nilles, Phys. Lett. B115 (1982) 193.

[58] L. Alvarez-Gaume, J. Polchinski and M.B. Wise, Nucl. Phys. B221 (1983) 495.

[59] L.E. Ibanez, Phys. Lett. B118 (1982) 73.

[60] J.R. Ellis, D.V. Nanopoulos and K. Tamvakis, Phys. Lett. B121 (1983) 123.

[61] K. Inoue et al., Prog. Theor. Phys. 68 (1982) 927.

[62] A.H. Chamseddine, R. Arnowitt and P. Nath, Phys. Rev. Lett. 49 (1982) 970.

[63] M. Dine, A.E. Nelson and Y. Shirman, Phys. Rev. D51 (1995) 1362, hep-ph/9408384.

[64] M. Dine et al., Phys. Rev. D53 (1996) 2658, hep-ph/9507378.

[65] ATLAS Collaboration, CERN-LHCC-94-43 (1994).

[66] ATLAS Collaboration, CERN-LHCC-99-14 (1999).

[67] ATLAS Collaboration, CERN-LHCC-99-15 (1999).

[68] ATLAS Collaboration, CERN-ATL-COM-PHYS-2007-102 (2007).

[69] G. Flugge, 1993 European School of High-energy Physics, CERN-94-04 (1994).

[70] ATLAS Collaboration, CERN-LHCC-97-16 (1997).

[71] ATLAS Collaboration, CERN-LHCC-97-17 (1997).

[72] ATLAS Collaboration, CERN-LHCC-96-40 (1996).

[73] ATLAS Collaboration, CERN-LHCC-97-22 (1997).

[74] ATLAS Collaboration, CERN-LHCC-98-14 (1998).

[75] ATLAS Collaboration, CERN-LHCC-2003-022 (2003).

[76] ATLAS Collaboration, CERN-LHCC-2005-022 (2005).

[77] S. Agostinelli et al., Nucl. Instrum. Meth. A506 (2003) 250.

[78] J. Allison et al., IEEE Trans. Nucl. Sci. 53 (2006) 270.

[79] ATLAS Electromagnetic Barrel Calorimeter Collaboration, M. Aharrouche et al., Nucl. Instrum. Meth. A568 (2006) 601.

[80] M. Cacciari and G.P. Salam, Phys. Lett. B641 (2006) 57, hep-ph/0512210.

[81] B.W. Lee, C. Quigg and H.B. Thacker, Phys. Rev. D16 (1977) 1519.

[82] K. Cranmer et al., CERN-ATL-PHYS-2004-034 (2004).

[83] M.S. Carena et al., Eur. Phys. J. C26 (2003) 601, hep-ph/0202167.

[84] M. Schumacher, CERN-ATL-COM-PHYS-2004-070 (2004).

[85] M. Schumacher, (2004), hep-ph/0410112.

[86] E. Accomando et al., (2006), hep-ph/0608079.

[87] ATLAS Collaboration, ATLAS CSC Note SUSY0 (2008).

[88] A. Hoecker, ATLAS Data Preparation Meeting (2006), Readapted graphics.

[89] ALEPH, DELPHI, L3, OPAL Collaborations, S. Schael et al., Eur. Phys. J. C47 (2006) 547, hep-ex/0602042.

[90] F.E. Paige et al., (2003), hep-ph/0312045.

[91] G. Corcella et al., JHEP 01 (2001) 010, hep-ph/0011363.

[92] S. Moretti et al., JHEP 04 (2002) 028, hep-ph/0204123.

[93] J.M. Butterworth, J.R. Forshaw and M.H. Seymour, Z. Phys. C72 (1996) 637, hep-ph/9601371.

[94] M.L. Mangano et al., JHEP 07 (2003) 001, hep-ph/0206293.

[95] M.L. Mangano, M. Moretti and R. Pittau, Nucl. Phys. B632 (2002) 343, hep-ph/0108069.

[96] E. Richter-Was, D. Froidevaux and L. Poggioli, CERN-ATL-PHYS-98-131 (1998).

[97] G. Belanger et al., Comput. Phys. Commun. 176 (2007) 367, hep-ph/0607059.

[98] G. Belanger et al., Comput. Phys. Commun. 174 (2006) 577, hep-ph/0405253.

[99] G. Belanger et al., Comput. Phys. Commun. 149 (2002) 103, hep-ph/0112278.

[100] ATLAS Collaboration, ATLAS CSC Note BT8 (2008).

[101] ATLAS Collaboration, ATLAS CSC Note BT10 (2008).

[102] F.G. Monticelli, Private communication (2007).

[103] R. Lafaye et al., (2007), arXiv:0709.3985 [hep-ph].

[104] LHC/LC Study Group, G. Weiglein et al., Phys. Rept. 426 (2006) 47, hep-ph/0410364.

[105] R. Lafaye, T. Plehn and D. Zerwas, (2004), hep-ph/0404282.

[106] R. Lafaye, T. Plehn and D. Zerwas, ECONF C0508141 (2005) ALCPG0607, hep-ph/0512028.

[107] P. Skands et al., JHEP 07 (2004) 036, hep-ph/0311123.

[108] B. Allanach et al., (2008), 0801.0045.

[109] W. Beenakker et al., Nucl. Phys. B492 (1997) 51, hep-ph/9610490.

[110] W. Beenakker et al., Nucl. Phys. B515 (1998) 3, hep-ph/9710451.

[111] W. Beenakker et al., Phys. Rev. Lett. 83 (1999) 3780, hep-ph/9906298.

[112] T. Plehn, (1998), hep-ph/9809319.

[113] F. James and M. Roos, Comput. Phys. Commun. 10 (1975) 343.

[114] R. Barlow, (2003), physics/0311105.

[115] CKMfitter Group, J. Charles et al., Eur. Phys. J. C41 (2005) 1, hep-ph/0406184.

[116] J. Neyman, Phil. Trans. Royal Soc. London Series A 236 (1937) 333.

[117] N. Metropolis et al., Journal of Chemical Physics 21 (1953) 1087.

[118] W.K. Hastings, Biometrika 57 (1970) 97.

[119] V. Buescher and K. Jakobs, Int. J. Mod. Phys. A20 (2005) 2523, hep-ph/0504099.

[120] M.M. Nojiri et al., (2008), 0802.3672.